

Marine Anti-Malarial Isonitriles: A Synthetic and Computational Study

**A thesis submitted in fulfilment of the requirements for the degree
of
Master of Science**



RHODES UNIVERSITY
Grahamstown • 6140 • South Africa

Matthew Ralph Adendorff

February 2010

Abstract

The development of *Plasmodium falciparum* malarial resistance to the current armoury of anti-malarial drugs requires the development of new treatments to help combat this disease. The marine environment is a well established source of potential pharmaceuticals. Of interest to us are isonitrile, isocyanate and isothiocyanate compounds isolated from marine sponges and molluscs which have exhibited nano-molar anti-plasmodial activities. Through quantitative structure-activity relation studies (QSAR), a literature precedent exists for a pseudoreceptor model from which a pharmacophore for the design of novel anti-malarial agents was proposed. The current theory suggests that these marine compounds exert their inhibitory action through interfering with the heme detoxification pathway in *P. falciparum*. We propose that the computational methods used to draw detailed conclusions about the mode of action of these marine compounds were inadequate. This thesis addresses this problem using contemporary computational methodologies and seeks to propose a more robust method for the rational design of new anti-malarial drug compounds that inhibit heme polymerization to hemozoin.

In order to investigate the interactions of the marine compounds with their heme targets, a series of modern computational procedures were formulated, validated and then applied to theoretical systems. The validations of these algorithms, before their application to the marine compound-heme systems, were achieved through two case studies. The first was used to investigate the applicability of the statistical docking algorithm AutoDock to be used for the exploration of conformational space around the heme target. A theoretical *P. falciparum* 1-deoxy-D-xylulose-5-phosphate reductoisomerase (*Pf*DXR) enzyme model, constructed by the Biochemistry Department at Rhodes University, provided the ideal model to validate the AutoDock program. The protein model was accordingly subjected to rigorous docking simulations with over 30 different ligand molecules using the AutoDock algorithm which allowed for the docking algorithm's limitations to be ascertained and improved upon. This investigation facilitated the successful validation of the protein model, which can now be used for the rational design of new *Pf*DXR-inhibiting anti-plasmodial compounds, as well as enabling us to propose an improvement of the docking algorithm for application to the heme systems. The second case study was used to investigate the applicability of an *ab initio* molecular dynamics algorithm for simulation of bond breaking/forming events between the marine compounds and their heme target.

This validation involved the exploration of intermolecular interactions in a naturally occurring non-oligomeric zipper using the Car-Parrinello Molecular Dynamics (CPMD) method. This study allowed us to propose a model for the intermolecular forces responsible for zipper self-assembly and showcased the CPMD method's abilities to simulate and predict bond forming/breaking events.

Data from the computational analyses suggested that the interactions between marine isonitriles, isocyanates and isothiocyanates occur through bond-less electrostatic attractions rather than through formal intermolecular bonds as had been previously suggested. Accordingly, a simple bicyclic tertiary isonitrile (**5.14**) was synthesized using Kitano *et al*'s relatively underutilized isonitrile synthetic method for the conversion of tertiary alcohols to their corresponding isonitriles. This compound's potential for heme detoxification inhibition was then explored *in vitro* via the pyridine-hemochrome assay. The assay data suggested that the synthesized isonitrile was capable of inhibiting heme polymerization in a similar fashion to the known inhibitor chloroquine. Attempts to synthesize tricyclic analogues of **5.14** were unsuccessful and highlighted the limitation of Kitano *et al*'s isonitrile synthetic methodology.

Acknowledgements

I am grateful to my supervisors, Prof. Mike Davies-Coleman and Dr. Kevin Lobb, for their guidance, advice and patience. I thank Prof. Gregory Blatch for his direction regarding the work on the theoretical protein model validated in Chapter 3 and acknowledge with gratitude the assistance and support of Ryan Young, Sunny Sunassee, Jessica Goble, Byron Truscott, the Natural Products laboratory and members of the Rhodes University Chemistry Department. I thank the National Research Foundation (NRF) and the Deutscher Akademischer Austausch Dienst (DAAD) for their financial assistance. Finally, I thank Dr Rob Ridley for granting me permission to reproduce **Figure 1.1** and **Figure 1.2** in Chapter 1.

Unless specifically indicated to the contrary in the text, this thesis is my own original work. It has not been submitted for a degree at any other university.

Matthew Ralph Adendorff

TABLE OF CONTENTS

CHAPTER 1: INTRODUCTION

1.1	Malaria as a Disease of the Third World	1
1.2	Socio-Economic Impact	2
1.3	The Current Anti-Malarial Armoury	3
	1.3.1 Quinolines	3
	1.3.2 Artemisinins	4
	1.3.3 Antifolates	5
	1.3.4 Atovaquone/Proguanil	6
	1.3.5 Antibiotics	6
	1.3.6 Pyrimethamine	7
1.4	Drug Targeting	8
	1.4.1 The Food Vacuole	8
	1.4.2: The Folate Pathway	10
	1.4.3 The Apicoplast	11
	1.4.4 Mitochondrion Electron Transport	11
	1.4.5 Glycolysis	12
	1.4.6 Purine Salvage and Pyrimidine Synthesis	12
	1.4.7 Membrane Synthesis	13
	1.4.8 Transport Mechanisms	13
1.5	Resistance	14
	1.5.1 Chloroquine Resistance	14
	1.5.2 Antifolate Resistance	15
1.6	Call for New Drug Development	15
	1.6.1 Combination Therapy	15
	1.6.2 Development of Analogues of Existing Agents	16
	1.6.3 Compounds Active against Other Diseases	16
	1.6.4 Natural Products	16
1.7	Continued Relevance of Heme Detoxification as a Primary Drug Target	17
	1.7.1 β -Hematin and the Theories around its Formation	17
	1.7.2 Strategies to Find Inhibitors of β -Hematin Formation	18
	1.7.2.1 UV/Visible Spectra	18
	1.7.2.2 Infra-red	19
	1.7.2.3 X-Ray	19
1.8	Marine Anti-Malarial Isonitriles	20
	1.8.1 Previous Computational Methods to Predict Marine Isonitrile Inhibition of Hemozoin Formation	22
	1.8.1.1 Pharmacophore Structure	22
	1.8.1.2 Isonitrile Mode of Action	23
	1.8.1.3 Critical Evaluation of Computational Methods Used	23
1.9	Aims	25

CHAPTER 2: EVALUATIONS OF STEREOELECTRONIC PROPERTIES OF MARINE ANTI-MALARIALS AND THEIR HEME TARGETS

2.1	Modern Computational Methods for Electronic Structure Calculations	27
	2.1.1 Molecular Mechanics / Dynamics	27
	2.1.2 <i>Ab Initio</i> Methods	28
	2.1.3 DFT Methods	30
2.2	Construction of Chloroquine and Marine Isonitrile, Isocyanate and Isothiocyanate Electronic Models	30
2.3	Molecular Bonding Orbitals of Chloroquine and Marine Isonitriles, Isocyanates and Isothiocyanates	31
	2.3.1 HOMO and LUMO Orbital Maps of Chloroquine	31
	2.3.2 HOMO and LUMO Orbital Maps of Marine Compounds	32
2.4	Construction of Hematin and β-Hematin Dimer Electronic Models	38
	2.4.1 Selection of the Free Heme Model's Electronic State	38

2.5	Molecular Bonding Orbitals of Free Heme and β-Hematin Dimer Models	39
2.5.1	HOMO and LUMO Orbital Maps of Free Heme	39
2.5.2	HOMO and LUMO Orbital Maps of the β -Hematin Dimer	40
2.6	Molecular Electrostatic Topologies of Chloroquine and Marine Isonitriles, Isocyanates and Isothiocyanates	43
2.6.1	Electronic Topology of Chloroquine	43
2.6.2	Electronic Topologies of Marine Compounds	44
2.7	Molecular Electrostatic Topologies of Free Heme and the β-Hematin Dimer	50
2.7.1	Molecular Electrostatic Topology for Free Heme	50
2.7.2	Molecular Electrostatic Topology for β -Hematin Dimer	52
2.8	Summary	54

CHAPTER 3: EXPLORING THE CONFORMATIONAL SPACE OF INHIBITORS AROUND HEME STRUCTURES AS FOUND IN THE FOOD VACUOLE OF *P. FALCIPARUM*

3.1	Docking Algorithms	56
3.2	Validation of a Theoretical Malarial 1-Deoxy-D-xylulose-5-phosphate Reductoisomerase Enzyme Model	57
3.2.1	Introduction	57
3.2.2	Results and Discussion	61
3.3	Is AutoDock a Valid Docking Algorithm?	66
3.4	Statistical Docking Analyses of Chloroquine and Marine Isonitriles, Isocyanates and Isothiocyanates	67
3.4.1	Docking of Chloroquine	68
3.4.2	Docking of Marine Compounds	69
3.5	Summary	76

CHAPTER 4: INVESTIGATION OF INTER-MOLECULAR BOND-FORMING OR BREAKING EVENTS

4.1	Semi-Empirical "Forced-Binding" Analyses	78
4.1.1	Semi-empirical Methods	78
4.1.2	Energy Minimization Trajectories	79
4.1.2.1	<i>Isocyanates and Isothiocyanates</i>	79
4.1.2.2	<i>Isonitriles</i>	81
4.2	Molecular Dynamics	82
4.3	Application of an <i>Ab Initio</i> Molecular Dynamics Method to a Naturally Occurring Non-Oligomeric Molecular Zipper	84
4.3.1	Introduction	84
4.3.2	Thermodynamical Data	85
4.3.3	Steric Interferences and Energy Minimizations	86
4.3.4	Differences in Hydrogen Bonding Between Polymeric (R) and (S) Systems	88
4.3.5	Force Field Dynamics	89
4.3.6	Car-Parrinello Molecular Dynamics	92
4.3.6.1	<i>The (R) System</i>	92
4.3.6.2	<i>The (S) System</i>	94
4.3.7	Summary	95
4.4	Discussion of the CPMD Method's Efficacy	95
4.5	CPMD Simulations of Heme Systems	95
4.5.1	The Isocyanate and Isothiocyanate Systems	96
4.5.2	The Isonitrile System	97
4.6	What Is the Computational Evidence Telling Us?	98
4.7	The Validity of Wright <i>et al.</i>'s Pseudoreceptor Model	101

CHAPTER 5: SYNTHESIS OF MARINE ANTI-MALARIAL ISONITRILE ANALOGUES

5.1	Introduction	102
5.2	Kitano <i>et al</i>'s Synthesis of Isonitriles	105
5.3	Synthesis of Bicyclic Isonitrile	108
	5.3.1 Methylation of α -Tetralone	108
	5.3.2 Preparation of Bicyclic Isonitrile 5.14	109
5.4	Computational Analysis of Bicyclic Isonitrile 5.14	113
	5.4.1 Molecular Bonding Orbital Maps and Electrostatic Potential of 5.14	113
	5.4.2 Docking of Bicyclic Isonitrile 5.14	114
5.5	Hemochrome Assay of Bicyclic Isonitrile 5.14	115
5.6	A Tricyclic Precursor for Isonitrile Synthesis	116
	5.6.1 Preparation of γ , δ – Unsaturated Acid 5.41	117
	5.6.2 Hydrogenation of 5.41 to Afford the Saturated Acid 5.42	118
	5.6.3 Preparation of Tricyclic Ketone 5.39	118
	5.6.4 Methylation of Tricyclic Ketone 5.39	119
5.7	Attempted Synthesis of Tricyclic Isonitriles using the Method of Kitano <i>et al</i>	122
5.9	Conclusion	122

CHAPTER 6: EXPERIMENTAL PROCEDURES

6.1	Chapter Two Experimental	124
	6.1.1 General	124
	6.1.2 Construction of Chloroquine and Marine Isonitrile, Isocyanate and Isothiocyanate Electronic Models	124
	6.1.3 Molecular Bonding Orbitals of Chloroquine and Marine Isonitriles, Isocyanates and Isothiocyanates	125
	6.1.4 Construction of Hematin and β -Hematin Dimer Electronic Models	125
	6.1.5 Molecular Bonding Orbitals of Free Heme and β -Hematin Dimer Models	125
	6.1.6 Molecular Electrostatic Topologies of Chloroquine, Marine Isonitriles, Isocyanates and Isothiocyanates; and Heme Targets	126
6.2	Chapter Three Experimental	126
	6.2.1 General	126
	6.2.2 Validation of a Theoretical Malarial 1-Deoxy-D-xylulose-5-phosphate Reductoisomerase Enzyme Model	126
	6.2.2.1 <i>Ligand Model Preparation</i>	126
	6.2.2.2 <i>Receptor Model Preparation</i>	127
	6.2.2.3 <i>Generation of Grid Maps and Statistical Docking</i>	127
	6.2.3 Statistical Docking Analyses of Chloroquine and Marine Isonitriles, Isocyanates and Isothiocyanates	128
	6.2.3.1 <i>Ligand Model Preparation</i>	128
	6.2.3.2 <i>Receptor Model Preparation</i>	128
	6.2.3.3 <i>Generation of Grid Maps and Statistical Docking</i>	129
6.3	Chapter Four Experimental	129
	6.3.1 Semi-Empirical "Forced-Binding" Analysis	129
	6.3.2 Application of an <i>Ab Initio</i> Molecular Dynamics Method to a Naturally Occurring Non-Oligomeric Molecular Zipper	130
	6.3.2.1 <i>General</i>	130
	6.3.2.2 <i>Zipper Model Construction</i>	130
	6.3.2.3 <i>Energy Minimizations</i>	131
	6.3.2.4 <i>Car-Parrinello Molecular Dynamics</i>	132
	6.3.3 CPMD Simulations of Heme Systems	133
6.4	Chapter Five Experimental	133
	6.4.1 General	133
	6.4.1.1 <i>Analytical</i>	133
	6.4.1.2 <i>Chromatography</i>	134
	6.4.1.3 <i>Synthesis</i>	134
	6.4.1 Methylation of α -Tetralone	135
	6.4.2 Preparation of Bicyclic Isonitrile 5.14	136

6.4.3	Hemochrome Assay of Bicyclic Isonitrile 5.14	137
6.4.4	Preparation of γ , δ – Unsaturated Acid 5.41	138
6.4.5	Hydrogenation of 5.41 to Afford the Saturated Acid 5.42	139
6.4.6	Preparation of Tricyclic Ketone 5.39	140
6.4.7	Methylation of Tricyclic Ketone 5.39	141
6.4.8	Attempted Synthesis of Tricyclic Isonitriles using the Method of Kitano <i>et al</i>	142
6.4.9	Attempted Synthesis of 10-Isocyano-hispanalone 5.17	143
REFERENCES		144

LIST OF FIGURES

	Page
CHAPTER 1	
Figure 1.1	1
Figure 1.2	2
Figure 1.3	9
Figure 1.4	10
Figure 1.5	14
CHAPTER 2	
Figure 2.1	31
Figure 2.2	32
Figure 2.3	32
Figure 2.4	33
Figure 2.5	33
Figure 2.6	33
Figure 2.7	34
Figure 2.8	34
Figure 2.9	35
Figure 2.10	35
Figure 2.11	36
Figure 2.12	36
Figure 2.13	37
Figure 2.14	37
Figure 2.15	39
Figure 2.16	40
Figure 2.17	41
Figure 2.18	41
Figure 2.19	42
Figure 2.20	43
Figure 2.21	44
Figure 2.22	45
Figure 2.23	45
Figure 2.24	45
Figure 2.25	46
Figure 2.26	46
Figure 2.27	46
Figure 2.28	47
Figure 2.29	47
Figure 2.30	47
Figure 2.31	48
Figure 2.32	48
Figure 2.33	49
Figure 2.34	50
Figure 2.35	51
Figure 2.36	52
Figure 2.37	52
Figure 2.38	53
Figure 2.39	53

Figure 2.40	The negative oxygen linkages, indicated by their red colouring, are circled and will be approached at 45° to the plane of the porphyrin rings. The arrow indicates the approach vector of molecules possessing suitably positive MEPs.	54
 CHAPTER 3		
Figure 3.1	The different conformations adopted by ligand 3.23 (green), compact (left) and extended (right), during docking with <i>Ec</i> DXR and <i>Pf</i> DXR respectively in the presence of NADPH (second tubular structure).	64
Figure 3.2	Interaction between ligand 3.2 (coloured tubular structure) and “hatch” residues in <i>EC</i> DXR, in the presence of NADPH (green).	65
Figure 3.3	Interaction between ligand 3.2 (coloured tubular structure) and “hatch” residues in <i>Pf</i> DXR.	65
Figure 3.4	Lowest energy conformations for chloroquine docked against free heme (left) and the B-hematin dimer (right).	68
Figure 3.5	Lowest energy conformations for 1.30 docked against free heme (left) and the β-hematin dimer (right).	69
Figure 3.6	Lowest energy conformations for 1.31 docked against free heme (left) and the β-hematin dimer (right).	69
Figure 3.7	Lowest energy conformations for 1.32 docked against free heme (left) and the β-hematin dimer (right).	70
Figure 3.8	Lowest energy conformations for 1.33 docked against free heme (left) and the β-hematin dimer (right).	70
Figure 3.9	Lowest energy conformations for 1.34 docked against free heme (left) and the β-hematin dimer (right).	71
Figure 3.10	Lowest energy conformations for 1.35 docked against free heme (left) and the β-hematin dimer (right).	71
Figure 3.11	Lowest energy conformations for 1.36 docked against free heme (left) and the β-hematin dimer (right).	72
Figure 3.12	Lowest energy conformations for 1.37 docked against free heme (left) and the β-hematin dimer (right).	72
Figure 3.13	Lowest energy conformations for 1.38 docked against free heme (left) and the β-hematin dimer (right).	73
Figure 3.14	Lowest energy conformations for 1.39 docked against free heme (left) and the β-hematin dimer (right).	73
Figure 3.15	Lowest energy conformations for 1.40 docked against free heme (left) and the β-hematin dimer (right).	74
Figure 3.16	Lowest energy conformations for 1.41 docked against free heme (left) and the β-hematin dimer (right).	74
Figure 3.17	Lowest energy conformations for 1.42 docked against free heme (left) and the β-hematin dimer (right).	75
Figure 3.18	Lowest energy conformations for 1.30 docked against free heme (left) and the β-hematin dimer (right).	75
 CHAPTER 4		
Figure 4.1	The initial (left) and AM1 optimized (right) configurations for isocyanate 1.33 .	79
Figure 4.2	The initial (left) and AM1 optimized (right) configurations for isothiocyanate 1.31 .	80
Figure 4.3	The initial (left) and AM1 optimized (right) configurations for isothiocyanate 1.39 .	80
Figure 4.4	The initial (left) and AM1 minimized (right) configurations for isonitrile 1.39 .	81
Figure 4.5	X-ray crystallography data showing the zipper network inherent in crystals of the (R) epimer (left). The hydrogen bonds act as the teeth in a normal zipper (right).	85
Figure 4.6	Enhancement of the sterically unfavourable proximities of methyl groups located at the C13 position of 4.3 on the (S) tetrameric system before energy minimization.	87
Figure 4.7	The starting (left) and AM1 optimized (right) arrangements of the (S) tetrameric system.	87

Figure 4.8	Proximity permitted hydrogen bonds (dotted blue lines) between hydroxyl groups on the minimized (R) tetrameric system.	88
Figure 4.9	Proximity permitted hydrogen bonds (dotted blue lines) between hydroxyl groups on the minimized (S) tetrameric system.	89
Figure 4.10	Interatomic distances monitored as a function of dynamical time. The (R) tetramer was used as a template for this figure and will not exhibit all of the hydrogen bonds illustrated here.	89
Figure 4.11	Extended zipper network formation, shown as red-white bonds along the central axis.	92
Figure 4.12	Stage one of transfer with hydrogen-oxygen bond at minimum extension. The proton donor is the lower of the two hydroxyl groups within the circle (orange rectangle), the acceptor is the higher (blue rectangle) and the arrow indicates direction of the zipper hydrogen bond network.	93
Figure 4.13	Stage two of transfer with the hydrogen-oxygen bond of the donor hydroxyl group (orange rectangle) extending towards the acceptor.	93
Figure 4.14	Stage three of transfer with the proton migrating from the donor hydroxyl group to the acceptor (blue rectangle).	93
Figure 4.15	Disruption of zipper hydrogen bond network during finite temperature CPMD run (hydrogens not shown). The green circle indicates the hydrogen-bonded micro-clusters which comprise the formation of a linear (S) crystal network.	94
Figure 4.16	Starting arrangement (left) and the system after after 3000 steps of CPMD dynamics for the isothiocyanate (1.39) – FP system.	96
Figure 4.17	Starting arrangement (left) and the system after after 3000 steps of CPMD dynamics for the isocyanate (1.33) – FP system.	96
Figure 4.18	Starting and 563 rd dynamical frame configurations for CPMD dynamics run on the isothiocyanate (1.39) – FP system.	97
Figure 4.19	The very similar electrostatic potentials of structures 1.32 (left) and 1.33 (right).	99
CHAPTER 5		
Figure 5.1	¹³ C NMR (150 MHz) spectra of 5.35 (bottom) and 5.36 (top).	109
Figure 5.2	¹³ C NMR (150 MHz) spectra of 5.14 (top), 5.36 (middle) and 5.35 (bottom).	110
Figure 5.3	Relative intensity of the isocyanato peak to the other peaks in commercial <i>tert</i> -butyl isocyanide (5.37 , Frame A). Structure of the isocyanato triplet caused by ¹³ C - ¹⁴ N coupling (Frame B).	111
Figure 5.4	¹³ C NMR (150 MHz) spectrum of 5.14 , showing the isocyanato triplet at δ_C 167.9	112
Figure 5.5	Electronic density maps of 5.14 HOMO and LUMO molecular orbitals.	113
Figure 5.6	Molecular electrostatic potential (right) superimposed on a map of total electronic density (left) for structure 5.14 .	113
Figure 5.7	Lowest energy conformations for 5.14 docked against free heme (left) and the β -hematin dimer (right).	114
Figure 5.8	Absorption versus wavelength plots for the hemochrome assay of isonitrile 5.14 (green) and chloroquine (blue) after one hour of incubation. The absorptions at 404 nm are the Soret bands for the three systems (purple arrow) and the red line indicates the reference zero-line.	115
Figure 5.9	A section of the NOESY spectrum for 5.43 . The increased interatomic distance between the methyl (blue) protons and the methine proton at position C-9 (orange) results in no correlation between the two signals in the spectrum.	120
Figure 5.10	A section of the NOESY spectrum for 5.43 . The reduced interatomic distance between the methyl (blue) protons and the methine proton at position C-9 (orange) results in correlation between the two signals in the spectrum (orange rectangle).	121

LIST OF GRAPHS

	Page
CHAPTER 3	
Graph 3.1	Graphs of binding affinity versus number of hydrogen bonds for <i>EcDXR</i> (A) and <i>PfDXR</i> (B), along with plots of binding affinity versus experimental IC ₅₀ . The coloured quadrants contain those ligands with optimal binding qualities. The red circles the especially poor binding ligands 3.29 – 3.32 . 62
CHAPTER 4	
Graph 4.1	Plot of interatomic distance versus dynamical time for the (R) tetrameric system at 300 K. 90
Graph 4.2	Plot of interatomic distance versus dynamical time for the (S) tetrameric system at 300 K. 90

LIST OF TABLES

CHAPTER 1	
Table 1.1	Structures of marine anti-malarial isonitriles, isocyanates and isothiocyanates used by Wright <i>et al</i> to generate their pseudoreceptor model and their IC ₅₀ values against <i>P. falciparum</i> strain D6. 20
CHAPTER 3	
Table 3.1	Structures of the ligands used as a test set for the theoretical <i>PfDXR</i> model constructed by Goble and co-workers. 59
CHAPTER 4	
Table 4.1	AM1 Thermochemical data (298K) for a polymeric series of the (R) and (S) epimers (kcal/mol). 86
CHAPTER 5	
Table 5.1	<i>In vitro</i> anti-malarial activity of isonitriles 5.1 – 5.10 against <i>P. falciparum</i> (strain NF - 45) 103

LIST OF SCHEMES

CHAPTER 5	
Scheme 5.1	Kitano <i>et al</i> 's first procedure for the conversion of a tertiary alcohol (5.18) to an isonitrile (5.19). (a) TMSCN, ZnX ₂ , DCM; (b) TBAF. 105
Scheme 5.2	Kitano <i>et al</i> 's modified procedure for the conversion of a tertiary alcohol (5.22) to an isonitrile (5.23). 106
Scheme 5.3	Proposed mechanism for the conversion of a tertiary alcohol (5.26) to the corresponding isonitrile (5.31) via Kitano <i>et al</i> 's procedure. 107
Scheme 5.4	Synthesis of tertiary alcohol 5.36 . (a) MeLi, anhydrous THF, -78°C. 108
Scheme 5.5	Synthesis of isonitrile 5.14 . (a) TMSCN, AgClO ₄ , anhydrous DCM. 109
Scheme 5.6	Synthesis of 2,3-dihydro-1H-phenalen-1-one (5.39). (a) diethyl succinate, KO ^t Bu, ^t BuOH, reflux; (b) AcOH, HCl, reflux; (c) Pd-C (5%), H ₂ ; (d) PPA, 130°C. 117
Scheme 5.7	Synthesis of the diastereomers 5.43 and 5.44 (enantiomers not shown). (a) MeLi, anhydrous THF, -78°C. 120

LIST OF ABBREVIATIONS

3D	three dimensional
AcOH	acetic acid
AIMD	<i>ab initio</i> molecular dynamics
AM1	Austin Model 1
AMBER	assisted model building with energy refinement
amu	atomic mass units
Asn	asparagine
atm	atmospheres
B3LYP	Becke-Lang-Yee-Parr
BOA	Born-Oppenheimer approximation
br	broad
calcd	calculated
CPMD	Car-Parrinello molecular dynamics
CQ	chloroquine
d	doublet
DCM	dichloromethane
DFT	density functional theory
DHFR	dihydrofolate reductase
DXR	1-deoxy-D-xylulose-5-phosphate synthetase
DXP	1-deoxy-D-xylulose-5-phosphate
<i>EcDXR</i>	<i>E. coli</i> 1-deoxy-D-xylulose-5-phosphate reductoisomerase enzyme
EIMS	electron impact mass spectroscopy
Eq	equation
equiv	molar equivalents
eV	electron volt
FOS	fosmidomycin
FP	free heme
FT	Fourier transform
Gly	glycine
h	hour(s)
HD	β -hematin dimer
HEPES	4-(2-hydroxyethyl)-1-piperazine ethanesulfonic acid
HF	Hartree-Fock
His	histidine
HOMO	highest occupied molecular orbital
HPLC	high performance liquid chromatography
HREIMS	high resolution electron impact mass spectroscopy
HRFAB	high resolution fast atomic bombardment mass spectroscopy
IC ₅₀	median inhibitory constant
IR	infra-red
KO ^t Bu	potassium <i>tert</i> -butylate
KS	Kohn-Sham
LCAO	linear combination of atomic orbitals
LUMO	lowest unoccupied molecular orbital
Lys	lysine
m	multiplet
MD	molecular dynamics
MeLi	methyllithium
MeOH	methanol
MEP	molecular electrostatic potential

MEP	2-C-methyl-erythritol 4-phosphate
min	minute(s)
MM	molecular mechanics
mmol	millimoles
MO	molecular orbital
mol	moles
MP2	second order Møller-Plesset
NADPH	nicotinamide adenine dinucleotide phosphate
NaOAc	sodium acetate
NMR	nuclear magnetic resonance
NOESY	Nuclear Overhauser enhancement spectroscopy
ONIOM	our own N-layered integrated molecular orbital + molecular mechanics
PBE	Perdew-Burke-Ernzerhof
<i>PfDXR</i>	<i>P. falciparum</i> 1-deoxy-D-xylulose-5-phosphate reductoisomerase
PM3	Paramatized Model number 3
PPA	polyphosphoric acid
ppm	parts per million
q	quartet
QSAR	quantitative structure activity relationship
R	alkyl group
rt	room temperature
s	singlet
sat.	saturated
SE	semi-empirical
Ser	serine
t	triplet
^t BuOH	<i>tert</i> -butanol
<i>tert</i>	tertiary
THF	tetrahydrofuran
TLC	thin layer chromatography
TMSCN	trimethylsilyl cyanide
TMSO	trimethyl-silate
TMSOH	trimethyl-silanol
TS	thymidilate synthase

GENERAL INTRODUCTION

1.1 Malaria as a Disease of the Third World

Each year over 2.2 billion people are exposed to the threat of *Plasmodium falciparum* malaria, resulting in approximately 500-660 million clinical cases and 1-3 million deaths, mostly of children.¹⁻⁵ Consequently, malaria may be considered the pre-eminent parasitic tropical disease and one of the top three communicable disease killers in the world.^{2,4,6} Globally, the pattern of malaria transmission is centred in the tropics and sub-tropics.⁷ The largest malaria burden is borne by sub-Saharan Africa,^{2,5} largely due to the high transmission capacity of Africa's primary mosquito vectors, i.e. the *Anopheles gambiae* complex of species, and their anthropophilic (human biting) tendencies.² Although many successful programmes have been conducted at country level to combat the parasite, the world is currently facing a rapidly increasing malarial threat. Potential causes for this include: population movement into malaria areas, weakening of public health systems in poorer countries and disruptive agricultural practices (i.e. dam building, irrigation schemes and deforestation). With the increase of populations within malaria zones, it is estimated that without decisive intervention strategies there will be a doubling of the number of clinical cases over the next 20 years.⁸

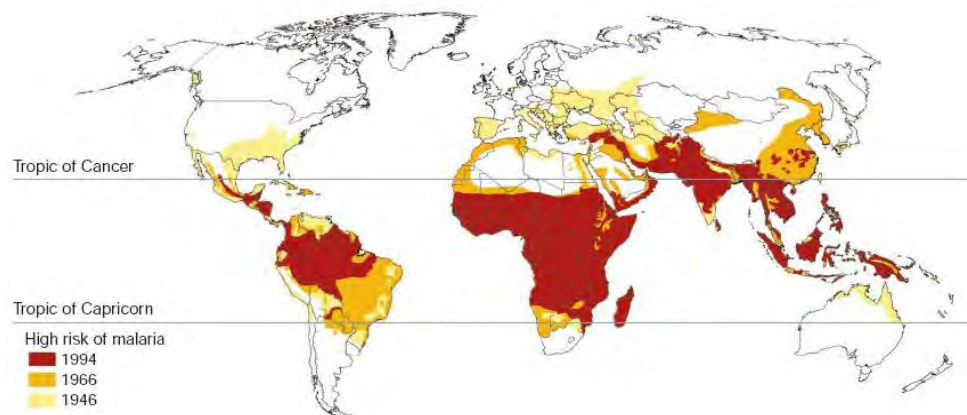


Figure 1.1: Global distribution of *P. falciparum* malaria. Reproduced with permission.²

1.2 Socio-Economic Impact

Human societies have prospered least where malaria has prospered most.² A disturbing correlation can be seen between malaria and poverty worldwide when observing the global distribution of countries' gross domestic product per capita, as in Figure 2. Essentially, malaria endemic countries have lower economic growth rates due to several impediments which the disease affords, namely, disrupted population growth, decreased worker productivity, increased absenteeism, premature mortality and high medical costs.⁷ Malaria also affects the movement of people, with the risk of infection having a profound influence on human population mobility and the construction of new settlements.² This consequently will have an impact on development due to the suppression of economic linkages between malaria and non-malaria zones. Industries which are most affected by malaria include: tourism, mining, agriculture and manufacturing. Economically, the malaria-poverty relationship is a bi-directional one with both being partly responsible for the other and this double causality presents a definite challenge to malaria endemic countries.^{2,5}

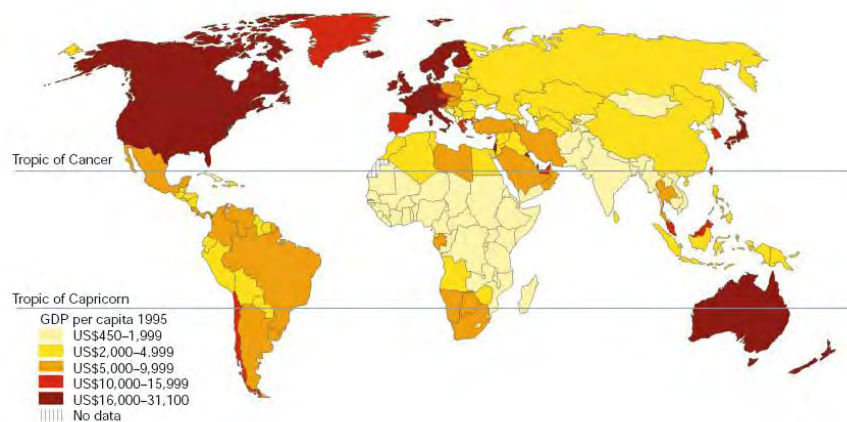
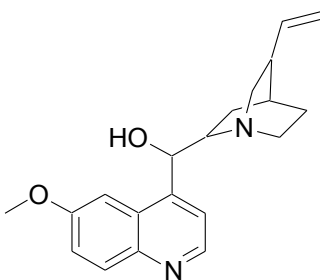
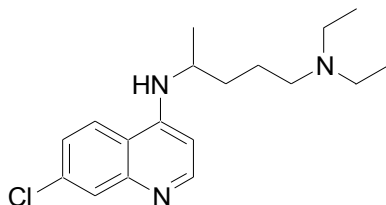
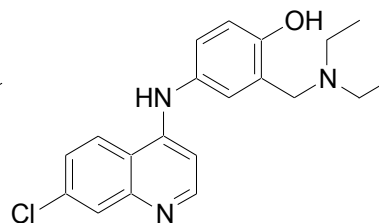


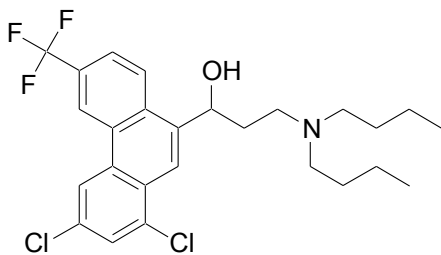
Figure 1.2: Global GDP distribution. Reproduced with permission.²

1.3 The Current Anti-Malarial Armoury

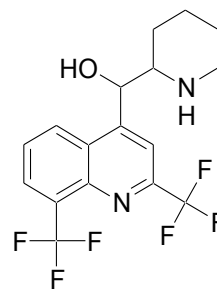
1.3.1 Quinolines

Quinoline anti-malarials originate from the compound quinine (**1.1**) which is an active anti-malarial natural product found in the bark of the Peruvian *Cinchona* tree.⁹ Due to toxic liabilities associated with **1.1** and the requirement of a 7 day dosage scheme, the fully synthetic 4-aminoquinoline anti-malarials (**1.2 – 1.5**) were developed.⁷ Most notable among these are chloroquine (CQ, **1.2**), which has been the mainstay of *P. falciparum* malaria chemotherapy for decades⁵, and the later developed amodiaquine (**1.3**). These two drugs are inexpensive and only require a 3 day dosage scheme.^{7, 10-12} The use of amodiaquine was limited after the mid 1980s due to the potential development of agranulocytosis in adults when used as a prophylactic; though due to its efficacy against all but the most highly chloroquine-resistant strains, there has been a recent increase in its use.¹³ Halofantrine (**1.4**) and mefloquine (**1.5**) are structurally related drugs used against chloroquine-resistant strains, however resistance to these drugs is developed rather rapidly and certain potential side-effects have been noted, including ventricular arrhythmias for halofantrine and neuropsychiatric irregularities for mefloquine.^{14, 15}

Quinine (**1.1**)Chloroquine (**1.2**)Amodiaquine (**1.3**)



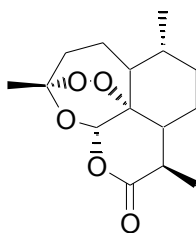
Halofantrine (1.4)



Mefloquine (1.5)

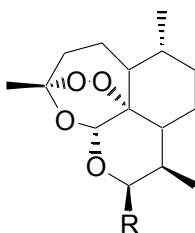
1.3.2 Artemisinins

Artemisinin (1.6) is the anti-malarial natural product in the Chinese medicinal herb *Artemisia annua*.^{13,16} Three synthetic derivatives, artemether (1.7), arteether (1.8) and artesunate (1.9) also exhibit anti-malarial activity. All these compounds are metabolized to dihydroartemisinin in the body which then acts rapidly against the sexual stages of the parasite.⁷ Due to the short half-lives of both the parent semi-synthetic compounds and the dihydroartemisinin (1.10) metabolic product, successful anti-malarial treatment with these compounds on their own would take 5-7 days. As a result, artemisinins are being used in combination with longer half-life drugs to reduce treatment time and to prevent resistance development via the destruction of the reproductive parasites by the artemisinins.¹⁷

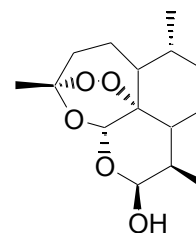


Artemisinin

(1.6)



Artemisinin Derivatives

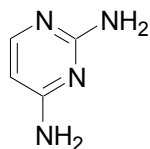
R = -OCH₃ (1.7)R = -OCH₂CH₃ (1.8)R = -OCO(CH₂)₂COOH (1.9)

Dihydroartemisinin

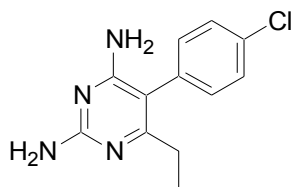
(1.10)

1.3.3 Antifolates

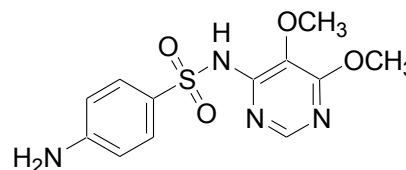
Antifolates are not derived from a natural product and were developed through knowledge of cell biology and synthetic medicinal chemistry in which a library of synthetic chemicals were found to disrupt the folate metabolism pathway within the parasite.¹⁸ The most significant folate anti-malarial at present is the combination of 2,4-diaminopyrimidine (**1.11**) derivative pyrimethamine (**1.12**) (a dihydrofolate reductase inhibitor) and sulphadoxine (**1.13**) (a sulphonamide which disrupts dihydroopteroate synthase activity).⁷



2,4-Diaminopyrimidine

(1.11)

Pyrimethamine

(1.12)

Sulphadoxine

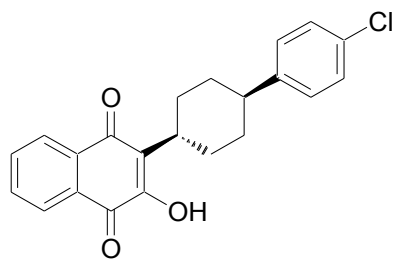
(1.13)

These two compounds act synergistically and enhance each other's activity whilst preventing the development of resistance. It is believed that the long half-lives of these compounds may allow for effective intermittent treatment of pregnant women; however this remains to be proven.¹⁹ Unfortunately, resistance has been shown to develop rapidly when this combination is used extensively and there is a potential for allergic reaction to the sulphur component when used as a prophylactic which may lead to a painful blistering of the skin, known as Stevens-Johnson syndrome.¹³

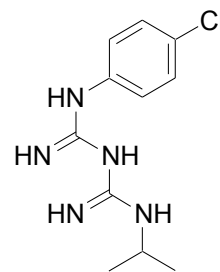
1.3.4 Atovaquone/Proguanil

The fixed-dose combination of atovaquone (**1.14**) and proguanil (**1.15**) was developed in a similar fashion to the antifolates and is used to disrupt mitochondrial electron transport. Due to the rapid onset of atovaquone resistance via a point mutation in cytochrome *c* reductase, proguanil (**1.15**) was added to allow for synergistic activity preventing the rapid development of this resistance.²⁰

²¹ The combination of atovaquone and proguanil is used primarily as a prophylactic and its high price unfortunately prevents it from being used for widespread treatment in developing countries.



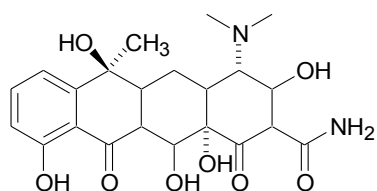
Atovaquone
(1.14)



Proguanil
(1.15)

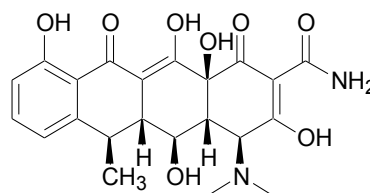
1.3.5 Antibiotics

Common antibiotics, e.g. tetracycline (**1.16**), doxycycline (**1.17**) and clindamycin, used routinely against bacterial protein synthesis, are increasingly being used in combination with anti-malarial treatments to augment their activity by inhibiting prokaryote-like protein synthesis in the apicoplast organelle.^{22, 23}



Tetracycline

(1.16)



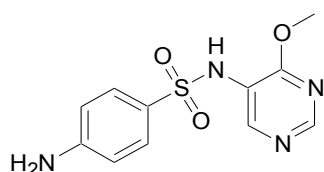
Doxycycline

(1.17)

Two such combinations being employed in south-east Asia are quinine (1.1) and tetracycline (1.16) or doxycycline (1.17). The use of these combinations in Africa is limited however as the antibiotics are contraindicated in children under the age of 8 years.¹³

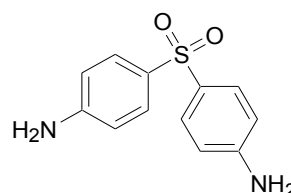
1.3.6 Pyrimethamine

Pyrimethamine (1.12) is formulated in a fixed combination with sulphadoxine (1.13), sulphalene (1.18) or dapsone (1.19).⁵



Sulphalene

(1.18)



Dapsone

(1.19)

The most widely used combination is that of pyrimethamine and sulphadoxine as it is cheap, practical (only one dose required) and highly effective in much of Africa. Sulphadoxine is now the frontline anti-malarial in several African countries, though it is particularly prone to the rapid emergence of resistance.²⁴

1.4 Drug Targeting

Successful chemotherapy of disease organisms most often exploits differences in the metabolisms of the pathogen and its host.²⁵ For example, in treating *P. falciparum* malaria, several enzymes from a number of the organism's biochemical pathways have been identified as potential drug targets, for example

1.4.1 The Food Vacuole

During the 48-hour invasion, growth and release from the infected erythrocyte, *P. falciparum* will digest up to 80% of the haemoglobin within the blood cell.²⁶ The degradation of haemoglobin takes place in a lysosomal food vacuole and is facilitated by the action of aspartic proteases (plasmepsins),²⁷ the cysteine protease falcipain 2²⁸ and a metallopeptidase.²⁹ The by-products of this degradation are free heme moieties (FP) and hydrogen peroxide (H₂O₂) which are both toxic to the parasite, thus requiring neutralization or removal. The parasite disposes of FP partly through sequestration into a crystalline form, hemozoin, and partly through non-enzymatic degradation processes.³⁰⁻³³ CQ and a number of other quinoline anti-malarials inhibit the formation of hemozoin and the non-enzymatic degradation of FP by interactions with glutathione and H₂O₂. They also inhibit the degradation of H₂O₂, facilitated by the peroxidase action of the FP group in its Fe (IV) ferryl intermediate state. Buller *et al* have proposed, through crystallographic studies on synthetic hemozoin (β -hematin), a non-covalent quinoline drug family specific binding site located at the end face associated with fastest crystal growth.³⁴ This research investigated the factors influencing the different activities of the synthetic quinolines and suggested that it is the adsorption of these molecules to the growing hemozoin crystal face that effects their inhibitory action. The binding of the FP moieties by these compounds (see Figure 3) thereby prevents their sequestration into inert hemozoin and inhibits their degradation by glutathione/H₂O₂ as well their

peroxidase action. When the concentration of the detergent-like FP molecules gets too high, they break down the vacuole plasma membrane, killing the parasite.³⁰

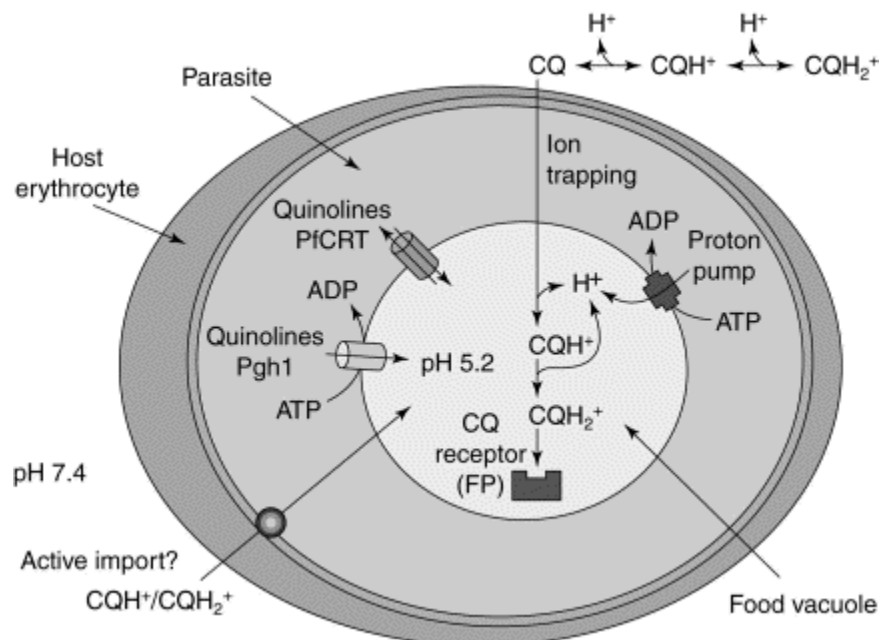


Figure 1.3: CQ action within the parasite food vacuole.²⁵

A second class of compounds which act within the food vacuole are the artemisinins (1.6 – 1.10) which, when subjected to the acidic pH (5.2) of this organelle, produce free radicals which then damage the vacuole and the cell. Artemisinin anti-malarials contain an endoperoxide bridge which undergoes an iron-catalyzed decomposition to form the damage-inducing free radicals.⁴

1.4.2 The Folate Pathway

In *P. falciparum*, the conversion of 2'-deoxyribosyluracil monophosphate (**1.20**) to 2'-deoxyribosylthymine monophosphate (**1.21**) is essential for DNA synthesis.⁵ This conversion is achieved through donation of a methyl group by 5,10-methylenetetrahydrofolate (**1.22**) which is in turn oxidised to 7,8-dihydrofolate (**1.23**) by thymidylate synthase (TS). This oxidation product must be reduced back to **1.22** via 5,6,7,8-tetrahydrofolate (**1.24**) and this reaction's rate limiting step (conversion of **1.22** into **1.24**) is catalyzed by the enzyme dihydrofolate reductase (DHFR). Antifolate anti-malarials, e.g. pyrimethamine (**1.12**), compete with **1.22** for DHFR by binding to the protein's active site with a higher affinity.³⁵

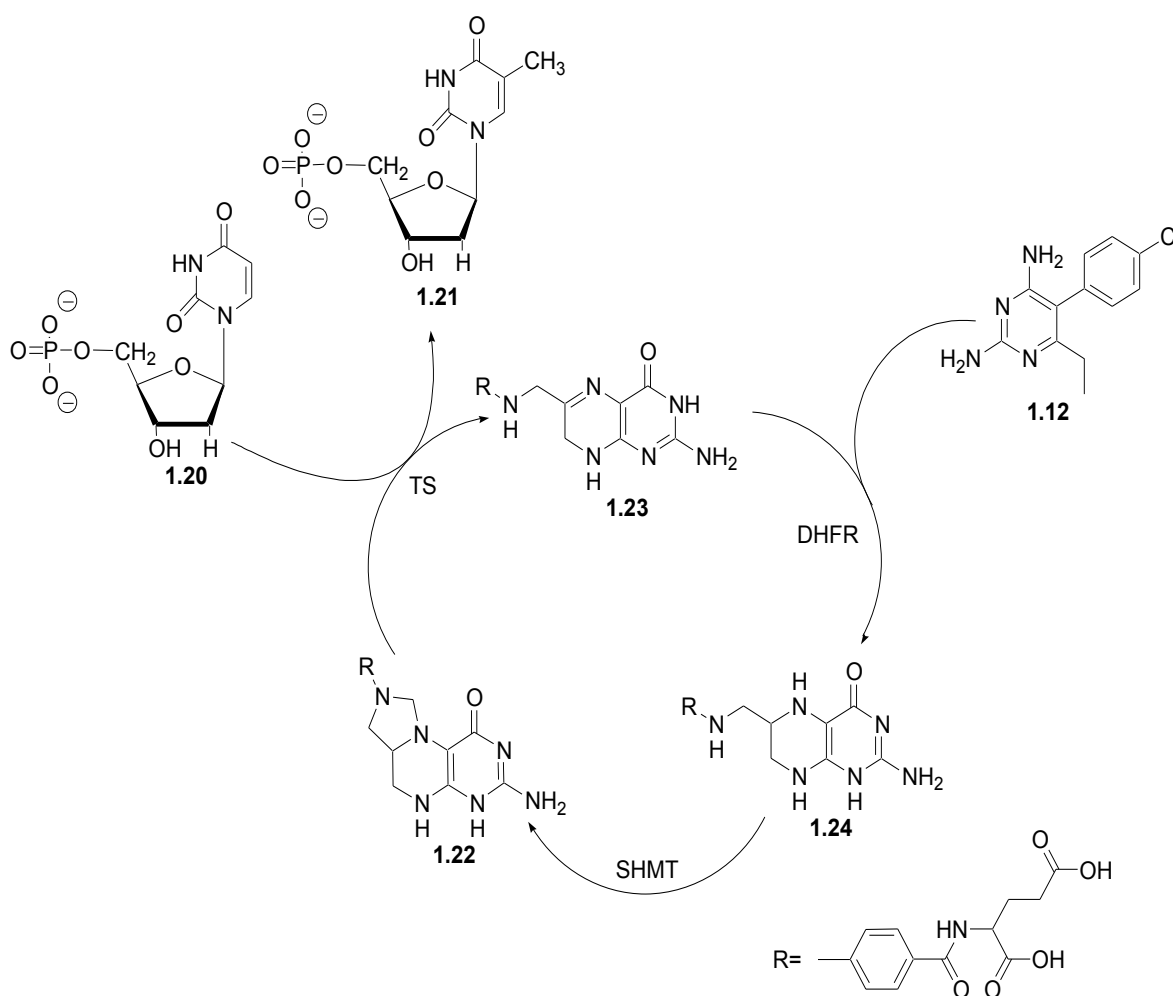


Figure 1.4: The malarial folate pathway.³⁵

1.4.3 The Apicoplast

The apicoplast is a plastid organelle within the cytosol of *P. falciparum* which contains a 35-kilobase circular genome encoding elements used in prokaryotic transcription and translation systems.³⁶ Several key metabolic pathways within the apicoplast have been identified which, if disrupted, can cause rapid cell death. The first of these is the non-mevalonate pathway which is responsible for synthesising isopentenyl diphosphate units and which can be disrupted by antibiotic inhibition of the enzyme 1-deoxy-D-xylulose-5-phosphate synthetase (DXP).³⁷ Isopentenyl diphosphate units are biosynthesized in the human host by the mevalonate pathway thereby making the inhibition of DXP activity parasite specific. Details of the non-mevalonate pathway in *P. falciparum* are discussed in Chapter 3. The second metabolic pathway target is the type II fatty acid biosynthetic pathway³⁸ which can be disrupted by inhibition of the condensing enzymes (Fab B, Fab F and Fab H) and the enoyl-acyl-carrier protein reductase.³⁹

1.4.4 Mitochondrion Electron Transport

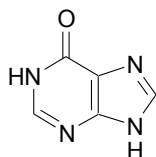
The *Plasmodium* mitochondrion is morphologically unusual as it has no oxidative phosphorylation activity and has an incomplete electron transport chain linked to metabolically significant redox reactions.⁴⁰ This is believed to be due to *Plasmodium* parasites tending to reside in oxygen-deficient environments, thereby relying on glycolysis for ATP production.⁷ One of the reactions linked to the mitochondrial electron transport chain is the coupling of cytochrome c reductase to dihydroorotate dehydrogenase, an enzyme crucial to nucleotide biosynthesis. Anti-malarials such as the atovaquone/proguanil combination and the β -methoxyacrylate class of compounds³⁹ disrupt the pathway by interfering with electron transport in the parasite's mitochondria.⁷

1.4.5 Glycolysis

As mentioned previously, *P. falciparum* relies on glycolysis for production of cellular energy. The enzyme lactate dehydrogenase has been structurally characterized and its binding site for the cofactor NADH thus provides a target for inhibition.⁴² Inhibition of this pathway has a lethal effect on the parasite as its energy source is effectively severed.

1.4.6 Purine Salvage and Pyrimidine Synthesis

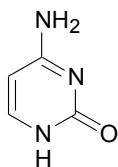
P. falciparum cannot synthesize purines and thus relies on salvaging host purines to facilitate nucleotide synthesis. The main source of purines is hypoxanthine (**1.25**) and so the enzyme hypoxanthine-guanine phosphoribosyltransferase also provides a target for anti-malarials.⁴³



Hypoxanthine

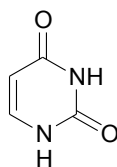
(1.25)

In contrast, the parasite is unable to salvage pyrimidines, e.g. cytosine, uracil and thymine (**1.26-1.28**), and is forced to biosynthesize these *de novo*. As this pathway is also linked to mitochondrial electron transport, it provides a double target for anti-malarials.²⁵



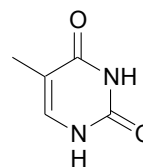
Cytosine

(1.26)



Uracil

(1.27)

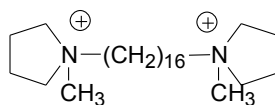


Thymine

(1.28)

1.4.7 Membrane Synthesis

Intra-erythrocytic malaria parasites undergo extensive phospholipid synthesis to produce the necessary amount of membranes for enclosing the food vacuole, cytosol and sub-cellular compartments. The lipid in greatest abundance within these plasmodial membranes is phosphatidylcholine which requires choline molecules from the host. The choline transport pathway thereby provides a target for anti-malarials such as G25 (**1.29**), the lead compound in the development of a membrane synthesis-inhibiting agent.⁴



G25

(1.29)

1.4.8 Transport Mechanisms

Malaria-infected erythrocytes display increased solute (permeability due to parasite induced new permeation pathways) and to increased activity of endogenous transporters.⁴⁴ This permeability can be exploited to introduce anti-malarial compounds into the cell more easily. One such method is through conjugation of these compounds to dinucleoside phosphate dimers to improve selective access to parasite targets.⁴⁵ Essentially, transport mechanisms provide a means to enhance the efficacy of anti-malarial drug targeting.

1.5 Resistance

The arrival of resistance on a global scale (as illustrated in Figure 5) towards chloroquine has highlighted the ability of *P. falciparum* to resist anti-malarial chemotherapies and has drawn attention to the possibility of similar resistances developing against other therapies as well, e.g. sulphadoxine and pyrimethamine (see Figure 5).⁷

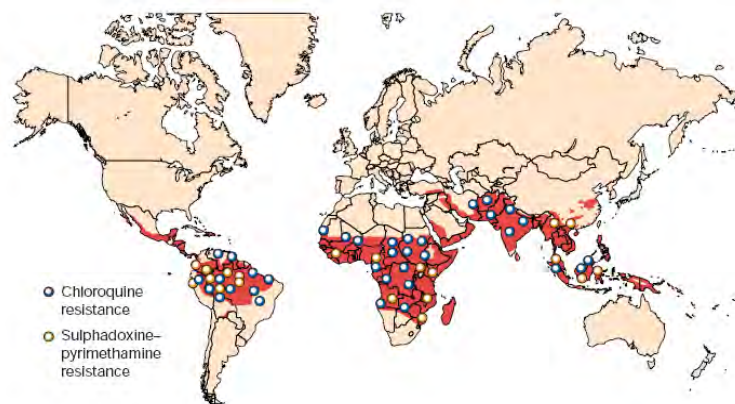


Figure 1.5: Global distribution of resistance to front-line anti-malarials.⁷

The following examples demonstrate how resistance is developed and the kinds of issues anti-malaria drug design faces by virtue of this.

1.5.1 Chloroquine Resistance

Before chloroquine can exert its drug action within the food vacuole of the plasmodium, it must first be transported across the vacuole membrane by a putative transporter protein, *PfCRT*. Fidock *et al* have shown that a single point mutation within this protein region is enough to confer resistance *in vitro*, whilst several mutations are required for clinical resistance.⁴⁶ Although chloroquine is now severely compromised by resistance, it is believed that the relatively long time required to develop this resistance was due to its non-enzyme-targeting action.⁴

1.5.2 Antifolate Resistance

Pyrimethamine is an example of a drug which has an enzyme as its target, DHFR. Sirawaraporn has shown that *P. falciparum* can undergo spontaneous mutation of its *dhfr* gene and the resulting mutants can proliferate if they have an advantage over their parent compound, usually enhanced by drug pressure.⁴⁷ Each of the mutations increases the IC₅₀ of pyrimethamine for the parasite and the development of different mutations from region to region makes it difficult to control mutant strains. Although pyrimethamine is generally used in combination with a compound like sulphadoxine, which inhibits an enzyme higher in the folate pathway, dihydroopteroate synthetase, mutations in the *dhps* gene permits sulphadoxine resistance to develop in a similar fashion. This rapid development of resistance to enzyme-targeting compounds presents a serious problem to new drug development as most of the newer treatments have enzymatic pathways as their targets.⁴

1.6 Call for New Drug Development

Considering the increase in resistance to currently existing agents,^{3,48} there is a general consensus that new developments in anti-malarial chemotherapy are needed.^{25,49} The following methodologies represent the potential paths which may be taken to develop new drugs.

1.6.1 Combination Therapy

Combination therapies coupling newer agents with older ones have shown great potential for parasite control, e.g. atovaquone (new) and proguanil (old). The use of combination therapy offers two important potential advantages. Firstly, the coupling of drug actions should permit synergistic activity against the parasite and secondly, the progression of resistance to the new agents should be slowed.⁴

1.6.2 Development of Analogues of Existing Agents

Chemical modifications of existing anti-malarial compounds can facilitate an improvement in their efficacy. The advantage of this approach is that knowledge of the parent compound's target and mode of action are not required, though such information would assist in streamlining the modification process. This methodology has been responsible for the development of many existing agents, e.g. chloroquine, primaquine and mefloquine were all discovered through structural modifications to quinine.⁵⁰

1.6.3 Compounds Active against Other Diseases

Agents which find use in the treatment of other diseases may act against orthologs (genes in different species that are similar to each other) of their normal targets within malarial metabolic systems. The advantage of this approach is that whatever the mechanism of these compounds are, they have been developed for a human disease and so should be more amenable to development into new drugs. Examples of compounds which were designed for antibiotic action and were later found to exhibit anti-malarial behaviour are folate antagonists and tetracycline.^{22,23,35}

1.6.4 Natural Products

Isolation of compounds from naturally occurring anti-malarial extracts has provided drugs such as quinine and artemisinin, two of the most important drug therapies today. Modifications of these parent compounds produced the quinolines and the artemisinin derivatives, thus demonstrating the wealth of potential agents which natural product isolations can afford.⁵² The role of marine organisms as a source of new anti-malarials to disrupt heme detoxification will be discussed in Section 1.8.

1.7 Continued Relevance of Heme Detoxification As a Primary Drug Target

Whilst resistance to drugs like CQ which target the heme detoxification pathways of the food vacuole is an ever increasing concern, the attractiveness of this target cannot be ignored. The reasons for continued interest are:

- Inhibition of hemozoin formation has been the mode of action of many drugs and consequently there is a lot of knowledge about this target.⁵³
- *P. falciparum* has high hemozoin (FP) toxicity whilst its human host has none at all.⁵⁴
- Being an integral component in host haemoglobin, hemozoin groups are fixed chemical entities and are not likely to vary, making them a good counterpoint as targets to malarial proteins or gene loci which are prone to mutation.⁵⁵

The process of heme detoxification is an integral process in the life of the malaria parasite and one which will always be necessary for its survival. As such, this is a drug target which will always be a viable mode of malarial suppression. It is also important to note that CQ's efficacy at destabilizing heme detoxification mechanisms has not lessened over time but instead the malaria parasite has developed the ability to remove the drug molecules from the food vacuole before they can interfere with cellular processes effectively.⁵⁶ This is recognisable in the way that CQ analogues exhibit anti-malarial action on CQ-resistant strains.⁵⁷

1.7.1 β -Hemozoin and the Theories around its formation

The synthetic analogue of hemozoin, β -hemozoin, has been shown to be identical to its biological counterpart.^{58,59} β -Hemozoin is formed by the polymerization of soluble hemozoin into an insoluble and chemically inert crystalline dimer. The formation of the dimer starts when two hemozoin molecules come into close association with each other and the porphyrin rings arrange

themselves such that a carboxylic acid tail on each monomer is aligned with the iron centre of its counterpart. Bonds from the propionate oxygens to the iron atoms then form and the water molecules coordinated to the metals on the opposite ring faces simultaneously displace, forming the dimer. This dimer, when in the presence of others, then extends to form larger macro-crystals. Originally this mechanism was considered to be catalyzed by lipids or proteins; however, research by Egan *et al* has shown that these dimers rapidly self-assemble under physiologically realistic conditions when at a lipid/water interface.⁶⁰ By virtue of β -hematin being analogous with its *in vivo* counterpart, hemozoin; coupled with its ability to self-assemble *in vitro*, it is an incredibly useful component in the screening of potential inhibitors of heme detoxification. If a molecule has the ability to prevent hematin polymerizing into β -hematin when in a physiologically equivalent environment, then it may very be capable of inhibiting the formation of hemozoin *in vivo*.

1.7.2 Strategies to Find Inhibitors of β -hematin Formation

1.7.2.1 UV/Visible Spectra

With the aim of designing a high-throughput assay for the detection of potential inhibitors of heme detoxification, Egan *et al* found that the early method of heme quantification, the pyridine hemochrome method, can be used for an effective monitoring of relative β -hematin and hematin levels.⁶¹ When pyridine is added to a solution of hematin, two pyridine molecules will coordinate themselves on either side of the iron porphyrin centre by displacing coordinated waters; this is a result of pyridine being a harder Lewis base than water. This results in a sharpening and intensification of the Soret band at 404 nm and an intensification of the Q band at 527 nm in the UV/Vis spectrum. In order for a similar coordination system to be produced with β -hematin, the environment must be made highly basic and the pyridine concentration kept high. β -Hematin is unstable at higher pH levels and the pyridine, in high concentration, is then capable of disrupting

the dimer to form the coordinated system. Thus, if the pyridine levels are kept lower, e.g. 10% by volume, and the pH maintained as neutral or mildly basic then no reaction occurs and there will be a poorly defined UV/Vis spectrum. If a molecule is capable of disrupting heme detoxification then there will be an increased concentration of hematin present for pyridine to form a complex with. This will then result in an increase in intensity of the Q and Soret bands in the reaction mixture's spectra. This assay was termed by Egan *et al* as the "Phi- β Assay".

1.7.2.2 *Infra-red*

A clear distinction between the infra-red (IR) spectra of β -hematin and its monomer, hematin, can be achieved through the monitoring of two characteristic frequencies. Strong peaks at 1660 cm^{-1} and 1210 cm^{-1} are β -hematin specific and allow for clear differentiation from hematin. The former peak represents the C=O stretch present in the unidentate Fe (III) carboxylate linkage between the two monomers at the iron porphyrin centre.⁶² The latter represents the C-O stretch within the Fe-O-C from that same linkage.⁶³ As such, an inhibitor of β -hematin formation will prevent the emergence of these strong peaks as the iron-carboxylate linkage between the hematin monomers will be prevented from forming.

1.7.2.3 *X-Ray*

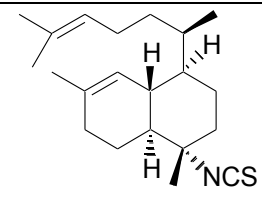
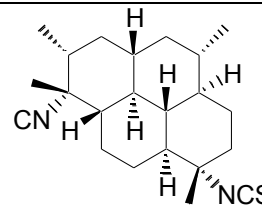
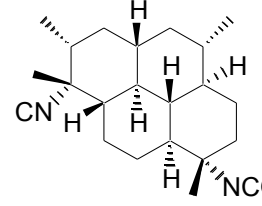
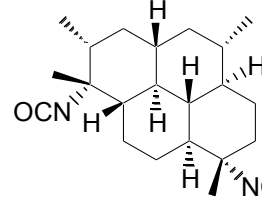
Although IR analysis shows the presence of this iron-carboxylate linkage, it does not guarantee that the crystal product has been formed. Subsequently, X-ray powder diffraction methods are required to confirm that β -hematin is in fact present. The diffraction pattern of hematin is characterized by broad peaks, indicating that the substance either comprises very small crystallites or is an amorphous solid. β -hematin on the other hand is crystalline in nature and will produce clearly defined peaks in the X-ray spectra.⁶¹ As such, the formation of β -hematin in a reaction mixture can be monitored through the development of clearly defined peaks that differ in

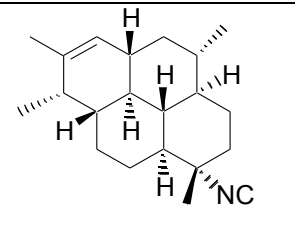
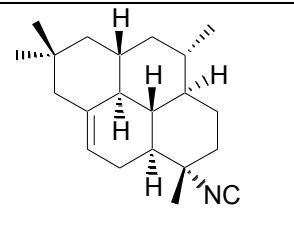
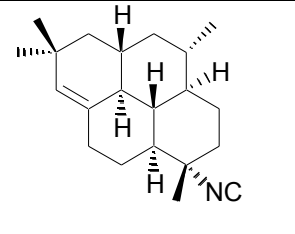
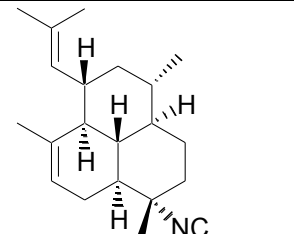
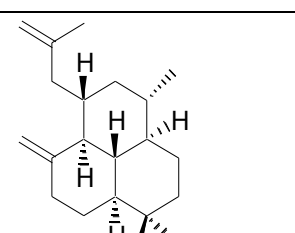
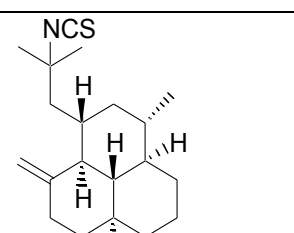
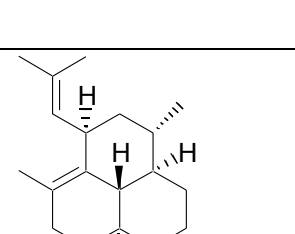
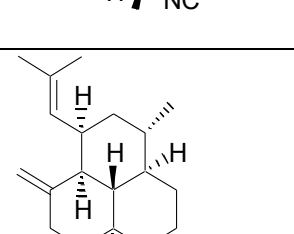
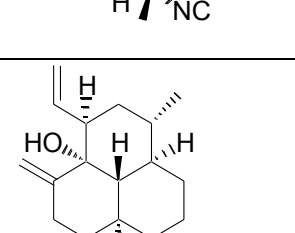
position (θ) to the broad peaks of the hematin starting material. An inhibitor of β -hematin formation will prevent the development of these peaks and the spectra will remain as that of monomeric hematin. An example of the X-ray powder diffraction method will be provided in Chapter 5.

1.8 Marine Anti-Malarial Isonitriles

A novel group of naturally occurring anti-malarials has been isolated from the marine sponge *Cymbastela hooperi* that possess characteristic isonitrile, isocyanate and isothiocyanate functionalities.⁶⁴ It has been shown that some of these compounds exhibit potent *in vitro* and *in vivo* anti-plasmodial activity effects at the nano-molar level (**Table 1.1**), possibly providing potential anti-malarial agents for future drug development.^{3,6,30,51}

Table 1.1: Structures of marine anti-malarial isonitriles, isocyanates and isothiocyanates used by Wright *et al* to generate their pseudoreceptor model and their IC_{50} values against *P. falciparum* strain D6.³⁰

No.	Structure	IC_{50} [nM]	No.	Structure	IC_{50} [nM]
1.30		>30160	1.31		126.48
1.32		219.96	1.33		9.4

1.34		210.09	1.35		285.39
1.36		249.09	1.37		1015.17
1.38		1747.98	1.39		1318.09
1.40		196.65	1.41		47.4
1.42		2306.47			

1.8.1 Previous Computational Methods to Predict Marine Isonitrile Inhibition of Hemozoin Formation

In research conducted by Wright *et al*³⁰, molecular modelling studies using three dimensional quantitative structure activity relationship (3D-QSAR) and receptor modelling methodologies were used to derive a pharmacophore hypothesis to fit the experimentally observed biological activities of structures **1.30** – **1.42**. As many drugs target the heme (FP) detoxification pathway, the interactions between these various compounds and a generated 3D pseudoreceptor envelope were simulated to provide information on pharmacophore structure and FP binding interactions were explored through force field molecular dynamics.

1.8.1.1 Pharmacophore Structure

To gain structural information about the pharmacophore it was assumed that all of the compounds interact with a common receptor and through comparable binding modes. An averaged receptor surface was generated by surrounding the inhibitor models with envelope-defining virtual particles possessing physiochemical descriptors, such as hydrophobicity, partial charge, electrostatic potential and hydrogen-bonding affinity. The various structures were chosen to give an accurate representation of this group of marine anti-malarials. This averaged surface was then used to generate the receptor model families characterising the pharmacophore. It was found that the optimal stereo-electronic fit is achieved by the isonitrile group of compounds and that activity decreases with an increase in shape and added electrostatically active functional groups. From the data produced, it was concluded that the most prominent structural determinant for receptor complementarity of the active compounds is the presence of an overall lipophilic, rigid molecular core comprising at least a tricyclic framework with an isonitrile group axially orientated.

1.8.1.2 Isonitrile Mode of Action

The structural knowledge gained from the pseudoreceptor model suggested that the receptor for these tricyclic isonitriles is hydrophobic in nature, but has the capacity to form electrostatic interactions with functional groups on the drug surface. Such interactions would describe activity against FP moieties and so three of the compounds were subject to modelling, mass spectrometry and optical activity studies in the presence of FP groups so as to monitor their behaviour. It was concluded that the isonitriles have the ability to form π - π chelation complexes with the iron center within FP, thereby replacing the hydroxyl moiety which is liganded to FP in the heme complex. The binding of the iron centre would also prevent the formation of the peroxidase-like ferryl Fe (IV) intermediate complex, thereby hindering H_2O_2 removal processes. This disruption of the parasitic detoxification pathways proposes that isonitrile compounds act against malaria in a similar fashion to chloroquine.

1.8.1.3 Critical Evaluation of Computational Methods Used

Criticism of the computational methods used by Wright *et al*³⁰ takes four forms. Firstly, the assumptions of the pseudopotential model are that the experimentally obtained IC_{50} values are solely dependent on the inhibitors interacting with one specific receptor and that this receptor is the FP moiety. The latter assumption is not necessarily true, however, and the target described by the pseudopotential envelope may in fact be another macromolecule in the complex passage from cell entry to arrival at the FP target, e.g. a transporter protein. The magnitude of the experimental IC_{50} value is actually dependent on a combination of the efficacy of drug delivery to the site of inhibitory action as well as the efficacy of the drug to perform this action *in situ*. Thus, the derived pharmacophore model may, for example, be describing a macromolecule responsible for delivering the compound to the site of inhibitory action but may not be the FP target itself. This means that the molecule with the lowest IC_{50} value may not be the most effective at binding to FP

but is instead able to reach its target more easily. Secondly, in this study the role of the isonitrile group in exerting an inhibitory effect is not discussed, nor is the nature of the $\pi - \pi$ chelation interactions elaborated on. Thirdly, the molecular modelling data only shows the starting configurations for the dynamical runs and does not show the final system arrangements. This leads to the final criticism that the configurations presented by Wright *et al*, with the isonitrile groups aligned in an axial orientation to, and in close association, with the iron centre, suggest that the isonitrile functionality either exhibits favourable electrostatic interactions with the centre of the FP porphyrin ring, or that there is the potential for formal intermolecular bonding to occur between these two groups. However, there is no discussion over the existence of such electrostatic interactions and the dynamical method which Wright *et al* used to reach this conclusion, being an empirical force field method, is not suitable to describe bond forming/breaking events as only *ab initio* methodologies are capable of this.^{65,66} As this pseudoreceptor model has the potential to provide valuable information on a potential novel anti-malarial pharmacophore, a greater understanding of its predictive capabilities is needed, with a particular focus being on the target which the pseudoreceptor is describing, i.e. is it modelling the active site of a heme target or another protein target?

As a result, the following questions needed to be answered:

1. What computational methodologies are capable of accurately predicting inhibition of β -hematin formation by marine isonitriles?
2. What is the nature of the interactions between these molecules and FP/hemozoin targets?
3. Does the pseudoreceptor model of Wright *et al* adequately describe these interactions and can the model be used for the rational design of a novel anti-malarial pharmacophore?

1.8 Aims

The aims of this thesis are therefore:

1. To describe the electronic properties of a representative set of marine anti-malarial compounds and their heme targets through the use of modern computational methodologies; and to make predictions on future intermolecular interactions based on this information. This will involve:
 - a. Construction of electronic models using density functional theory methods.
 - b. The expression of these models' electrostatic properties as molecular topologies.
 - c. Generation of highest occupied and lowest unoccupied molecular orbital population maps for each model.
 - d. Examining inhibitor-target electrostatic and orbital complementarities.

2. To validate the use of, and then apply a statistical docking program to explore the conformational space around the heme target models and to explore inhibitor-target electrostatic interactions. This will involve:
 - a. The selection a docking algorithm whose efficacy has been established through a rigorous case study.
 - b. Modification of the algorithm if necessary.
 - c. Application of the algorithm to the inhibitor-target systems.

-
3. To investigate whether formal bonding can occur between the functionalities of the isolated marine compounds and their heme targets; and whether the pseudoreceptor model of Wright *et al* accurately describes the proposed heme-binding nature of these compounds. This will require:
 - a. Construction of artificially bonded inhibitor-receptor complexes.
 - b. Energy minimizations of these complexes using semi-empirical *ab initio* methods to see if formally bonded inhibitor-heme complexes are energetically favourable.
 - c. Validation of an *ab initio* molecular dynamics method.
 - d. Application of this method to further confirm the nature of intermolecular bonding.
 - e. An evaluation of whether Wright *et al*'s pseudoreceptor model describes a heme target or another form of receptor molecule, taking into account data from all the computational methods described previously.
 - f. A further evaluation of the ability of Wright *et al*'s pseudoreceptor model to identify a novel anti-malarial isonitrile-containing pharmacophore.

 4. To rationally design a marine anti-malarial isonitrile analogue and to determine its inhibitory capabilities. This will involve:
 - a. A review of synthetic isonitriles and the identification of a novel marine anti-malarial isonitrile analogue.
 - b. Design and synthesis of the analogue.
 - c. Application of the theoretical techniques described above to predict its inhibitory potential.
 - d. Ascertain the synthetic analogue's inhibitory potential with respect to a standard inhibitor, i.e. chloroquine, using the β -hematin inhibition assay developed by Egan *et al*.

EVALUATION OF STEREOELECTRONIC PROPERTIES OF MARINE ANTI-MALARIALS AND THEIR HEME TARGETS

2.1 Modern Computational Methods for Electronic Structure Calculations

Nearly all of a material's physical properties can be related to free energy values. In turn, any property that is related to energies (or differences in energies) can be determined theoretically if a method exists which is both reliable and capable of accurately determining these values.⁶⁷

2.1.1 Molecular Mechanics / Dynamics

Two theoretical approaches commonly used for the handling of very large systems are the molecular mechanics (MM) and molecular dynamics (MD) methods.⁶⁷ Both use classical Newtonian motion equations to monitor the trajectory of a system's components under certain boundary conditions. The chief difference is that MD methods conduct these energy evaluations at a finite temperature whilst the MM methods do not.⁶⁶ The accuracy of these calculations is determined by the manner in which the inter-atomic forces are defined. In most cases, these forces are determined by means of an empirical model or force field, allowing for both the equilibrium thermodynamic and dynamical properties of a system to be calculated.⁶⁵ The general mathematical form of this force field is:

$$\begin{aligned}
 V(r^N) = & \sum_{bonds} \frac{1}{2} k_b (l - l_0)^2 \\
 & + \sum_{angles} k_a (\theta - \theta_0)^2 \\
 & + \sum_{torsions} \frac{1}{2} V_n [1 + \cos(n\omega - \gamma)] \\
 & + \sum_{j=1}^{N-1} \sum_{i=j+1}^N \left\{ \epsilon_{i,j} \left[\left(\frac{\sigma_{ij}}{r_{ij}} \right)^{12} - 2 \left(\frac{\sigma_{ij}}{r_{ij}} \right)^6 + \frac{q_i q_j}{4\pi\epsilon_0 r_{ij}} \right] \right\}
 \end{aligned}$$

...Equation 1.

Here the first three terms are the energy contributions of deviations from reference bond lengths, bond angles and torsional positions. The final term is the non-bonded energy contribution between all atom pairs, divided into a van der Waals term (first summation) and an electrostatic term (second summation). The reference values come from the accurate determinations of libraries of reference structures, selected to represent a broad spectrum of potential molecules. As a result, empirical methods are only effective if the structure being analyzed has adequate representation in the structural database of the force-field being used.⁶⁸

2.1.2 *Ab Initio* Methods

A failing of the force field methodologies is their inability to take electronic polarization effects into account and can only deal with chemical reactivity through specialized techniques.⁶⁶ With the advent of high speed parallel computing, the modern theoretical methodologies required to explore atomic interactions to high degrees of accuracy are made available for routine use.

Ab initio methods are fast becoming the method of choice for exploring chemical reactivity. The ability of these methods to simulate bond breaking and forming events allows for valuable information to be gathered on the interactions taking place. They can also help to facilitate the elucidation of the reaction mechanisms involved. Basic *ab initio* calculations are based on the assumptions that a system is comprised of a finite number of nuclei and electrons, that the Born-Oppenheimer approximation (BOA) is applicable to the system, and that the nuclei can be treated in their ground state electronic configuration. In essence, the BOA (or “clamped nuclei” hypothesis) treats the nuclei of a system as being stationary due to their relatively low speed compared to the electrons; thereby allowing for the Schrödinger equation to be solved for the wavefunction of the electrons alone.⁶⁸ However, the electron energy is dependent on the nuclear positions as the electrons will adiabatically follow the nuclei. Thus, the total energy of the system is expressed as a sum of electron and nuclear energies where the nuclear energy term is given an approximated value.^{66, 69} The total Hamiltonian is:

$$H = T_e + V_{ee} + V_{eN} + T_N + V_{NN} \quad \dots\text{Equation 2.}$$

Here the terms are the electronic kinetic energy, the inter-electron Coulomb repulsion, the electron-nuclear Coulomb attraction, the nuclear kinetic energy and the inter-nuclear Coulomb repulsion. This can now be simplified to:

$$H = H_{\text{elec}} + T_N + V_{NN} \quad \dots\text{Equation 3.}$$

Here H_{elec} is the simplified Hamiltonian eigenvector equation for the electrons only and $T_N + V_{NN}$ are the nuclear energies which are given an approximated value. The multi-electron Schrödinger wave function in this modified Hamiltonian can now be replaced by a product of one-electron wave functions which can be solved individually and then compounded.⁶⁹ There are several methods available for computing these electronic structure functions. Initially the most popular method was the Hartee-Fock (HF) method which incorporated both the Hartee-Fock and the Linear Combination of Atomic Orbitals (LCAO) approximations and applied them to the electronic Schrödinger equation.⁶⁸ HF approximations treat the motions of the electrons as independent of one another and as a result there arises a discrepancy as the electrons will now come into "contact" with one another more than in the case of a „real-life' multi-electron system. This will cause an overestimation of the inter-electronic repulsion energy term, thus resulting in an overly high total energy. To correct this, an electron correlation term is introduced to account for the coupling of electronic motions, thereby lessening the inter-electronic repulsion energy and lowering the total energy.^{68,69} There are various methods which account for this correlation energy term, with the most popular being the second order Møller-Plesset (MP2) energy correlation function, however this method is very time consuming with computational time scaling proportional to N^6 where N is the number of atoms in the system.⁷⁰ The long computational times of HF methods has resulted in them often being abandoned in favour of more expedient methods.

2.1.3 DFT Methods

In modern *ab initio* calculations, the Kohn-Sham (KS) formulation of density functional theory (DFT) has become the method of choice, in which the atomic forces acting on a system are expressed as a functional (a function of a function) of the electron density. The total energy of the system is expressed as a functional of multiple mutually orthonormal single-particle orbitals which are dependent upon the electronic density of the system.^{66, 68, 69} The two most popular functionals in modern DFT are the Becke-Lang-Yee-Parr (B3LYP)^{71, 72} and Perdew-Burke-Ernzerhof (PBE)⁷³ gradient correcting functional where the PBE is a pure DFT method; whilst the B3LYP is a HF/DFT hybrid. Currently, the literature standard DFT formulation uses the B3LYP functional applied to the 6-31G (d) basis set which describes the core electronic states by means of six Gaussian functions and then describes the valence states with two vector sets containing three and one vectors, respectively. Consequently, this formulation was used for all the minimizations in this chapter.

2.2 Construction of Chloroquine and Marine Isonitrile, Isocyanate and Isothiocyanate Electronic Models

In order to investigate the predictive capabilities of Wright *et al*'s pseudoreceptor model, a detailed knowledge of their electronic structure was essential for predicting future interactions with other molecules. Furthermore, computational algorithms such as electrostatic topology mapping, statistical ligand docking⁷⁴ and dynamical analyses⁷⁵ often require data obtained from electronic structure calculations. Thus the molecular electronic properties of a selection of computational models of Wright *et al*'s marine anti-malarial were determined using DFT methods that involved construction of molecular electron densities, full molecular orbital population analyses and the visualization of molecular bonding orbitals and electrostatic potentials as graphical topologies. Structures **1.30** – **1.42** provided a diverse group of marine compounds containing representatives of structures with isonitrile, isocyanate and isothiocyanate functionalities. The IC₅₀ values of inhibitory capabilities of these compounds against malaria have also been determined and so correlations between structure and anti-malarial function could hopefully be explored. It was hoped that this data, coupled with the

statistical ligand binding studies performed in Chapter Three and the *ab initio* simulations performed in Chapter Four, would allow for Wright *et al*'s pseudoreceptor model to be adequately evaluated. A theoretical model of chloroquine was also constructed to act as the control as it is a known inhibitor of heme polymerization and has been the frontline anti-malarial for several decades.

2.3 Molecular Bonding Orbitals of Chloroquine and Marine Isonitriles, Isocyanates and Isothiocyanates

Once the molecular electronic density distributions had been calculated, the location and shape of the intermolecular bonding orbitals, the HOMO (highest occupied) and LUMO (lowest unoccupied) molecular orbitals, could be investigated. As intermolecular bonding occurs between these two orbitals on adjacent molecules, i.e. electrons are donated from one molecule's HOMO and accepted by another's LUMO, an understanding of their nature is critical for predicting where such bonds will form, if they form at all. To achieve this, the models were subject to full orbital population analyses and the HOMO and LUMO maps were visualized. Isocontour values are 0.02 e/bohr^3 and both the positive (blue) and negative (orange) orbital lobes are shown. Although interactions from lower but energetically similar molecular orbitals, i.e. HOMO - 1, LUMO + 1, etc., can play a part in determining reactivity, they have not been considered explicitly in the following preliminary analyses.

2.3.1 HOMO and LUMO Orbital Maps of Chloroquine

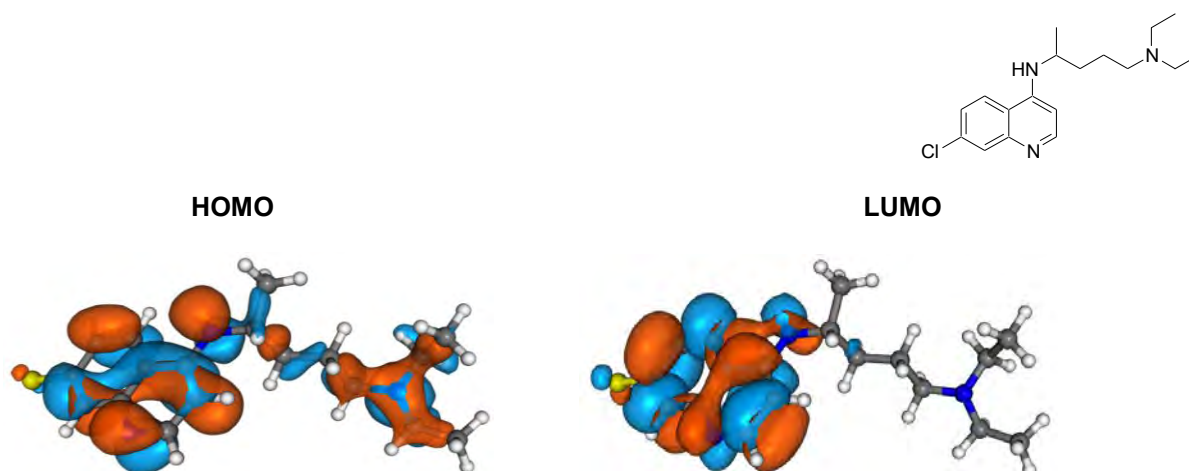


Figure 2.1: Electronic density maps of chloroquine HOMO and LUMO molecular orbitals.

Visual inspection of the above maps show that the orbitals of the aromatic rings contribute the most to the HOMO and LUMO molecular orbitals, with the amine group on the ring substituent contributing significantly to the HOMO but not the LUMO. Most intermolecular electronic interactions will therefore most likely be directed from/to the aromatic rings.

2.3.2 HOMO and LUMO Orbital Maps of Marine Compounds

From the full population analyses, occupation maps of the HOMO and LUMO orbitals were generated and visualized. The orientations of the molecules may differ slightly, this was done so as to better present the orbitals for visualization. Double, triple and aromatic bonds are not indicated explicitly but can be identified by the number of attached hydrogens:

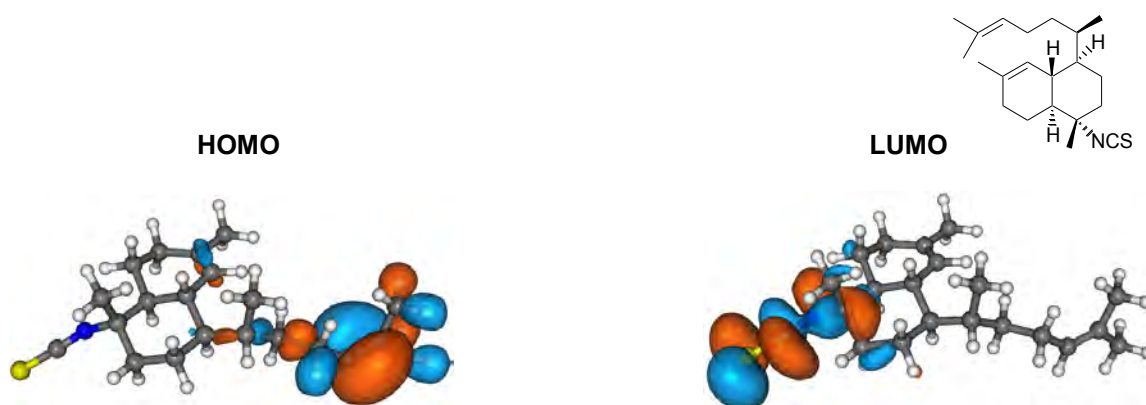


Figure 2.2: Electronic density maps of the HOMO and LUMO molecular orbitals for **1.30**.

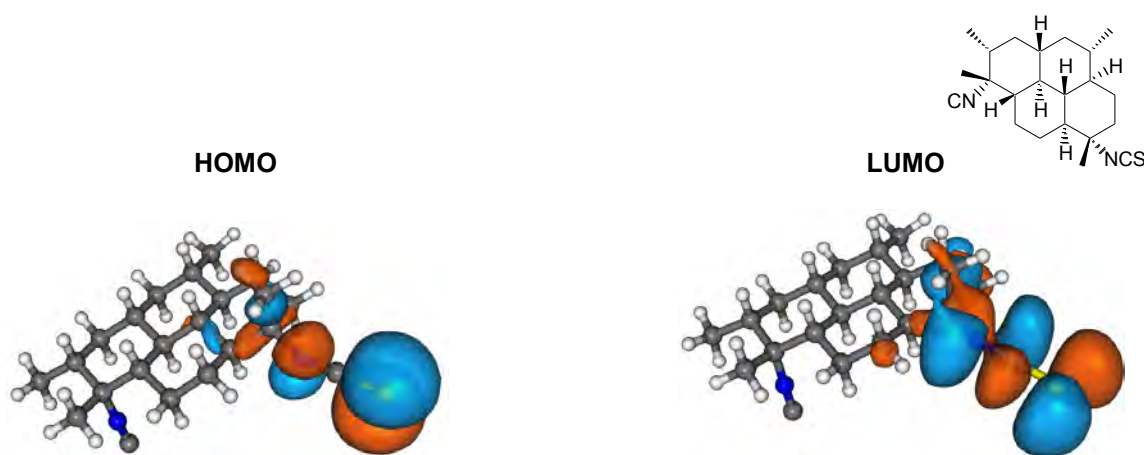


Figure 2.3: Electronic density maps of the HOMO and LUMO molecular orbitals for **1.31**.

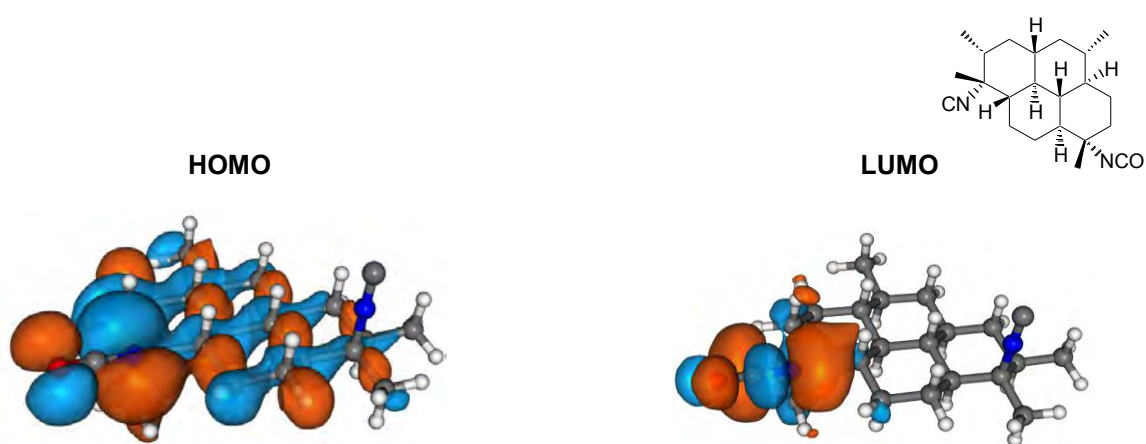


Figure 2.4: Electronic density maps of the HOMO and LUMO molecular orbitals for **1.32**.

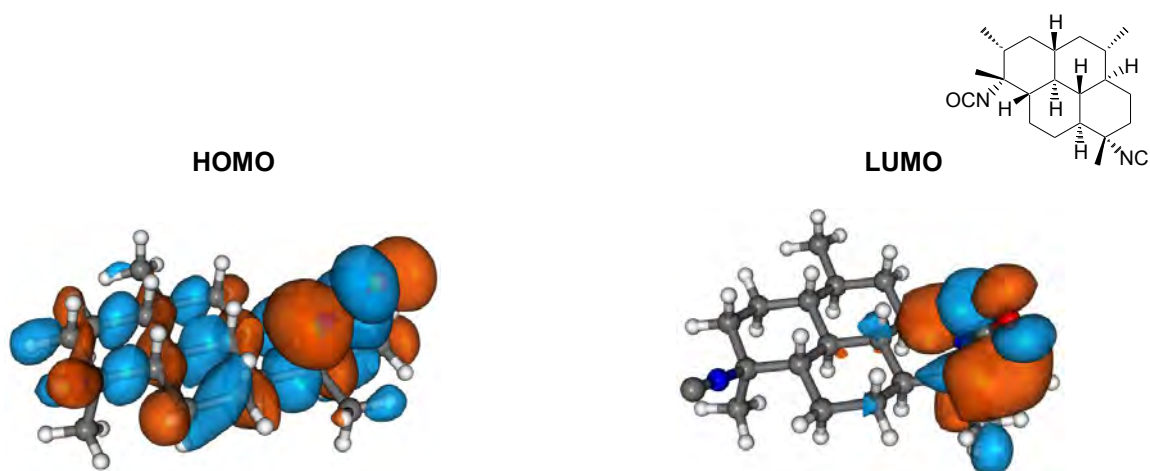


Figure 2.5: Electronic density maps of the HOMO and LUMO molecular orbitals for **1.33**.

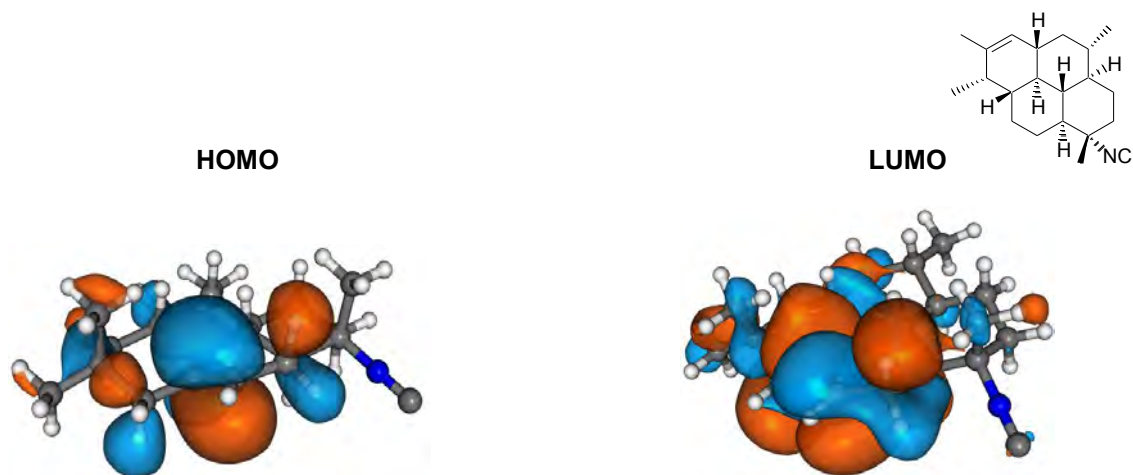


Figure 2.6: Electronic density maps of the HOMO and LUMO molecular orbitals for **1.34**.

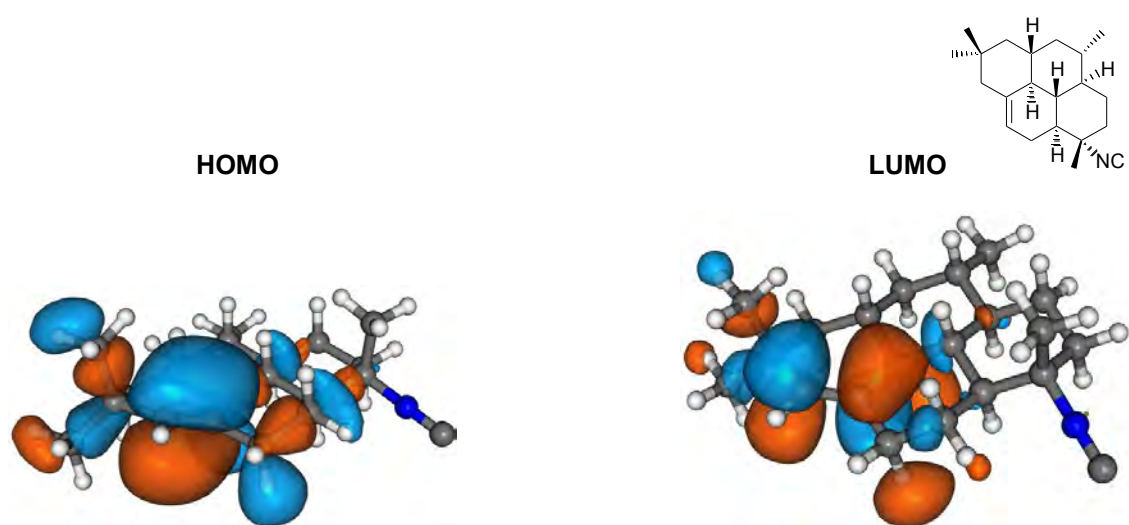


Figure 2.7: Electronic density maps of the HOMO and LUMO molecular orbitals for **1.35**.

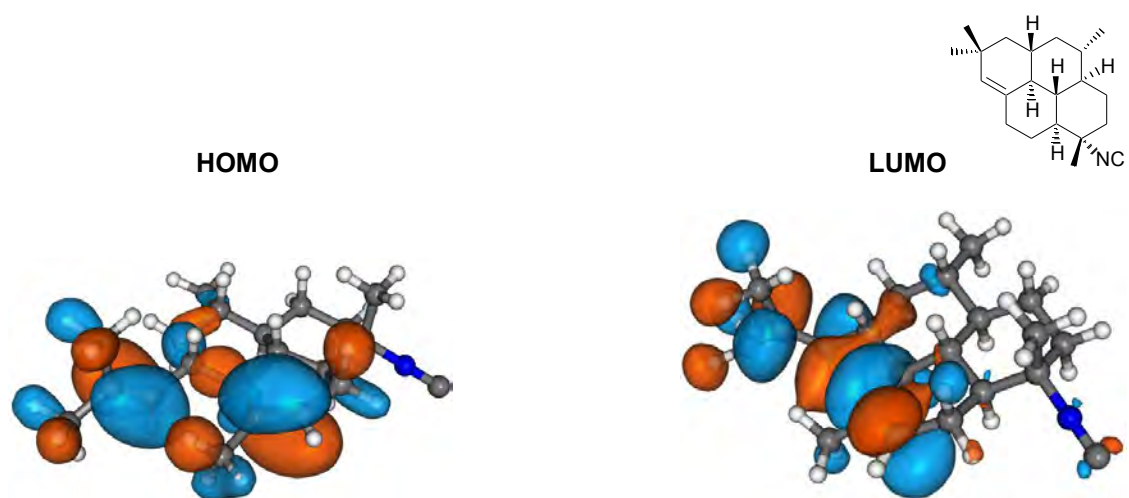


Figure 2.8: Electronic density maps of the HOMO and LUMO molecular orbitals for **1.36**.

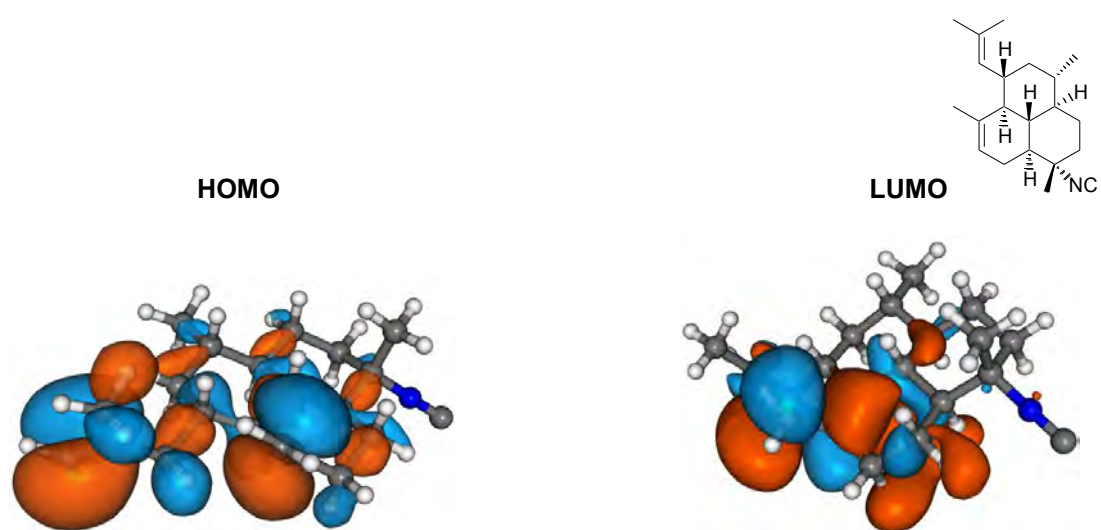


Figure 2.9: Electronic density maps of the HOMO and LUMO molecular orbitals for **1.37**.

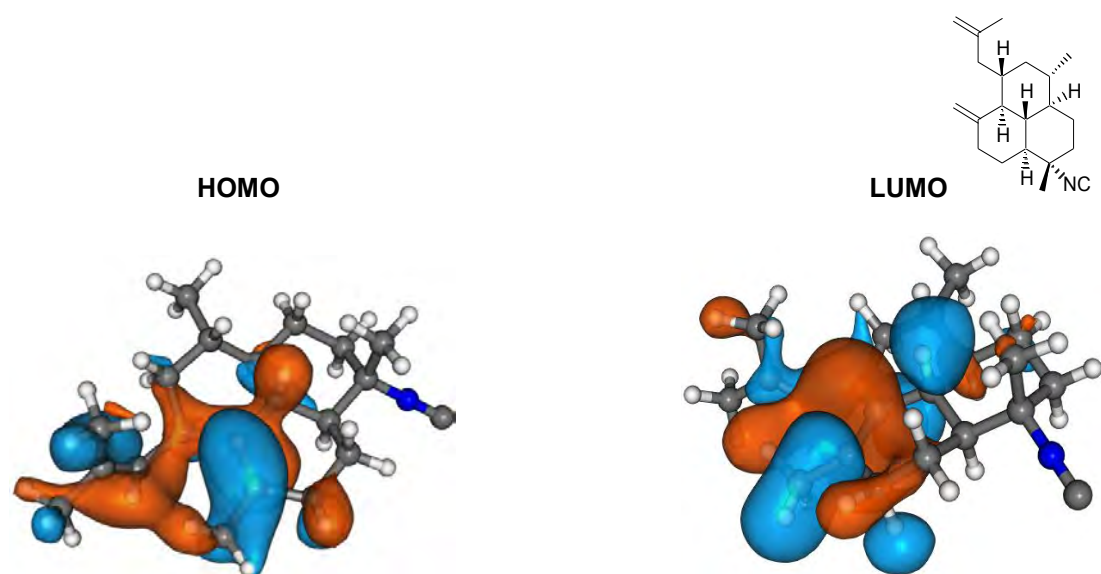


Figure 2.10: Electronic density maps of the HOMO and LUMO molecular orbitals for **1.38**.

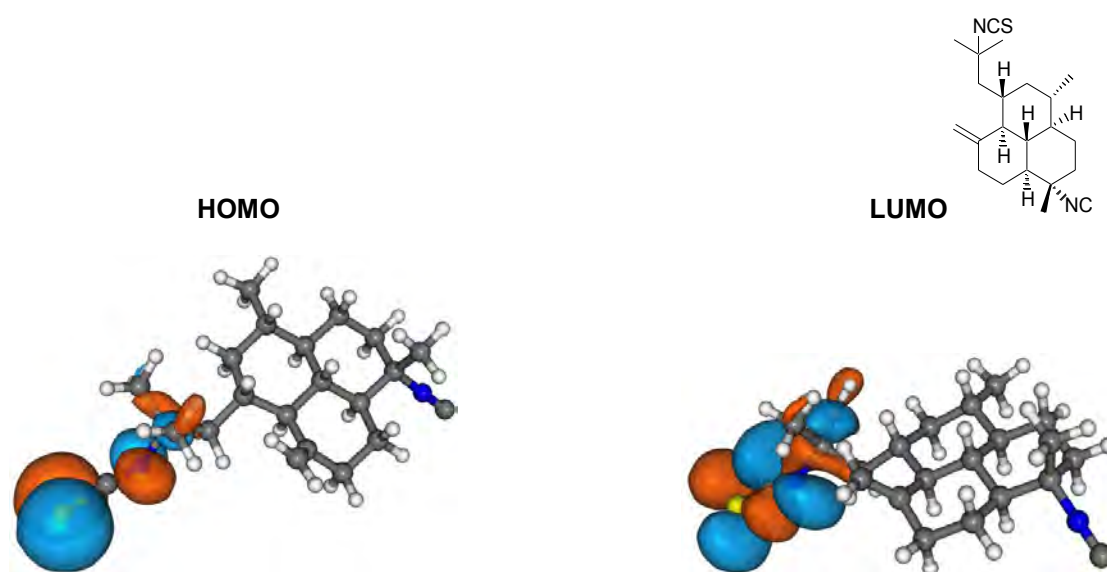


Figure 2.11: Electronic density maps of the HOMO and LUMO molecular orbitals for **1.39**.

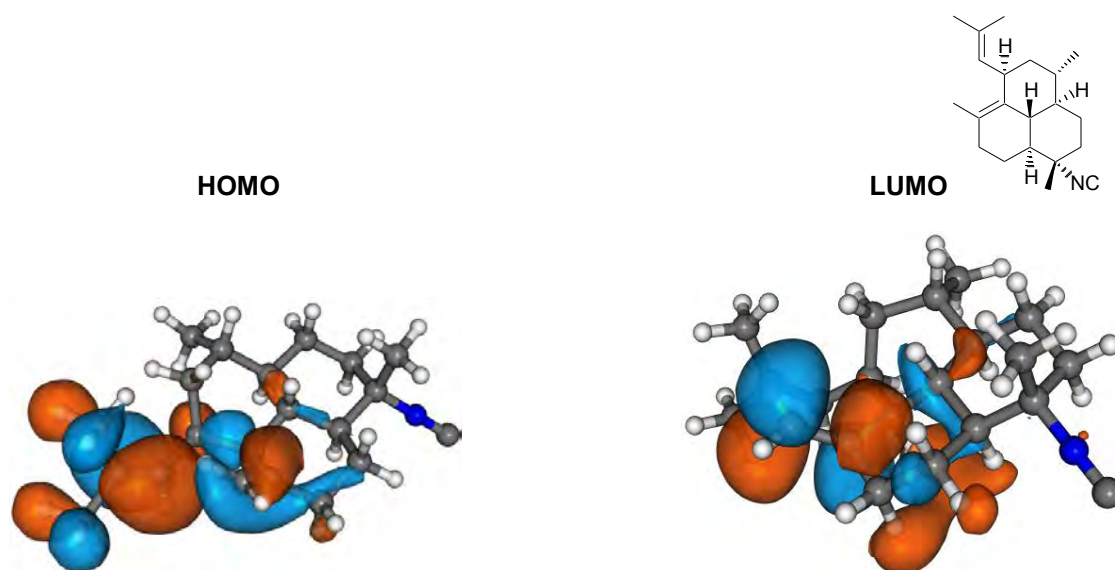


Figure 2.12: Electronic density maps of the HOMO and LUMO molecular orbitals for **1.40**.

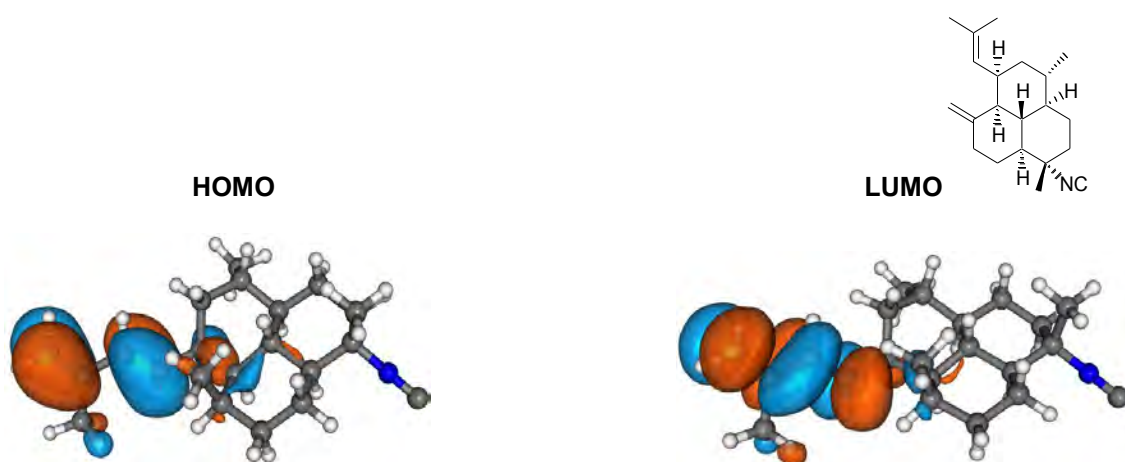


Figure 2.13: Electronic density maps of the HOMO and LUMO molecular orbitals for **1.41**.

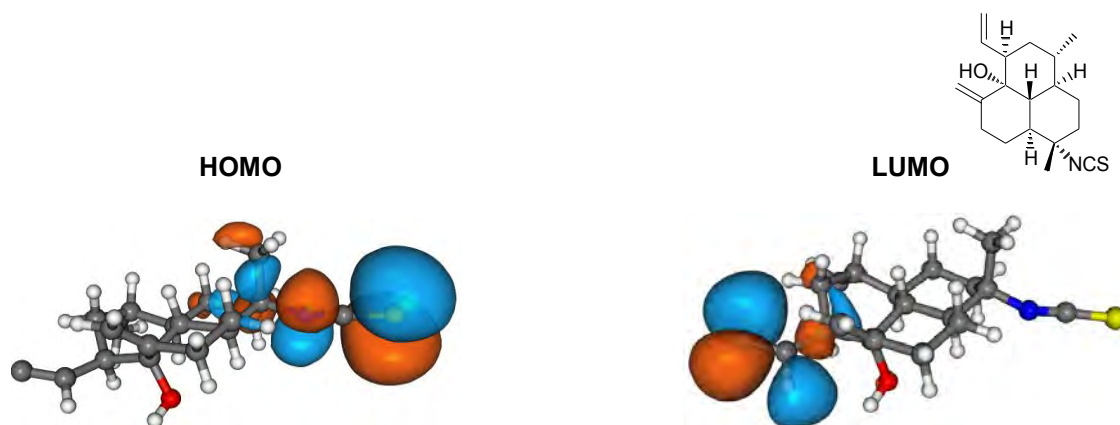


Figure 2.14: Electronic density maps of the HOMO and LUMO molecular orbitals for **1.42**.

One way of inhibiting the detoxification of heme would be for the molecules to form formal bonds with the heme molecules, thereby preventing their polymerization into inert hemozoin. To effect this, complementary overlap needs to occur between the HOMO/LUMO orbitals of the inhibitor and the receptor molecules. It can be seen that the local orbitals of the isocyanate (structures **1.32** and **1.33**) and isothiocyanate (structures **1.30**, **1.31**, **1.39** and **1.42**) functionalities can act as major components of both the HOMO and LUMO molecular orbitals. As intermolecular bonding occurs between these molecular orbitals, it indicates that these functionalities could potentially form formal bonds with other molecules as either an electron donor or acceptor. The isonitrile (structures **1.31** – **1.41**) orbitals however make little, if any, contribution to the HOMO and LUMO orbitals. The electron density either

sits on alternate functionalities, e.g. on the isocyanate or isothiocyanate as seen in structures **1.32** and **1.39** respectively; or on the carbon skeleton as exemplified in structure **1.38**. This suggests that the anti-malarial activities of the marine isonitriles may in fact not be due to their ability to form bonds with the heme receptor molecules.

2.4 Construction of Hematin and β -Hematin Dimer Electronic Models

In order to investigate the action of the inhibitor molecules mentioned above, it was critical to understand the electronic properties of the heme receptors that they interact with. As disruption of heme polymerization can occur either by the prevention of free heme groups from forming β -hematin dimers, or through the “capping” of these dimers to halt macro-crystal growth; electronic models of a free heme moiety (FP) and a β -hematin dimer (HD) were constructed.

2.4.1 Selection of the Free Heme Model's Electronic State

Arujo *et al* showed that theoretical free heme models can exist in four different electronic states: singlet, triplet, quintet and septet.⁷⁶ In order to ascertain which state to use, the heme model was minimized in the singlet, triplet and quintet states and the one possessing the lowest energy was used for subsequent analyses. A minimization of the septet was not performed as it was shown in this study to be much higher in energy than the other three states. The FP model was successfully minimized in both the singlet and triplet electronic states with electronic energies of -3098.486 Hartrees and -3098.549 Hartrees respectively. Once converted to kJ the triplet state is 166 kJ lower in energy than the singlet state. The quintet state repeatedly failed to achieve electronic self-consistency and it could only be successfully minimized using a pseudopotential to describe the iron atom's core electrons and then the standard DFT method to account for the valence electrons.⁷⁷ As pseudopotential models treat the non-valence electrons of a given atom as a rigid core, these methods are not as accurate as unrestricted DFT calculations which account for the motions of all atomic electrons. Consequently, the quintet state was not considered and the triplet heme electronic model was used for subsequent analyses.

2.5 Molecular Bonding Orbitals of Free Heme and β -Hematin Dimer Models

2.5.1 HOMO and LUMO Orbital Maps of Free Heme

From the full population analyses, occupation maps of the HOMO and LUMO orbitals were generated and visualized. Isocontour values of 0.01 e/bohr^3 were applied and both the positive (blue) and negative (orange) orbital lobes are shown. The orientations of the molecules may differ slightly, this was done so as to better present the orbitals for visualization. Double, triple and aromatic bonds are not indicated explicitly but can be identified by the number of attached hydrogens:

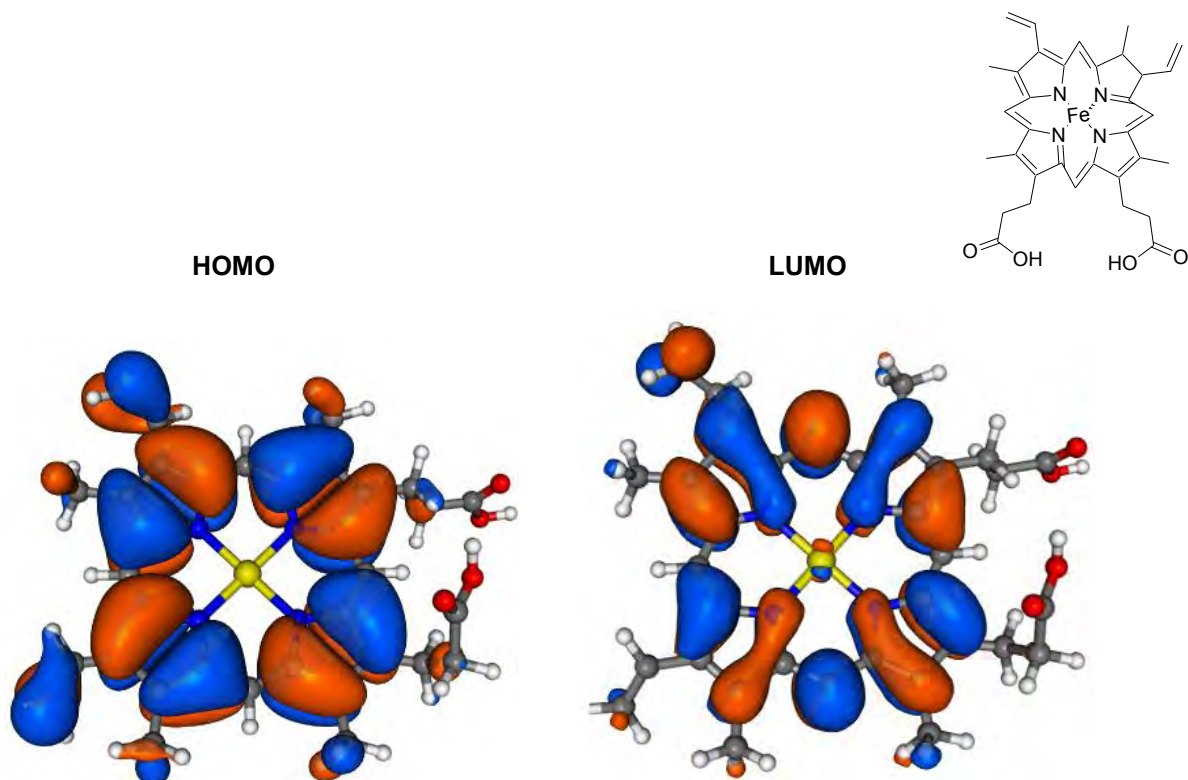


Figure 2.15: Electronic density maps of the HOMO and LUMO molecular orbitals for free heme.

It can be clearly seen that formal bonding from the HOMO orbital will most likely occur around the the porphyrin ring, with the largest orbital contribution being from the pirrolic nitrogens (the word pirrolic is widely used to describe the nitrogens coordinated to the iron atom in heme)⁷⁶ and their neighbouring carbons. The iron atom's orbitals are not involved in the molecular HOMO and so no electron

donation will occur from this position. The largest contribution to heme's LUMO once again comes from the orbitals of the pyrrolic nitrogens, though there is a small contribution to the molecular orbital from the iron centre. Consequently, the iron centre may play a role in bonding in an electron accepting capacity.

2.5.2 HOMO and LUMO Orbital Maps of the β -Hematin Dimer

From the full population analyses, occupation maps of the HOMO and LUMO orbitals were generated and visualized. Isocontour values of 0.01 e/bohr^3 were applied and both the positive (blue) and negative (orange) orbital lobes are shown. The orientations of the molecules may differ slightly, this was done so as to better present the orbitals for visualization. Double, triple and aromatic bonds are not indicated explicitly but can be identified by the number of attached hydrogens:

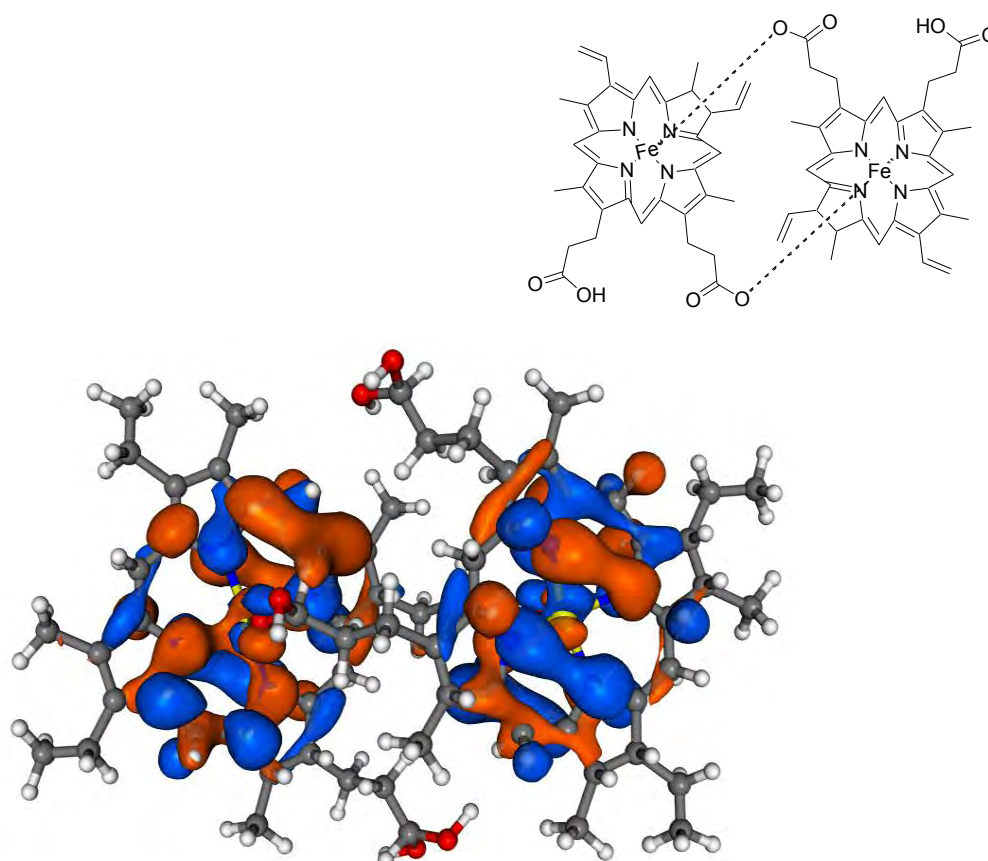


Figure 2.16: Electronic density maps of the HOMO molecular orbital for the β -hematin dimer as viewed from above the ring planes.

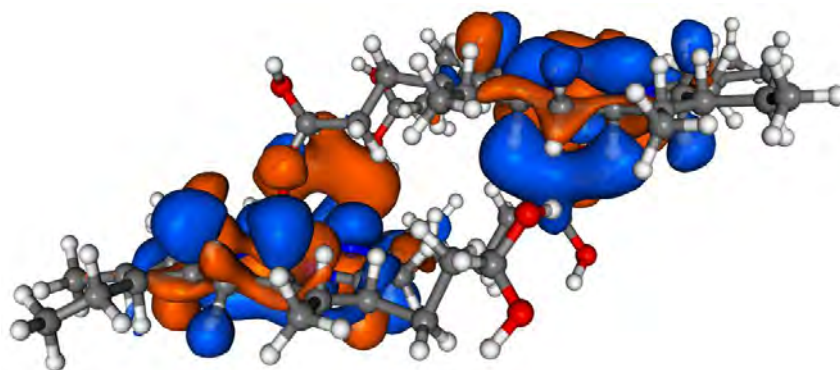


Figure 2.17: Electronic density maps of the HOMO and LUMO molecular orbitals for the β -hematin dimer as viewed from within the ring planes.

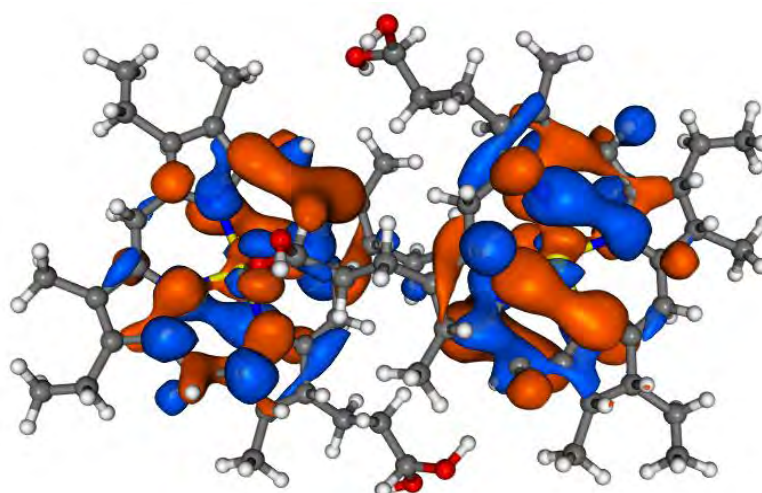


Figure 2.18: Electronic density maps of the LUMO for the β -Hematin dimer as viewed from above the ring planes.

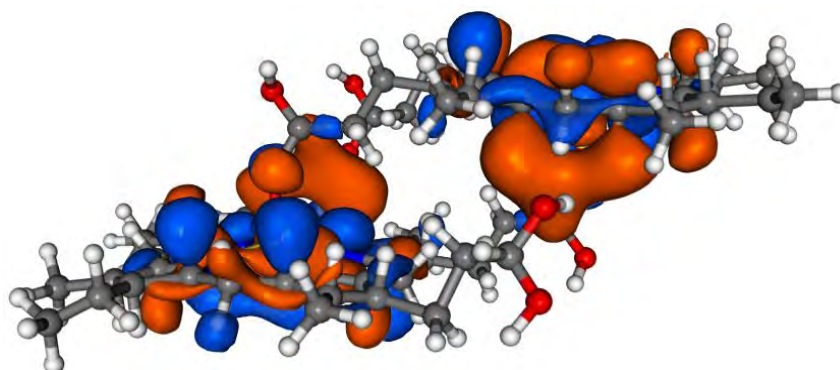


Figure 2.19: Electronic density maps of the LUMO orbital for the β -hematin dimer as viewed from above the ring planes.

The HD orbital maps are very similar to those of the FP, with most of the orbital contributions coming from the pyrrolic nitrogens and their adjacent carbons within the porphyrin rings. In the dimer, however, there is greater contribution from the iron centres to these orbitals when compared to the very small contributions from the FP iron orbitals. A result of this is that, whilst inter-molecular bonding will most probably be directed to the nitrogens and their surrounding carbons, if a molecule's orbitals are of the necessary shape and are complementary with regards orbital parity, they may be capable of forming a bond with the iron centres.

Our studies indicate that the inhibitor molecules with MO's that have potential to form such bonds are those with isocyanate and isothiocyanate groups. The orbitals of these groups possess the necessary shape and parity to be capable of overlapping with receptor nitrogen orbitals and extending this overlap to include the iron orbitals. The isonitrile groups of the marine compounds have been shown to make little contribution to the HOMO/LUMO orbitals and so would not be likely candidates for bonding. A feature of the best stereoelectronic fit for Wright *et al's* heme pseudoreceptor model, as stated in that work, was an isonitrile functionality; however the data obtained from the orbital population analyses show that these functionalities exhibit the lowest potential for intermolecular orbital overlap with the heme models. It must be remembered that formal intermolecular bonding is not the only mode of inhibitory behaviour and that electrostatic attractions between the inhibitor models and their heme targets could result in successful inhibition of heme detoxification mechanisms.

2.6 Molecular Electrostatic Topologies of Chloroquine and Marine Isonitriles, Isocyanates and Isothiocyanates

Another type of intermolecular interactions that can occur are electrostatic attractions or repulsions. These arise due to differences in charge distribution between two molecules' electron clouds. Whilst not as powerful as intermolecular bonds, these interactions can be sufficient for a molecule to exhibit an inhibitory action on another. In the case of heme polymerization, if the inhibitor molecules can successfully occupy the space around the heme receptors and block the approach of subsequent heme molecules, then the formation of β -hematin dimers or dimer macro-crystals will be compromised. This model is generally accepted as the mode of action of chloroquine.⁷⁸ These “bond-less” interactions come about through electrostatic attractions between the electron clouds of the two molecules and can be investigated through computing the electrostatic potentials of the molecular orbitals as a function of total electronic density. This creates molecular topologies for the interacting compounds and areas of electrostatic complementarity can be identified as regions for intermolecular interactions.

2.6.1 Electronic Topology of Chloroquine

Molecular electrostatic potential (MEP) surfaces were calculated from the population analysis files (Section 2.4) and superimposed on maps of total electronic density:

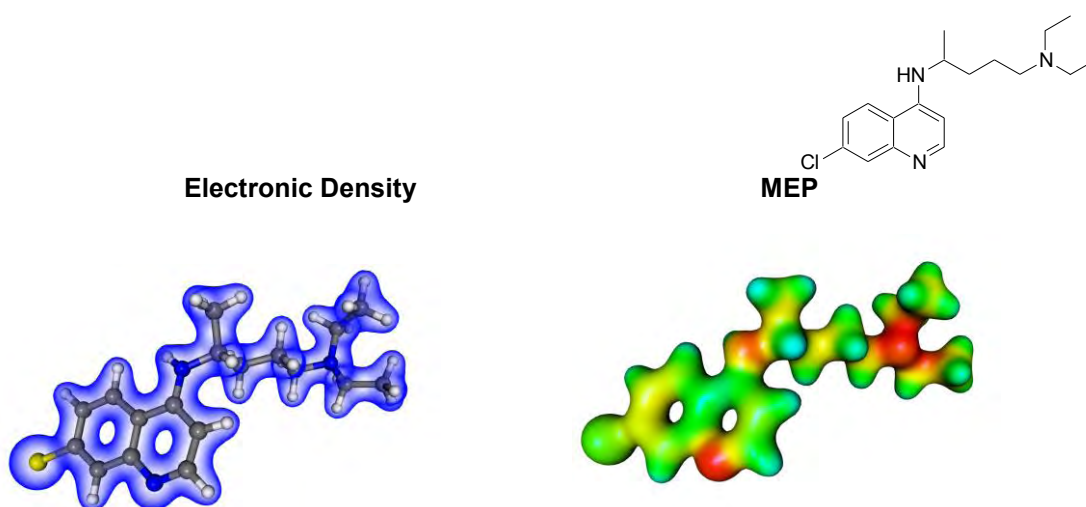


Figure 2.20: Molecular electrostatic potential (right) superimposed on a map of total electronic density (left) for chloroquine.

The electrostatic surface of the CQ molecule has some key features. The nitrogen atoms all bear significant negative potentials due to their lone electron pairs and these atomic centres will have the potential to donate these electrons. The chloride substituent, due to its high electronegativity, has a moderately positive electron potential and so will most likely direct itself to regions of negative potential on a receptor's complementary surface. The bicyclic ring system is predominantly electropositive, with regions of electronegativity on the nitrogen and the carbons adjacent to the halide bearing carbon. The hydrogens on the ring system appear as nodes of high electropositivity and appear blue on the MEP. Thus, the ring system will most likely orientate itself in a planar fashion with a receptor should it possess a predominantly negative electrostatic surface, with the aromatic nitrogen directing towards more positive receptor regions. Finally, the long carbon side-chain has varied regions of potential, ranging from high positive potentials on the hydrogen centres, to high negatives on the nitrogens. This side-chain will thus exhibit complex interactions with receptor surface topologies.

2.6.2 Electronic Topologies of Marine Compounds

Molecular electrostatic potential (MEP) surfaces were calculated from the population analysis files and superimposed on maps of total electronic density:

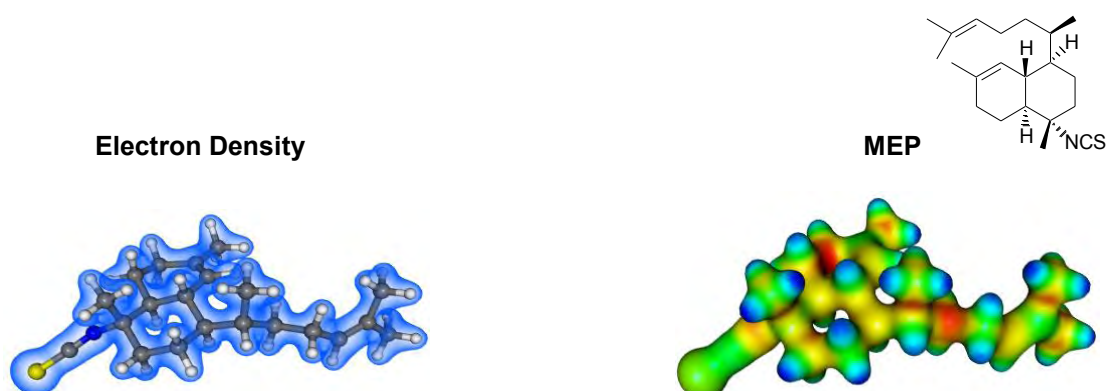


Figure 2.21: MEP (right) superimposed on a map of total electronic density (left) for **1.30**.

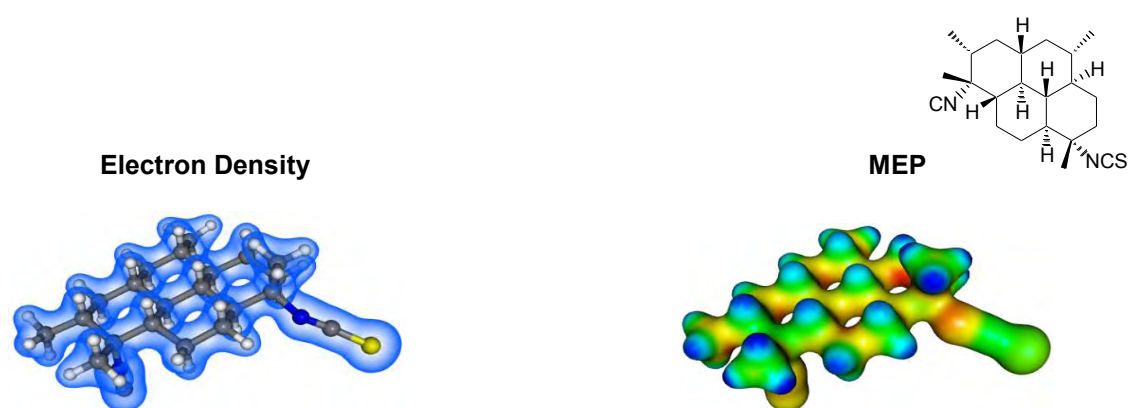


Figure 2.22: MEP (right) superimposed on a map of total electronic density (left) for **1.31**.

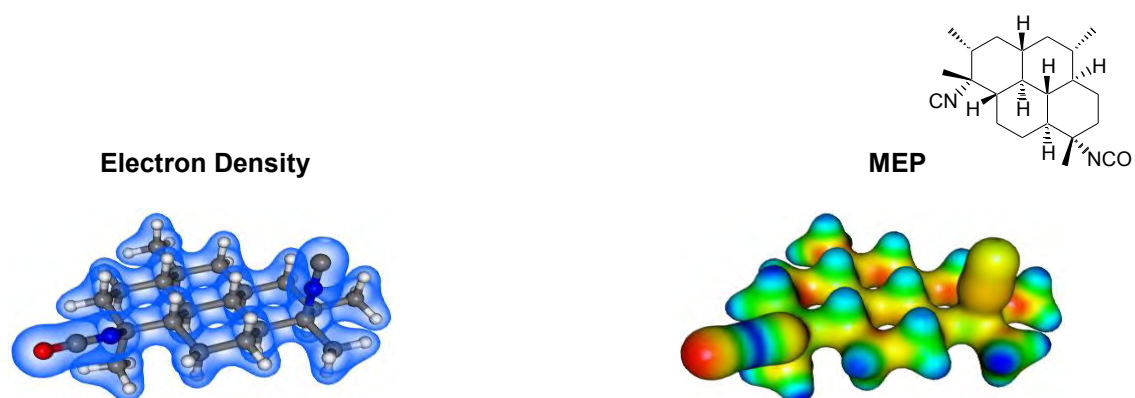


Figure 2.23: MEP (right) superimposed on a map of total electronic density (left) for **1.32**.

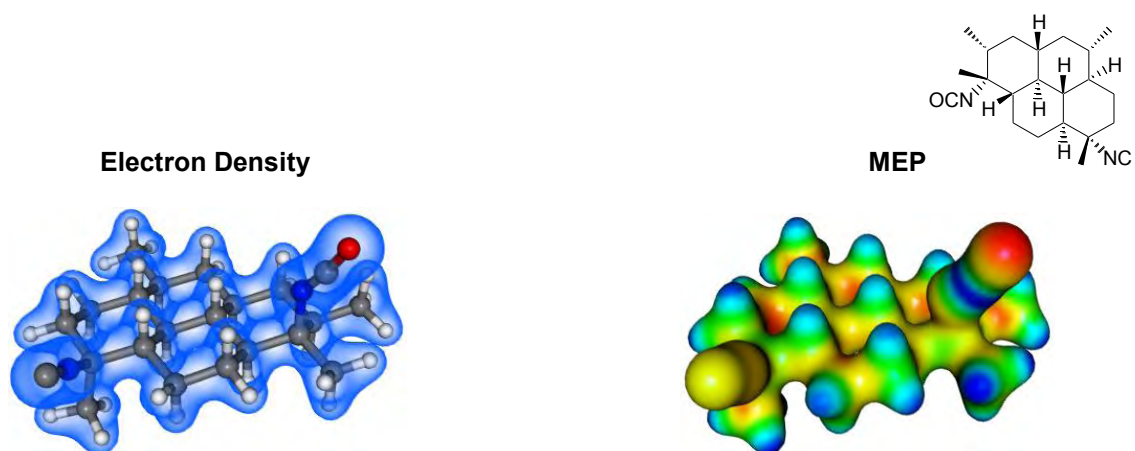


Figure 2.24: MEP (right) superimposed on a map of total electronic density (left) for **1.33**.

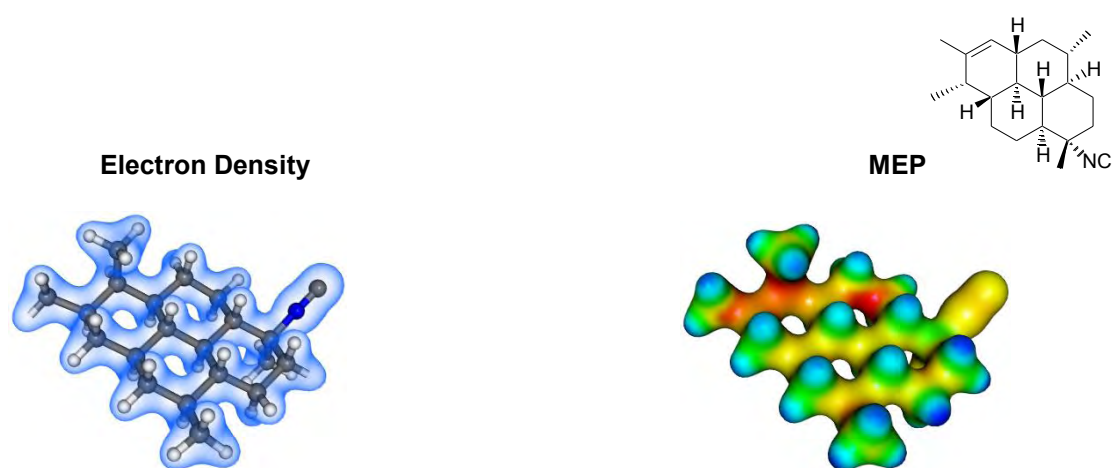


Figure 2.25: MEP (right) superimposed on a map of total electronic density (left) for **1.34**.

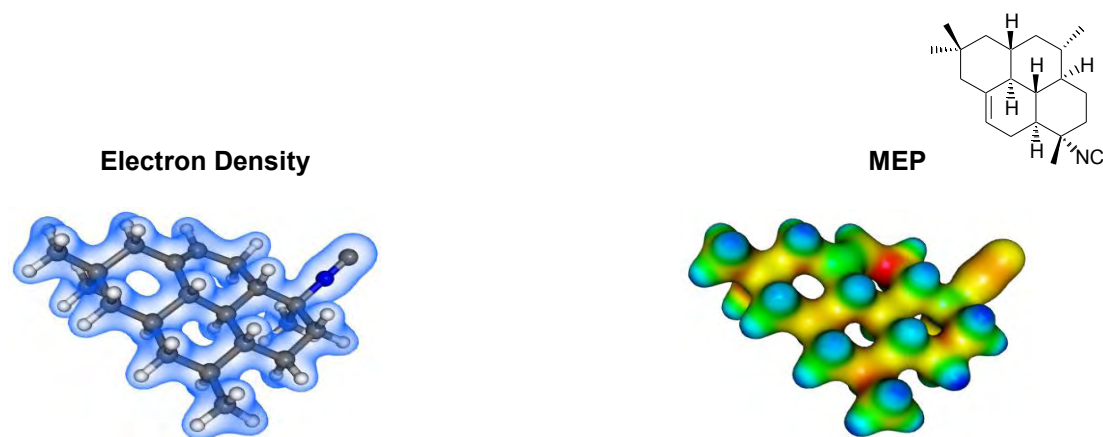


Figure 2.26: MEP (right) superimposed on a map of total electronic density (left) for **1.35**.

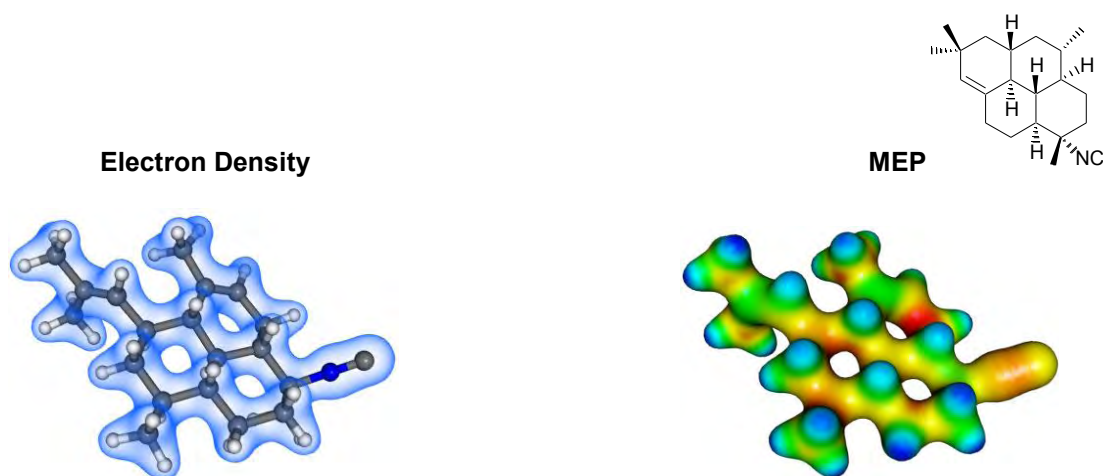


Figure 2.27: MEP (right) superimposed on a map of total electronic density (left) for **1.36**.

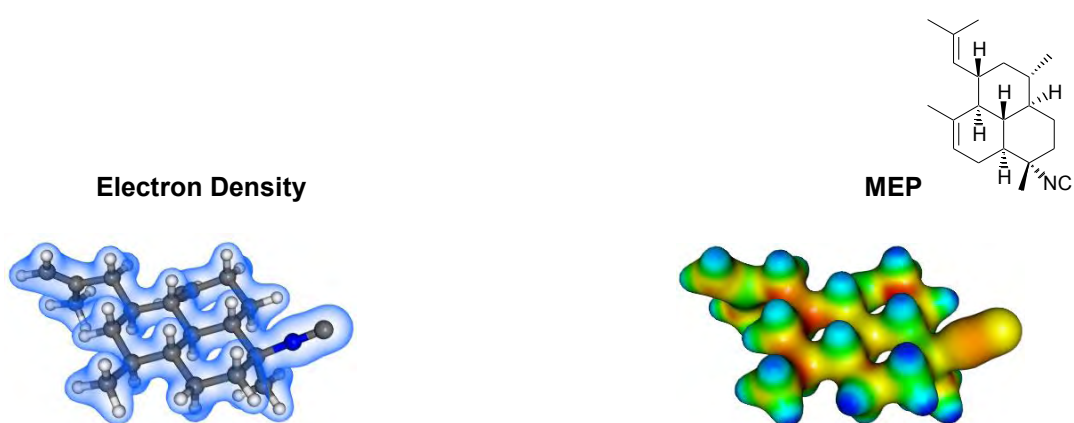


Figure 2.28: MEP (right) superimposed on a map of total electronic density (left) for **1.37**.

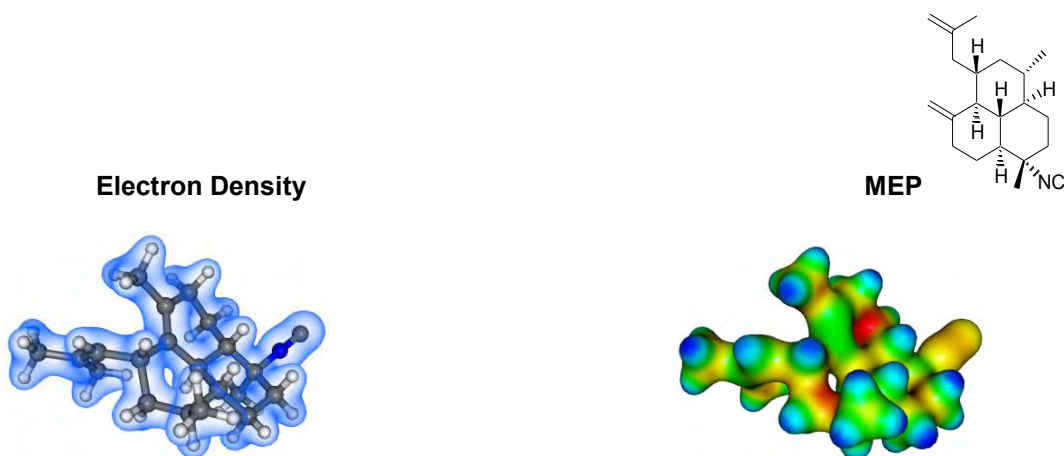


Figure 2.29: MEP (right) superimposed on a map of total electronic density (left) for **1.38**.

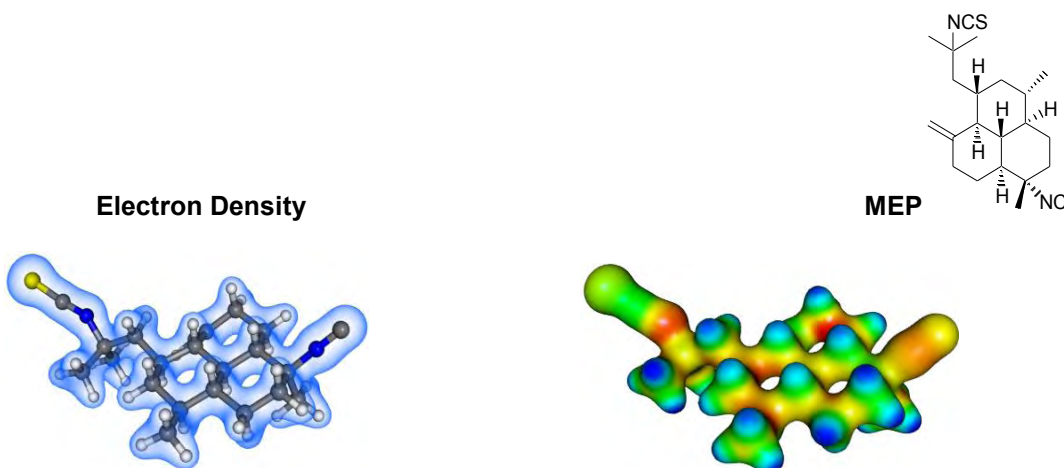


Figure 2.30: MEP (right) superimposed on a map of total electronic density (left) for **1.39**.

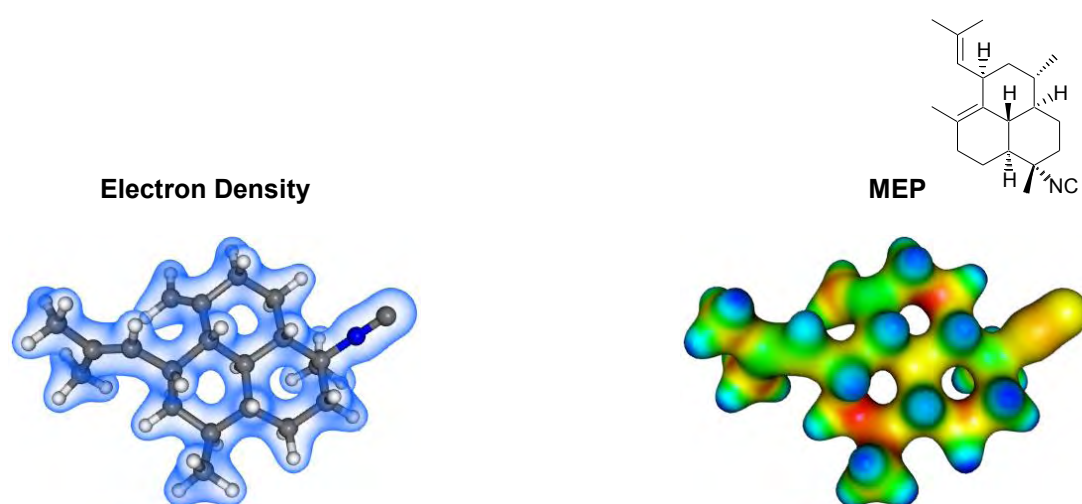


Figure 2.31: MEP (right) superimposed on a map of total electronic density (left) for **1.40**.

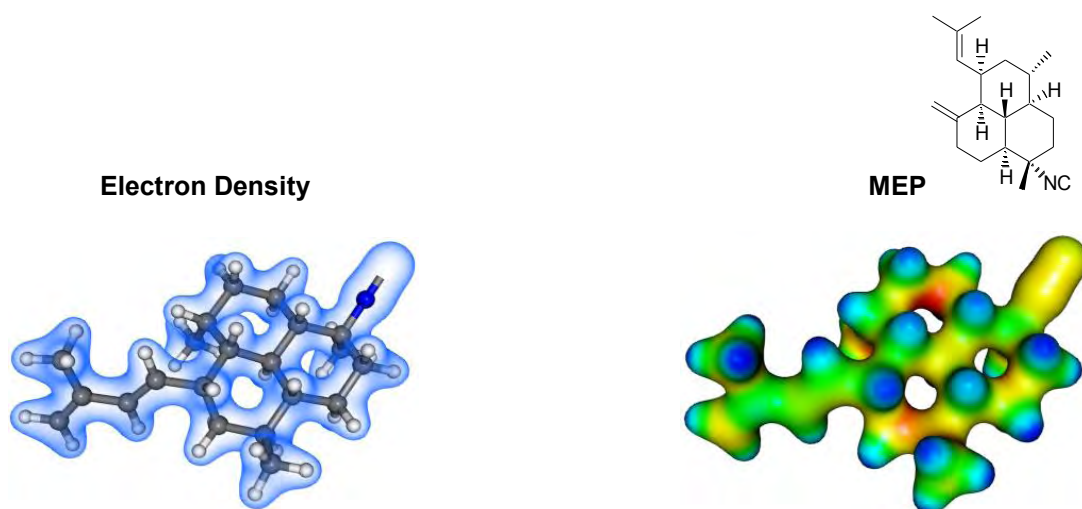


Figure 2.32: Molecular electrostatic potential (right) superimposed on a map of total electronic density (left) for **1.41**.

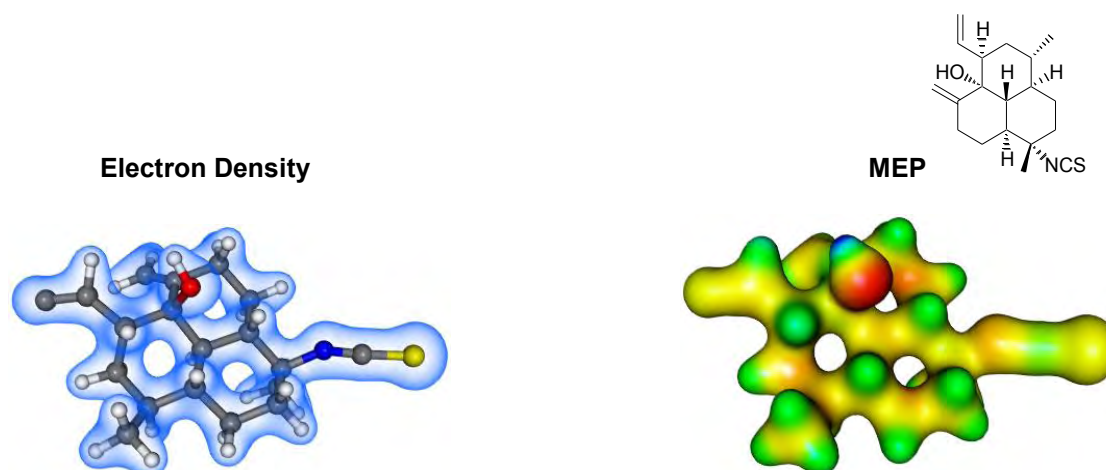


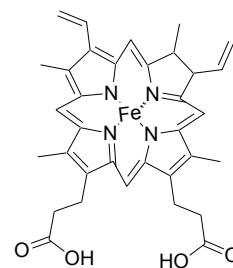
Figure 2.33: Molecular electrostatic potential (right) superimposed on a map of total electronic density (left) for **1.42**.

A characteristic feature of these compounds is the highly saturated polycyclic carbon framework forming the backbone of the molecules and onto which the various hetero-atom functional groups are attached. The MEP maps are electronic topologies⁷⁸ which give an indication of the kinds of interactions the molecules could engage in with receptor molecules. The marine compounds exhibit electropositive potentials along their carbon frameworks, with the hydrogens forming nodes of very high electropositivity (indicated by their deep blue colouring). The heteroatom functional groups possess electronegative potentials, with the isocyanates being very negative on their oxygen atoms and very positive on their nitrogen atom. The isothiocyanates are slightly negative through to slightly positive across the whole group, without any significant charge gradient from the nitrogen to the sulphur; though the nitrogen is generally more negative. The isonitriles have relatively negative potentials, with the nitrogen possessing a slightly more negative potential than the isonitrile carbon atom.

2.7 Molecular Electrostatic Topologies of Free Heme and the β -Hematin Dimer

In the same way that it is important to understand both the inhibitor and receptor bonding orbitals to investigate potential intermolecular bonds, so too is it important to understand the electrostatic surfaces of these models to investigate potential intermolecular attractions and repulsions. MEP surfaces were calculated from the population analysis files (Section 2.4) and superimposed on maps of total electronic density:

2.7.1 Molecular Electrostatic Topology for Free Heme



Electron Density

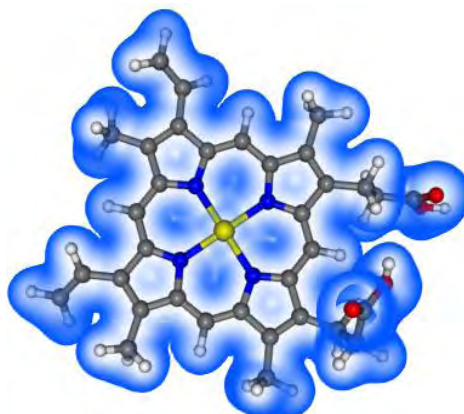


Figure 2.34: Total electronic density for free heme, as viewed from above the ring plane.

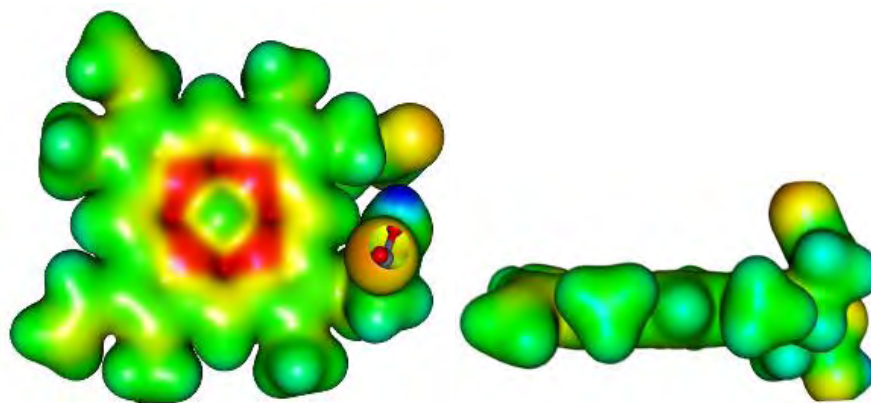


Figure 2.35: MEP superimposed on a map of total electronic density for free heme, as viewed from above the ring plane (left) and within the ring plane (right).

As can be seen in the MEP maps above, the heme molecule has a positive centre due to the nitrogens drawing electron density away from the central iron atom. Consequently, the nitrogens (red) are very negative and the carbons (yellow) next to them in the porphyrin ring also carry a slightly negative potential. The rest of the porphyrin carries a slightly positive potential, with slightly negative regions (yellow) due to double bonds being present. The acid side chains are positive along their carbons with the oxygen atoms carrying negative potential and the very polar acid hydrogen exhibiting a strongly positive potential. The potential of the oxygen attached to the acidic hydrogen is not particularly negative in nature and only appears yellow on the MEP. Due to these potentials, positive centers of ligand molecules will most likely orientate themselves with the negative porphyrin center and negative regions/functionalities will be drawn to positive potentials on the outer regions of the ring or acid tails.

2.7.2 Molecular Electrostatic Topology for β -Hematin Dimer

MEP surfaces were calculated from the population analysis files (Section 2.4) and superimposed on maps of total electronic density:

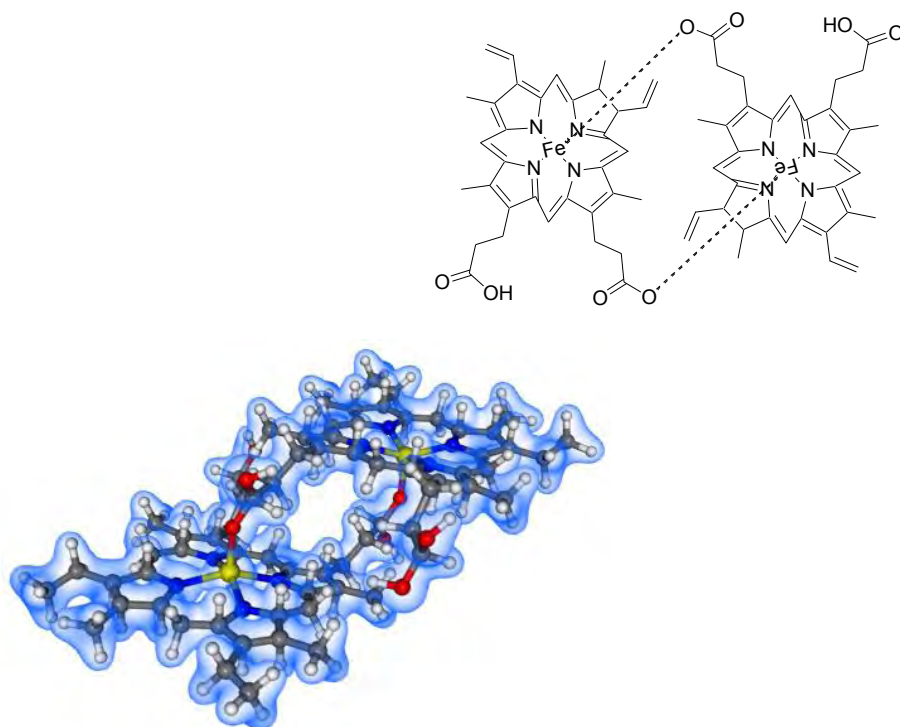


Figure 2.36: Total electronic density for the β -hematin dimer.

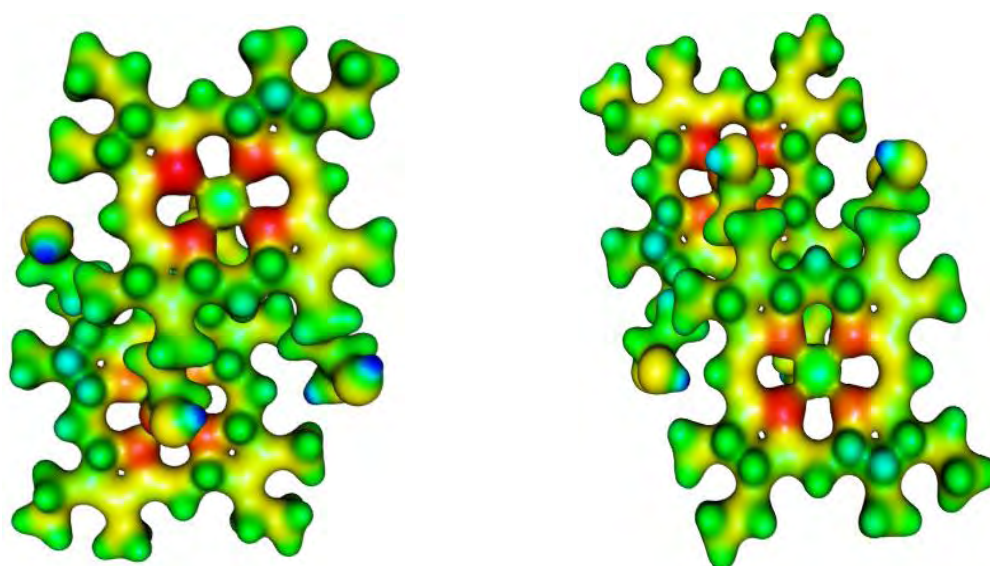


Figure 2.37: Total electronic density for the β -hematin dimer, as viewed from above the ring plane.

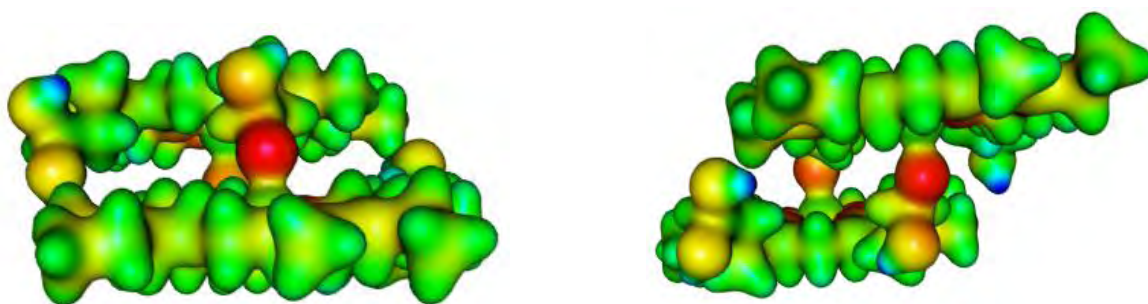


Figure 2.38: Total electronic density for the β -hematin dimer, as viewed within the ring plane.

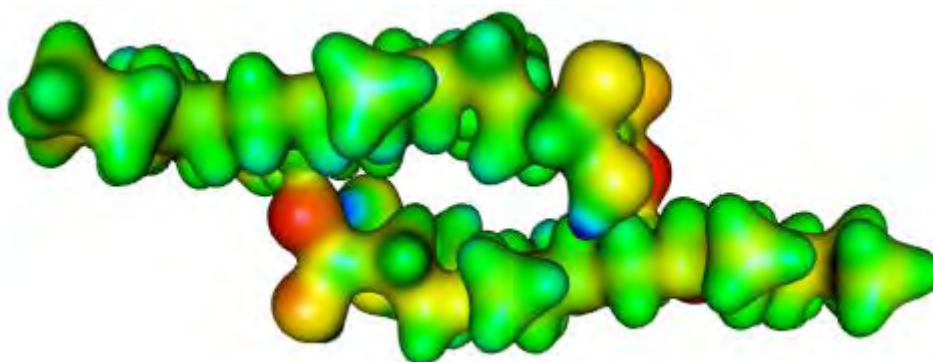


Figure 2.39: Total electronic density for the β -hematin dimer, as viewed sideways.

The β -hematin dimer has very similar electrostatics to the free heme model. The porphyrin rings still have positive iron centers with the very negative pyrrolic nitrogens surrounding them. A slight difference to the potential of the free heme group is that the negative potential extends out further from the nitrogens; and the planar faces (shown as top and bottom views) exhibit a predominantly more negative general potential to that of a lone heme moiety. This will encourage the approach of positively charged molecules/parts of molecules, and resist those that are negative in a slightly more intense way than for free heme.

A new potential binding position is found at 45° to the molecular plane, with the ligand molecules being able to approach the oxygen linkages between the two heme groups as shown in see **Figure 2.40**. This zone, by virtue of the highly electronegative oxygen groups, exhibits a strongly negative

general electrostatic potential and so this mode of approach will be limited to positively charged molecules/molecular centers. Chloroquine, with its long and flexible side-chain, has been shown to interact with this site in conjunction with the primary planar surface³⁴ and it may be possible that those marine compounds possessing a similar side-chain, e.g. compound **1.39**, may behave in a similar fashion.

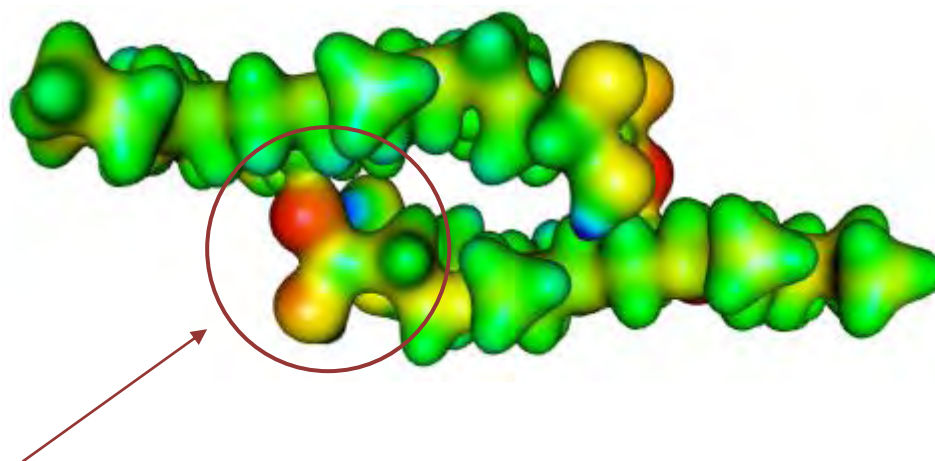


Figure 2.40: The negative oxygen linkages, indicated by their red colouring, are circled and will be approached at 45° to the plane of the porphyrin rings. The arrow indicates the approach vector of molecules possessing suitably positive MEPs.

2.8 Summary

The isocontour maps of the HOMO and LUMO orbitals suggest that the most likely place for intermolecular bonding for the isonitrile compounds is not in fact the isonitrile functionality itself. As most of the electronic density in these orbitals is located along the carbon molecular framework, electronic intermolecular interactions will most likely not involve the isonitrile functionalities. The orbital contributions of the isocyanate and isothiocyanate groups are considerably more significant however and possess the necessary shape to potentially interact with the heme receptor orbitals.

The electrostatic potentials of the isonitrile functionalities are also mismatched for attraction to the porphyrin ring centers on their heme targets due to the highly negative potentials of the isonitrile

group and the pyrrolic heme nitrogens. The electrostatic potentials of the molecular backbones of the marine models should, however, result in favorable interactions with the target molecules. The interactions of the MEPs of the marine compounds will be a strong determining factor in their mode of approach to the heme receptors and will influence their efficacies as potential inhibitors of heme polymerization via their binding to these receptors. A prediction that can be made from the MEPs obtained is that the ligand molecules will align their positively charged carbon backbones with the negative porphyrin zones in predominantly planar conformations. Heteroatom functionalities on these backbones will most likely influence the steering of molecules on their approach through the interaction of their (usually) strong electrostatic potentials with complementary heme regions. These intermolecular interactions will be explored in greater detail by means of statistical ligand docking analyses in Chapter 3.

EXPLORING THE CONFORMATIONAL SPACE OF INHIBITORS AROUND HEME STRUCTURES AS FOUND IN THE FOOD VACUOLE OF *P. FALCIPARUM*

Whilst the electrostatic calculations performed in Chapter 2 provide information on the intrinsic properties of the molecules being studied, an adequate simulation of the interactions between the receptor molecules and their inhibitors is needed. A thorough investigation of these interactions requires an adequate exploration of the conformational spaces of the receptors and their inhibitors, coupled with a reasonably accurate energy evaluation method to find the lowest energy conformers.

3.1 Docking Algorithms

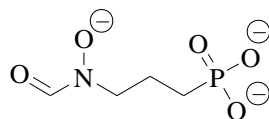
The ability of force-field methodologies to efficiently compute the energies of very large systems (up to many thousands of atoms) has resulted in their implementation in protein docking methodologies where energy calculations are used to explore interactions between protein receptors and smaller 'ligand' molecules.⁷⁴ Docking simulations require a combination of two basic methods: a search method to explore the conformational space available to the system being studied and a force field to evaluate the various conformations' energies.⁷⁹ A trade-off needs to be made, depending on computational time available, between the accuracy of the energy calculations and the degree of conformational space explored, i.e. the more accurate the energy determination, the less of conformational space that can be explored. The force fields used in these programs are usually similar in form to Eq. 1, though often contain a desolvation term as well. The ability of docking algorithms to efficiently explore ligand conformational space around a receptor has resulted in their use as a means to identify potential protein drug targets and assist in the rational design of new inhibitor models. Currently, the most literature cited docking algorithm is AutoDock^{74,79} which incorporates a modified AMBER⁸⁰ force-field coupled with a Lamarckian genetic search algorithm.⁸¹

Although AutoDock is the most cited methodology in the literature at present, force field methodologies in general often sacrifice calculation accuracy for the sake of expedience.⁷⁴ As the heme models are relatively small compared to macromolecules such as proteins and the conformational space around the models is nearly a complete sphere, i.e. ligand molecules can approach from all directions; the method would have to be particularly accurate in its energy evaluations. Coupled with the unique charge distributions across functionalities like isonitriles, this necessitated an evaluation of AutoDock before it could be used to model the heme systems. A joint project with Goble and co-workers provided an opportunity to evaluate the efficacy of this docking algorithm by using it to validate a theoretical *P. falciparum* 1-deoxy-D-xylulose-5-phosphate reductoisomerase enzyme (*PfDXP*) protein model through extensive docking analyses, whilst also contributing to the development of new *PfDXR* inhibitors. The work performed in Section 3.2 of this thesis was used to confirm that the theoretical protein model designed and constructed by Goble and co-workers could emulate *PfDXR*'s behaviour *in silico*, and could be used for the rational design of novel inhibitor molecules.⁸²

3.2 Validation of a Theoretical Malarial 1-Deoxy-D-xylulose-5-phosphate Reductoisomerase Enzyme Model

3.2.1 Introduction

The MEP pathway, as found in the apicoplast organelle of *P. falciparum*, comprises seven enzyme catalyzed steps. The initial steps of this series involve the production of 1-deoxy-D-xylulose-5-phosphate (DXP) via a condensation of pyruvate and glyceraldehydes,⁸³ followed by a reduction to 2-C-methyl-erythritol 4-phosphate (MEP),⁸⁴ catalyzed by DXR. The DXR enzyme of *E. coli* has been characterized via X-ray crystallographic methods, and a great deal of information is available describing its biological mechanism.⁸⁵⁻⁸⁷ It is a homodimeric protein,⁸⁵ possessing a flexible loop of residues which covers the substrate binding site and provides DXP binding specificity.⁸⁶ A disruption of this reductive step in the MEP pathway would greatly inhibit parasitic development. Presently, the most potent DXR inhibitor is the antibacterial agent fosmidomycin (FOS, **3.1**).⁸⁸



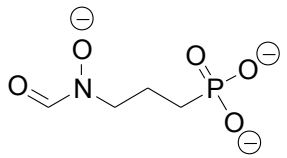
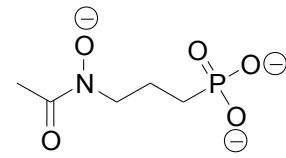
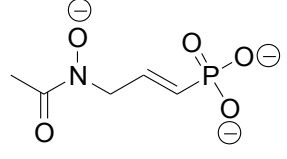
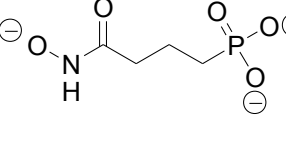
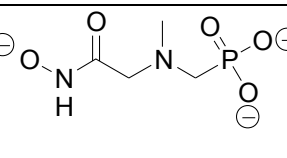
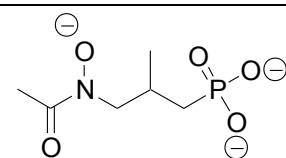
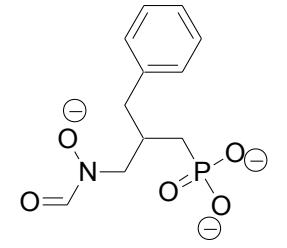
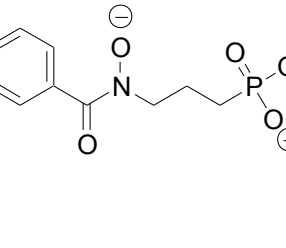
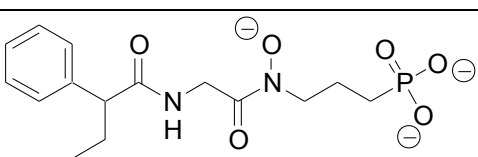
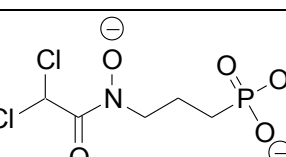
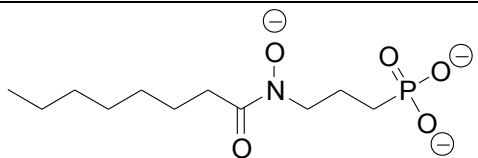
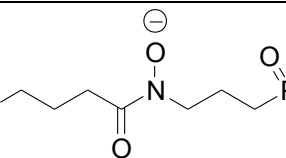
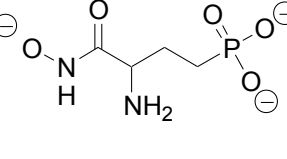
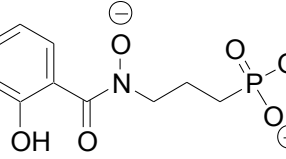
3.1

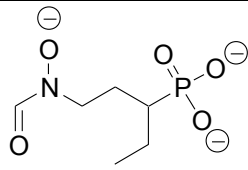
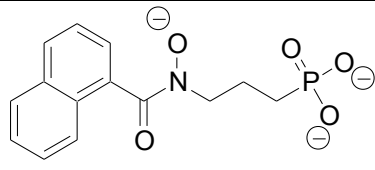
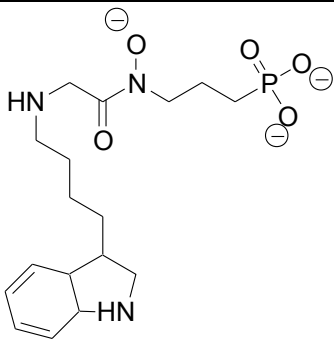
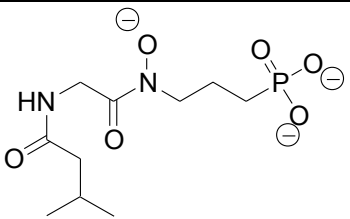
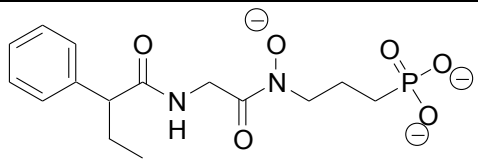
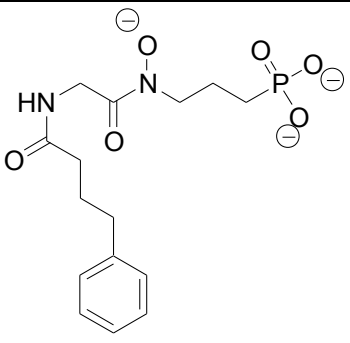
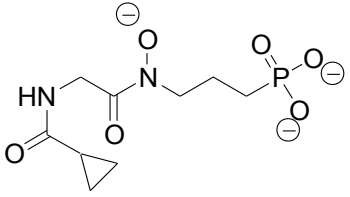
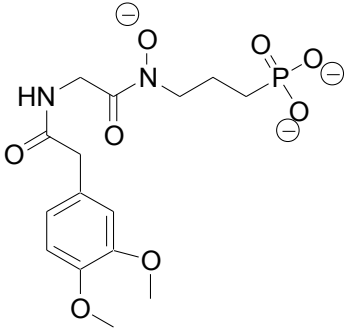
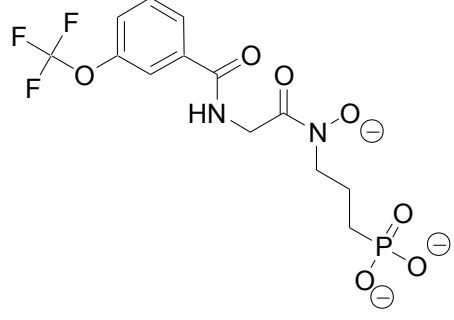
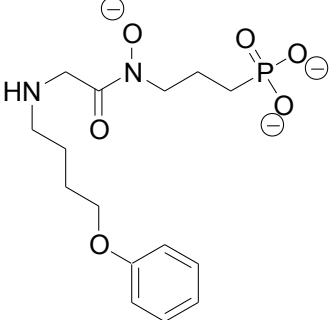
Successful crystallization of FOS in complex with *E. coli* DXR (*EcDXR*), NADPH (nicotinamide adenine dinucleotide phosphate) and Mn^{2+} indicated that it binds to DXR in a similar fashion to DXP. Although FOS exhibits potent inhibitory properties, it has a greatly reduced pharmacological potential. As a result, new inhibitors exhibiting similar inhibitory properties to FOS yet possessing better drug potential are required. Recently, several groups of new inhibitors have been identified and their inhibitory properties determined.⁸⁹⁻⁹³

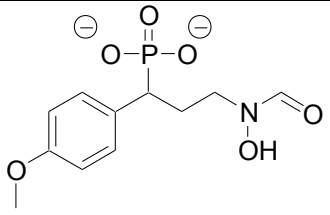
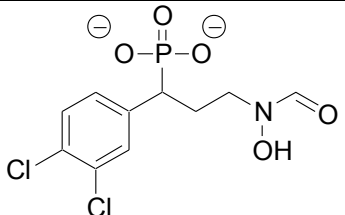
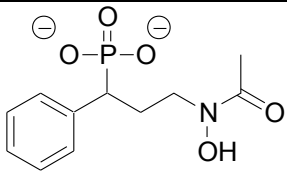
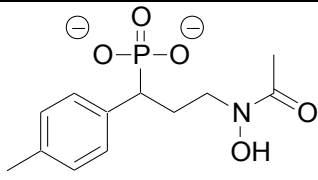
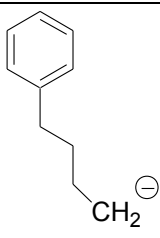
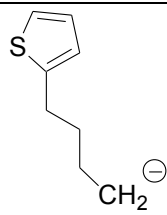
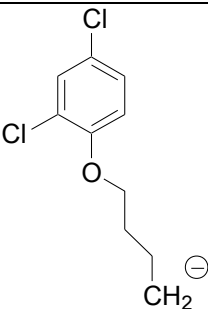
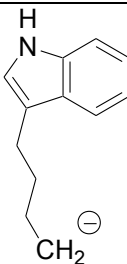
No experimentally determined *P. falciparum* DXR (*PfDXR*) structure has been published; however it remains important that a suitably similar model be established to provide information on protein structure and to facilitate rational inhibitor design. One such model was produced and successfully used for *in silico* docking analyses by Singh *et al.*,⁹⁴ though the structure was not published nor made freely available. This structure was also developed when the *PfDXR* inhibitor library was not as extensive as it is now⁸⁸ and with new information available from more recent experimental binding studies, a proposed model can now undergo a much more rigorous computational analysis.

In a parallel study with the Biochemistry Department at Rhodes University, a new theoretical *PfDXR* model, constructed through homology modeling to the well established *E. coli* protein structure by Goble and co-workers⁸² was made available for just such a validation. Fortuitously, this allowed us to explore AutoDock's capabilities as a docking algorithm whilst contributing to the development of novel anti-malarial drug discovery. We comparatively docked over 30 ligands into the *PfDXR* and *EcDXR* models, followed by an analysis of binding affinity versus literature experimental IC_{50} values to investigate the protein model's potential for use in the rational design of novel *PfDXR* inhibitors. The structures of the ligands used are contained in **Table 2.1**:

Table 3.1: Structures of the ligands used as a test set for the theoretical *Pf*DXR model constructed by Goble and co-workers.

No.	Structure	No.	Structure
3.1		3.2	
3.3		3.4	
3.5		3.6	
3.7		3.8	
3.9		3.10	
3.11		3.12	
3.13		3.14	

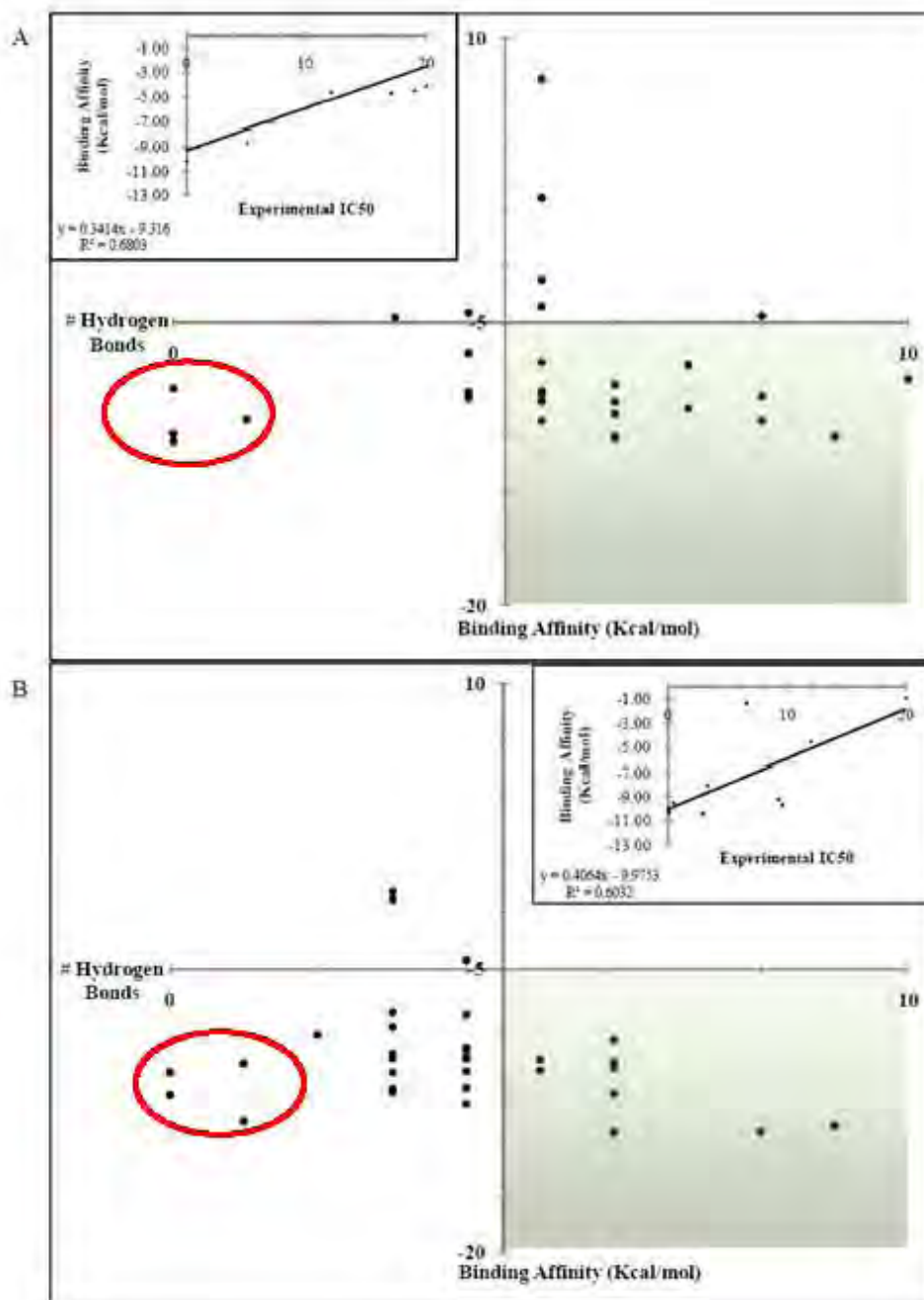
3.15		3.16	
3.17		3.18	
3.19		3.20	
3.21		3.22	
3.23		3.24	

3.25		3.26	
3.27		3.28	
3.29		3.30	
3.31		3.32	

3.2.2 Results and Discussion

A minimized fosmidomycin structure was initially docked back into the primed *EcDXR* to confirm that the docking protocol was adequately simulating the active site system. The subsequent docks fitted well with the literature crystal structure and so this protocol was applied to the other 30 ligands. The best docking results were chosen based on the greatest number of electrostatic interactions with the active site proteins, orientation of the ligand in the active site, and the ligand binding affinity. Structurally similar ligands exhibited similar orientations. All ligands were quantified with respect to binding affinity and the number of hydrogen bonding interactions. The theoretical inhibition potential of each ligand was graphically classified into a quadrant graph plotting binding affinity against number of

electrostatic interactions. This method of quantification provides an efficient means of screening for potential rational designing of novel DXR inhibitors. This can be seen in **Graph 3.1**:



Graph 3.1: Graphs of binding affinity versus number of hydrogen bonds for *EcDXR* (A) and *PfDXR* (B), along with plots of binding affinity versus experimental IC₅₀. The coloured quadrants contain those ligands with optimal binding qualities. The red circles the especially poor binding ligands **3.29 – 3.32**.

This analysis allows for one to observe “artifact” behavior, i.e. those molecules which can enter the active site easily, yet are not held strongly in place via hydrogen bonds with the binding site residues. Ligands that possessed the lowest (most negative) binding energies as well as high levels of interaction included:

EcDXR: **3.1, 3.2, 3.3, 3.4, 3.6, 3.7, 3.10, 3.12, 3.13, 3.14, 3.15,**

PfDXR: **3.1, 3.2, 3.7, 3.12, 3.13, 3.32**

In the case of the phosphate mimics (**3.17 – 3.24**),⁹³ α -substituted FOS analogues (**3.25 – 3.28**)⁹² and DOXP-reductoisomerase inhibitors (**3.1 – 3.16**),⁹¹ it was evident that a phosphonate moiety, as well as a nitrogen atom carrying significant negative charge, was required for reasonable binding of the active residues. When the 3'-amido-3'-deoxy-N6-(1-naphthylmethyl) adenosine derivatives (**3.29 – 3.32**)⁹⁰ were docked into *EcDXR* and *PfDXR*, very few hydrogen bonding interactions were observed (**Graph 3.1**). The ligands from this group are not bulky and therefore entered the active site efficiently and this is most likely responsible for the reasonable binding affinities. The lack of electrostatic interactions suggests that these ligands may be artifacts, moving freely between the active site and external environment. The lack of interaction may be a consequence of the lack of highly charged nitrogen atoms or phosphonate moieties in the structures. This method, whilst providing significant information on the nature of ligand-receptor interaction, relies on the presence of hydrogen bond donor/acceptor systems. As such, it could not be implemented in the subsequent binding studies of the heme systems as most of the marine compounds (**1.30 – 1.42**) do not possess polar hydrogens capable of forming such bonds.

An interesting trend was noted in the different behaviours of ligands with bulky side chains in their interactions with the *EcDXR* compared to *PfDXR*. Those ligands with bulky side chains showed signs of forming intra-molecular bonds, thereby adopting a more compact conformation, to facilitate entry into the active site. The conformations of these ligands were very different to those of their minimized states. As an example, in **Figure 3.1**, when ligand **3.23** was docked into *PfDXR*, the ligand adopted a

reasonable linear arrangement comparable with that of the minimized ligand. When docked into *EcDXR*, ligand **3.23** assumed an entirely new conformation.

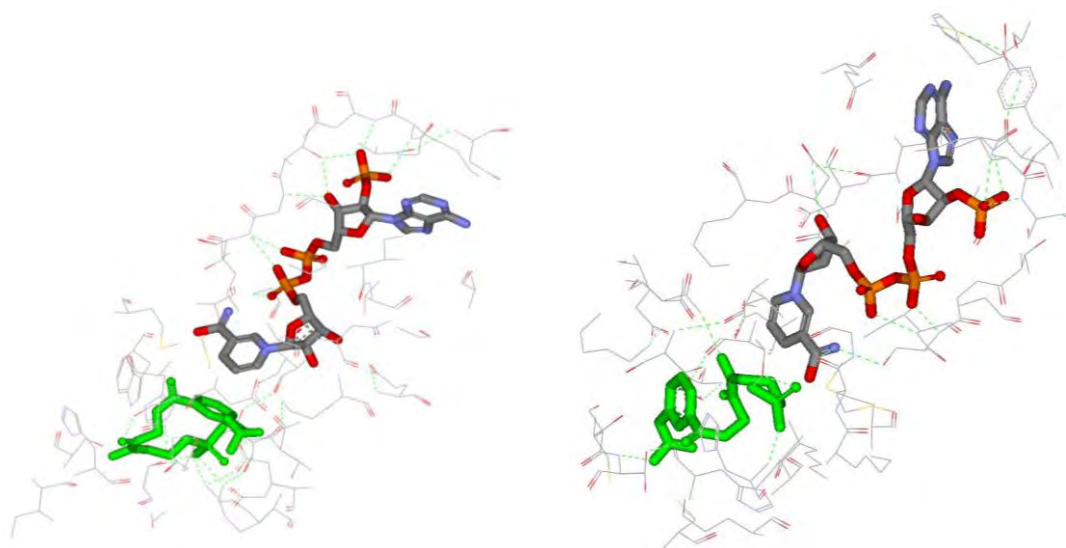


Figure 3.1: The different conformations adopted by ligand **3.23** (green), compact (left) and extended (right), during docking with *EcDXR* and *PfDXR* respectively in the presence of NADPH (second tubular structure).

In the literature, interactions with *EcDXR* residues Gly197 (Gly200 in *PfDXR*) and His219 (His222 in *PfDXR*) have been shown to exhibit “hatch-like” behaviour in the *EcDXR*-NADPH-fosmidomycin complex.⁹⁴ Although the direct “hatch” interactions were not observed in the FOS (**3.1**) docking runs, they were observed in the docking of **3.2** and **3.22** (for Gly200) into *PfDXR*. Residues interacting with **3.2** were: Ser199, Ser235, Asn240, Lys241 and Gly200 in *PfDXR*, and Ser186, Ser222, Asn227, Lys228, Glu231, Ser151 and Gly185 in *EcDXR*. These interactions can be seen in **Figure 3.2** and **Figure 3.3** respectively. Similarly, interactions with **3.23** and **3.16** were also apparent (for His222) when docked into *PfDXR*. The hydrogen bonding interaction between His209 (His222 in *PfDXR*) and the phosphonate moiety of the substrate is said to be the reason for the closing of the hatch once the substrate has entered,^{95,85} shielding the reactants completely from the solvent environment. When FOS (**3.1**) was docked into *PfDXR* the phosphonate moiety of the ligand interacted with the following residues: Ser199, Ser235, Asn240 and Lys241 in *PfDXR* (Ser186, Ser222, Asn227 and Lys228 in

EcDXR). Rather than a direct interaction, Glu244 in *PfDXR* (Glu231 in *EcDXR*), played a supporting role to stabilize the catalytic lysine.

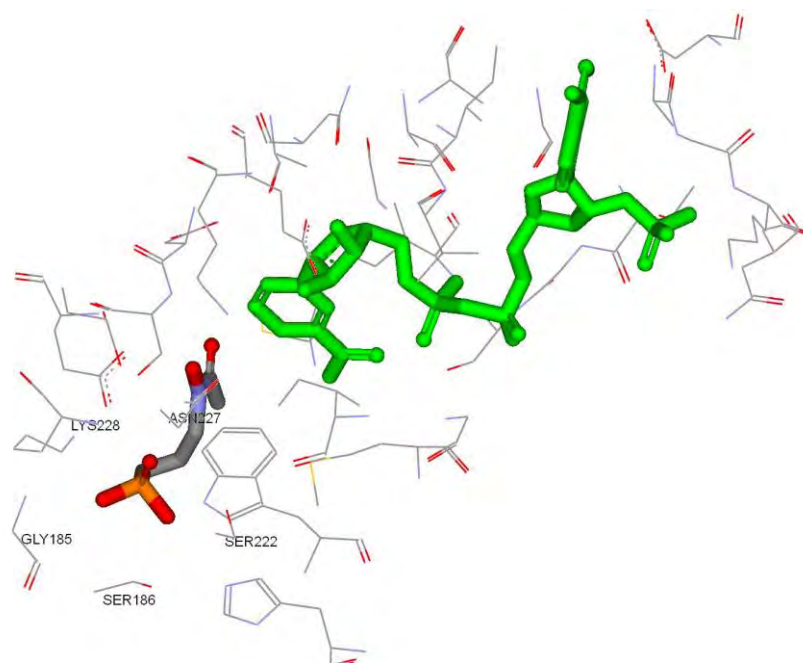


Figure 3.2: Interaction between ligand 3.2 (coloured tubular structure) and “hatch” residues in *EcDXR*, in the presence of NADPH (green).

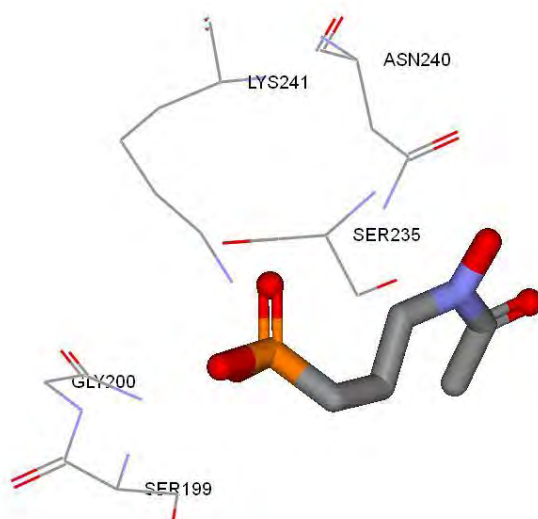


Figure 3.3: Interaction between ligand 3.3 (coloured tubular structure) and “hatch” residues in *PfDXR*.

Statistically, there should be a correlation between the experimental *EcDXR* and *PfDXR* IC₅₀ values and computational binding affinities. An example of this correlation could be seen with the binding affinities for **3.19** docked into *EcDXR* and *PfDXR*. Binding affinities were -4.15 and -12.16 kcal/mol respectively, meaning that the experimental IC₅₀ for *PfDXR* should theoretically show a 2.9-fold increase. Experimentally, **3.19** was found to demonstrate a 2.2-fold higher inhibition of *PfDXR* when compared to *EcDXR*.⁹³ The other phosphate mimics (**3.17 – 3.24**), demonstrated the same trend indicating that the theoretical *PfDXR* model behaves in a similar manner to the *PfDXR* enzyme experimentally.

In conclusion, the *PfDXR* theoretical model, through binding energy, may provide some evidence of the potential inhibitory strength (IC₅₀) of compounds. The *PfDXR* model can hence be used to screen groups of compounds and may also provide a rational basis from which new and more effective compounds can be designed. Although AutoDock proved to be sufficient as a docking algorithm for the evaluation of potential antagonists of *PfDXR*, its applicability to the simulation of heme inhibition systems requires further discussion.

3.3 Is AutoDock a Valid Docking Algorithm?

Although AutoDock proved to be sufficient as a docking algorithm, a limitation of its empirical methods became evident and this would require attention before it could be applied to the heme-binding systems under investigation here. Firstly, there was little if any charge difference between atoms of similar types, e.g. nitrogen centres were given a charge of -0.346 ± 0.010 . Whilst this method is an efficient method of assigning descriptive electrostatics in large protein systems where the “luxury” of highly accurate calculations is often not affordable, the small size of the heme-ligand systems would allow for explicitly determined charges to be used.⁷⁴ Secondly, whilst empirical charge methods are generally parameterized for most elements present in organic molecules, they are poorly expressed for transition metals as could be seen in the AutoDock parameter set file (part of the software package).⁹⁶ This would present future problems in the description of the iron atom present in heme. In light of these limitations and due to the relatively small size of the heme-ligand systems being

explored in later docking studies, it was decided that DFT charge calculations would be incorporated in place of the Gasteiger⁹⁷ empirical charges used by AutoDock. An examination of the electrostatics term (highlighted) in the free energy algorithm used by AutoDock (Eq. 4)

$$\Delta G_{\text{Total}} = \Delta G_{\text{vdw}} \sum_{i,j} \left(\frac{A_{ij}}{r_{ij}^{12}} - \frac{B_{ij}}{r_{ij}^6} \right) + \Delta G_{\text{hbond}} \sum_{i,j} E(t) \left(\frac{C_{ij}}{r_{ij}^{12}} - \frac{D_{ij}}{r_{ij}^{10}} E_{\text{hbond}} \right) + \boxed{\Delta G_{\text{elec}} \sum_{i,j} \left(\frac{q_i q_j}{\epsilon(r_{ij}) r_{ij}} \right)}$$

$$+ \Delta G_{\text{tor}} N_{\text{tor}} + \Delta G_{\text{sol}} \sum_{i,j} S_i V_j e^{(r_{ij}^2 / 2\sigma^2)}$$

... Equation 4.⁹⁶

reveals that the electrostatics term (highlighted) is independent of the other terms, i.e. it does not impact on or influence any other terms in the equation before final summation. Thus, replacing the empirical charges with DFT values will not disrupt the parameterization and should better simulate inter-molecular electrostatic interactions. The augmentation of force fields with DFT charges has precedence in the literature and should greatly enhance the accuracy of subsequent simulations.^{98,99}

3.4 Statistical Docking Analyses of Chloroquine and Marine Isonitriles, Isocyanates and Isothiocyanates

With the DFT augmented force field, the inhibitor molecules were docked against both the free heme model and the β -hematin dimer. The lowest energy conformer from each analysis was visualized with only polar hydrogens displayed:

3.4.1 Docking of Chloroquine

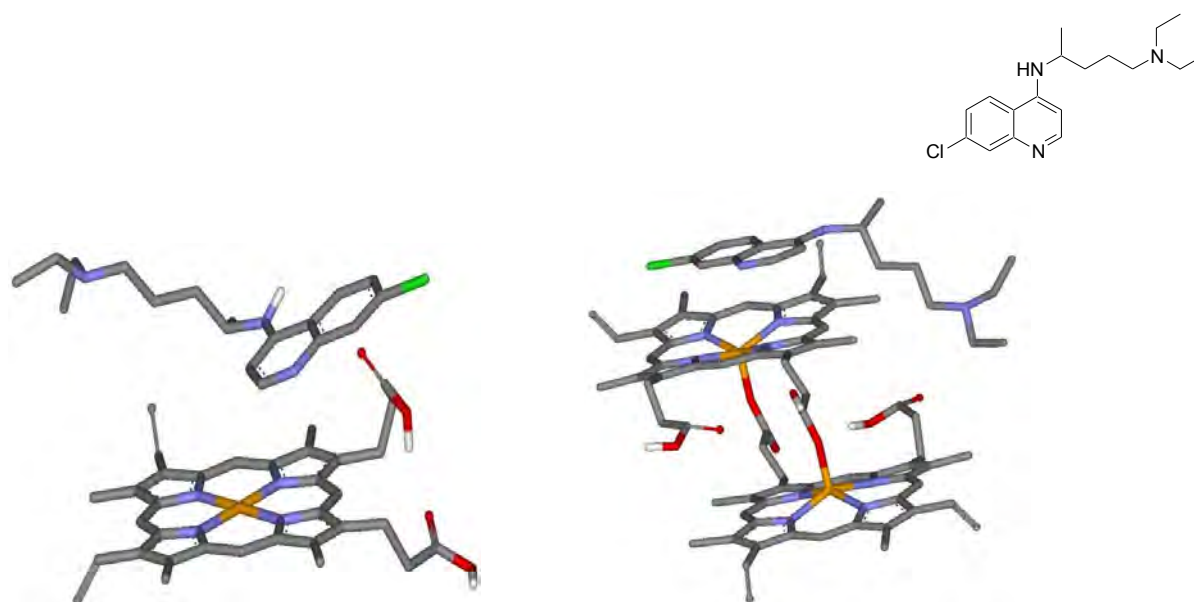


Figure 3.4: Lowest energy conformations for chloroquine docked against free heme (left) and the β -hematin (right).

Chloroquine (CQ. **1.2**) has been the frontline anti-malarial treatment for several decades and, as its inhibitory mode of action has been widely studied, it served as the control structure for evaluating the modes of action of subsequent inhibitors. As the above figures show, CQ interacts with the heme models through vertical stacking with the aromatic rings orientating themselves in parallel with the centre of the heme porphyrin rings. In the docking runs with the HD, the hydrocarbon tail of the CQ molecule orientates itself at 45° to the planes of the porphyrin rings and occupies the space immediately adjacent to the dimer molecule, consistent with the electrostatic data discussed on pp 54 - 55. The combination of this with its planar stacking across the porphyrin faces would allow for it to inhibit hemozoin crystal growth both vertically and laterally. The chloride functionality does not show any direct interaction with the receptor models but may very well be responsible for steering the molecule on its approach towards the receptor surfaces. These docking results are in agreement with the electrostatic calculations represented in Chapter 2 and with current literature.³⁴ By virtue of these agreements, the augmentation of the AutoDock force field with DFT charges has been shown to

enhance the accuracy of the algorithm and will now provide meaningful data concerning the intermolecular interactions of the marine compounds.

3.4.2 Docking of Marine Compounds

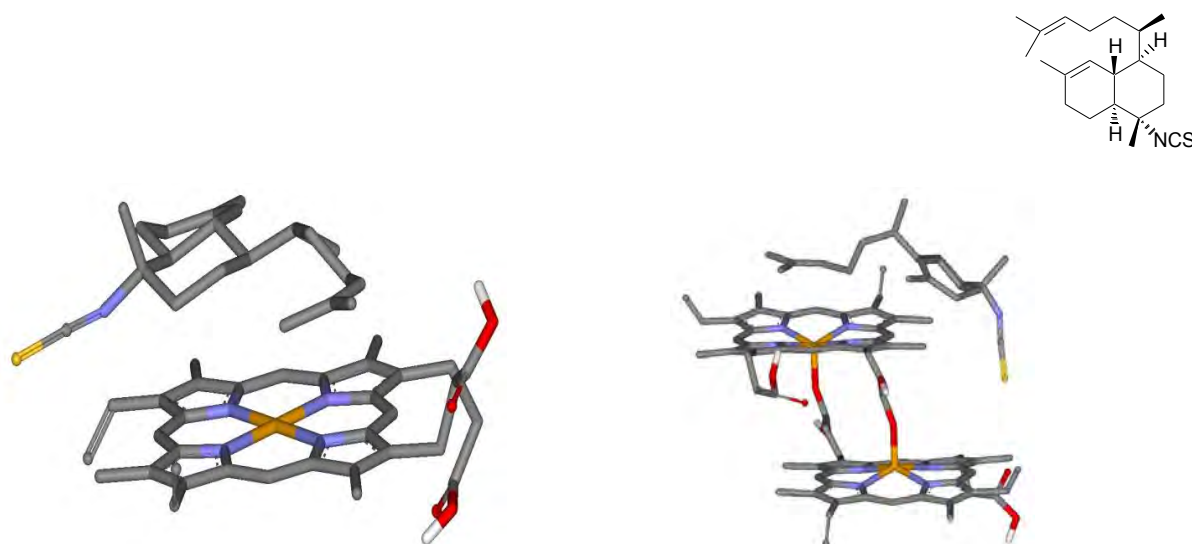


Figure 3.5: Lowest energy conformations for **1.30** docked against free heme (left) and the β -hematin dimer (right).

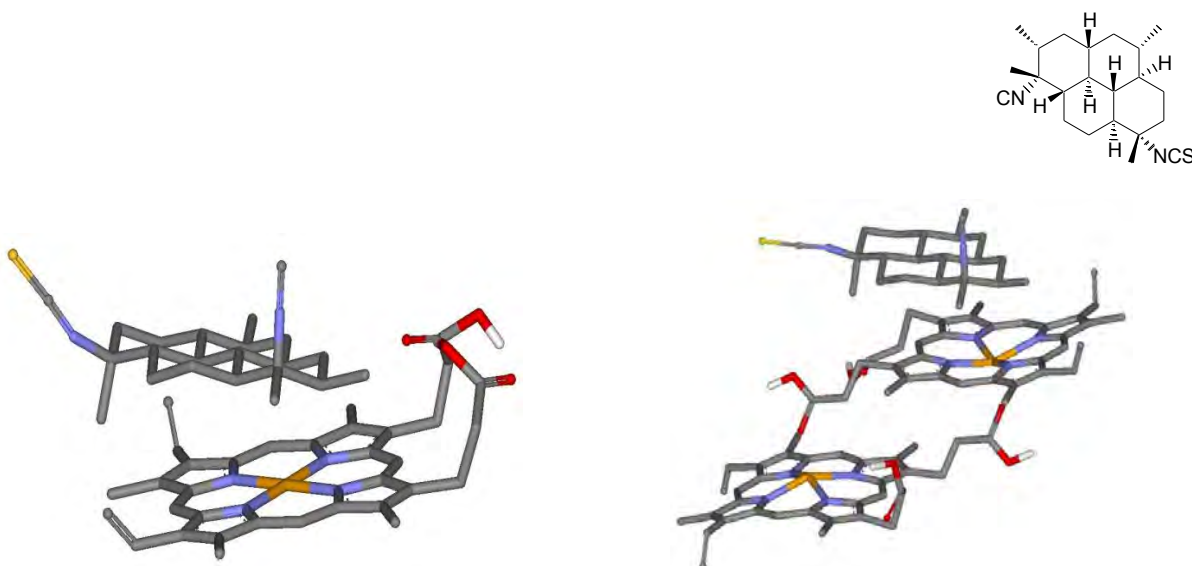


Figure 3.6: Lowest energy conformations for **1.31** docked against free heme (left) and the β -hematin dimer (right).

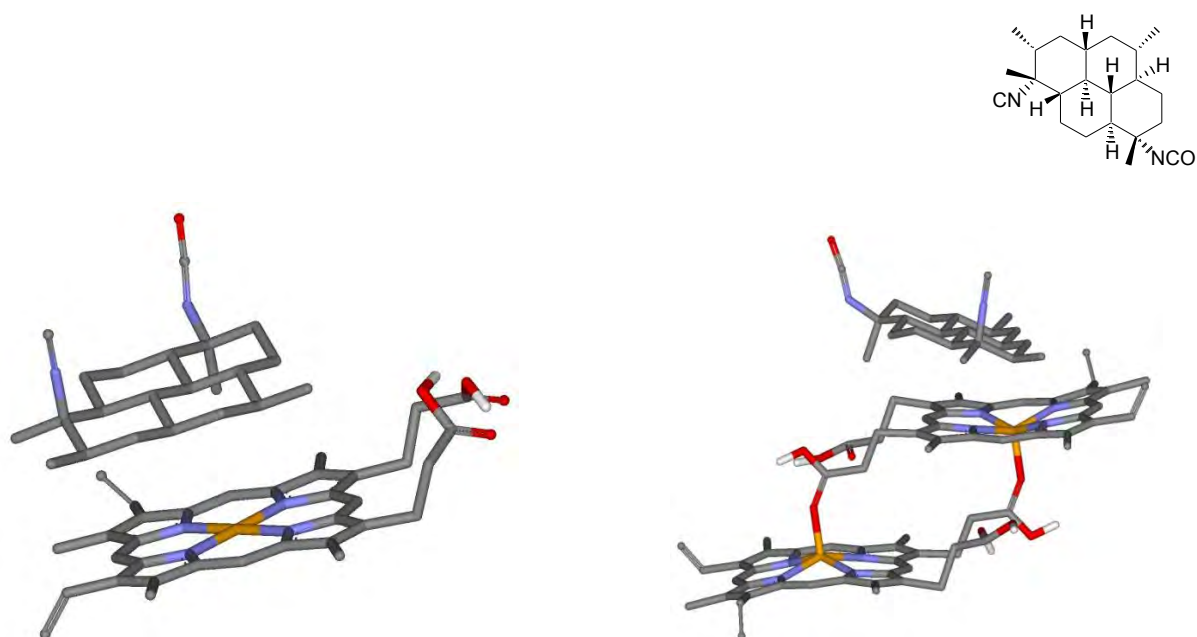


Figure 3.7: Lowest energy conformations for **1.32** docked against free heme (left) and the β -hematin dimer (right).

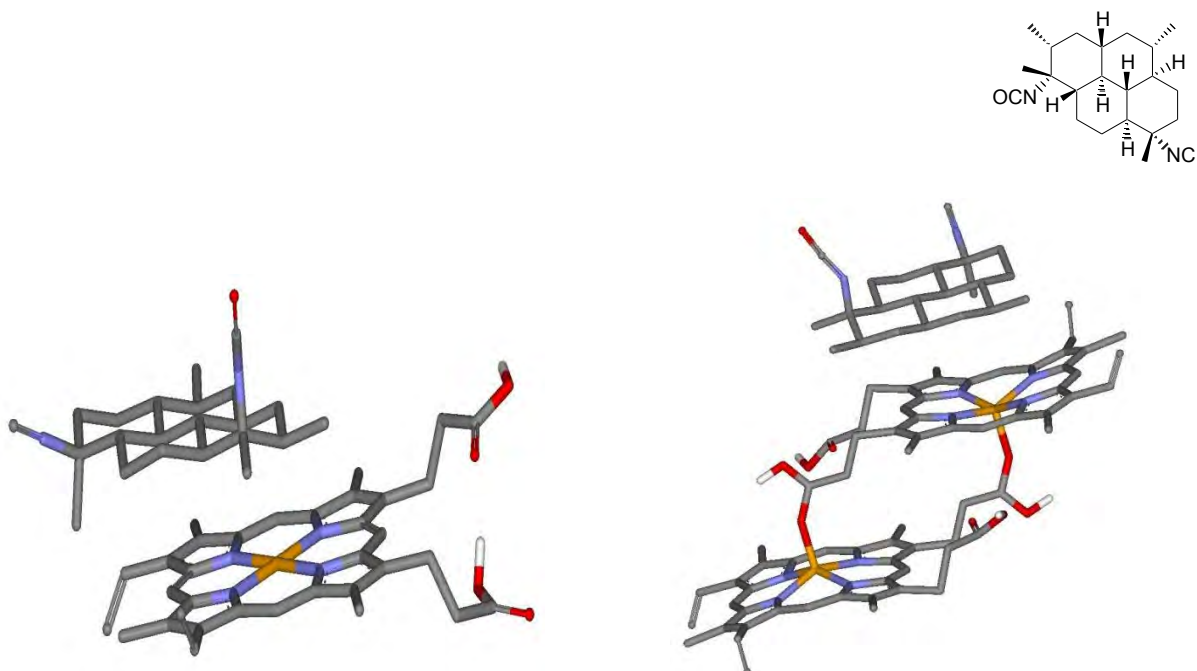


Figure 3.8: Lowest energy conformations for **1.33** docked against free heme (left) and the β -hematin dimer (right).

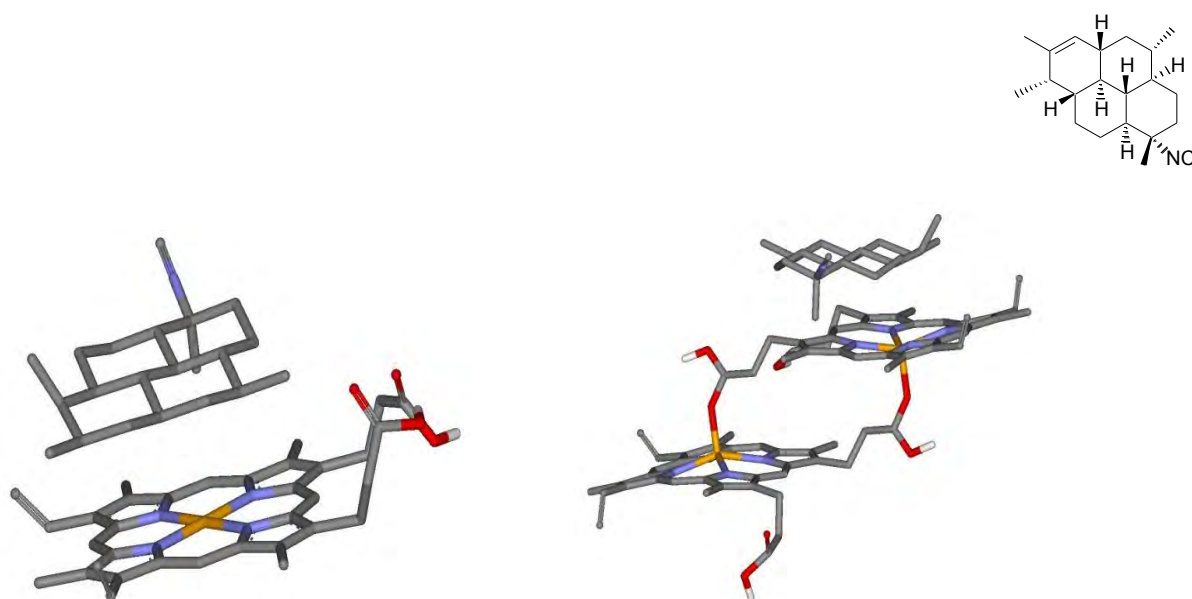


Figure 3.9: Lowest energy conformations for **1.34** docked against free heme (left) and the β -hematin dimer (right).

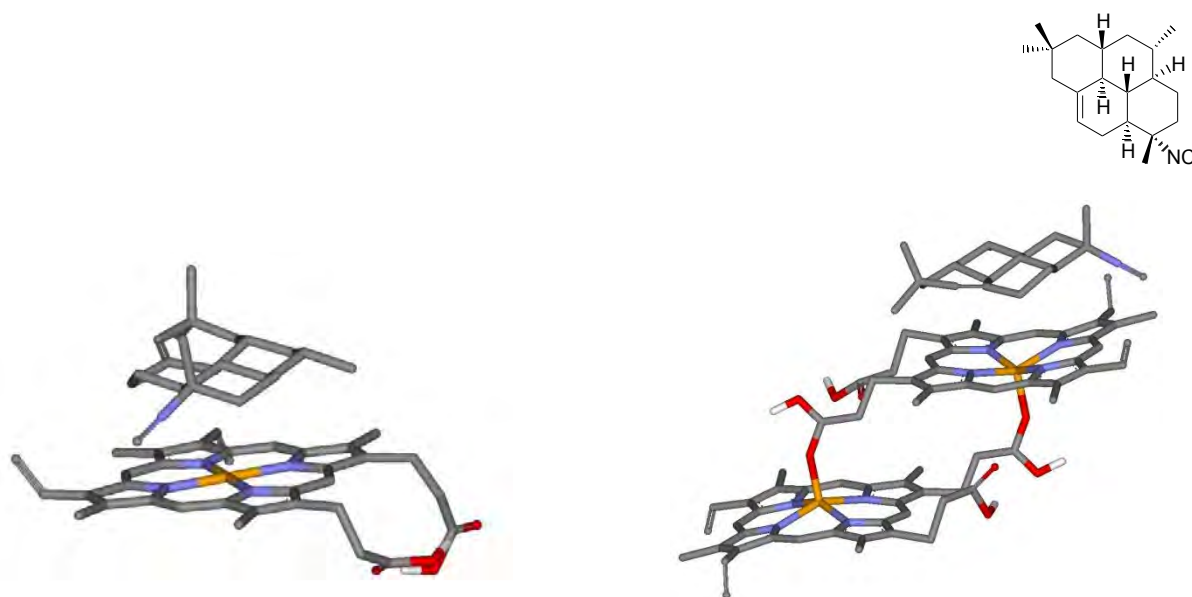


Figure 3.10: Lowest energy conformations for **1.35** docked against free heme (left) and the β -hematin dimer (right).

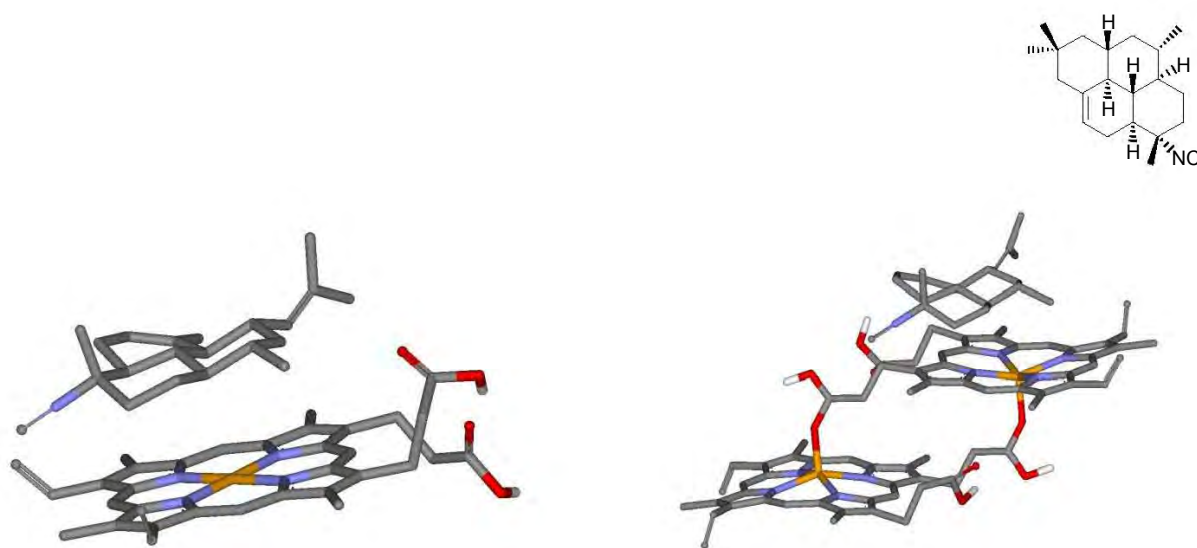


Figure 3.11: Lowest energy conformations for **1.36** docked against free heme (left) and the β -hematin dimer (right).

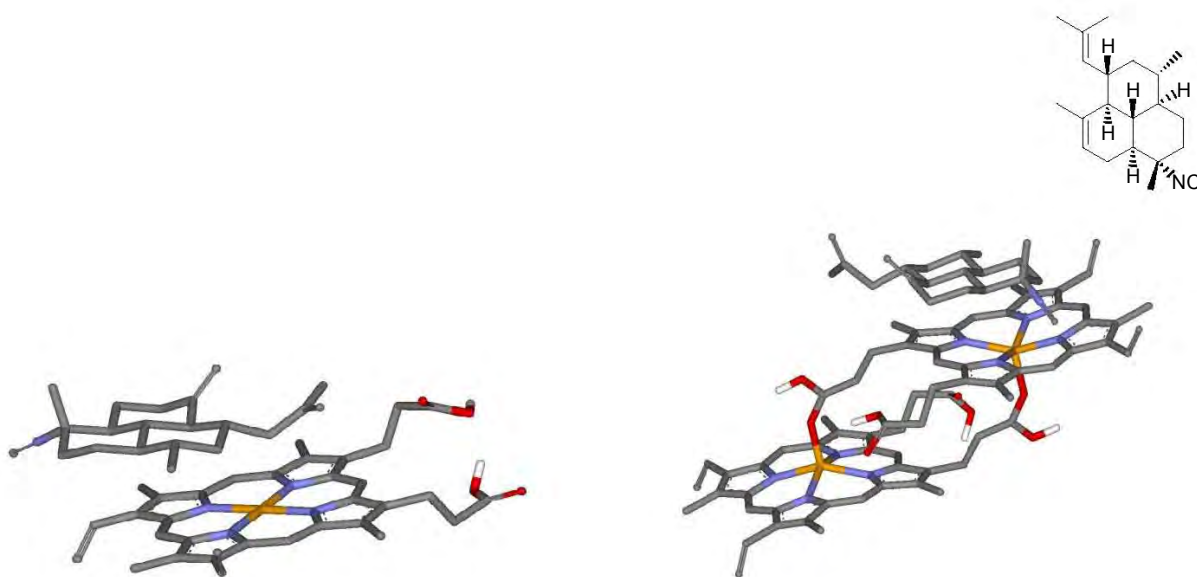


Figure 3.12: Lowest energy conformations for **1.37** docked against free heme (left) and the β -hematin dimer (right).

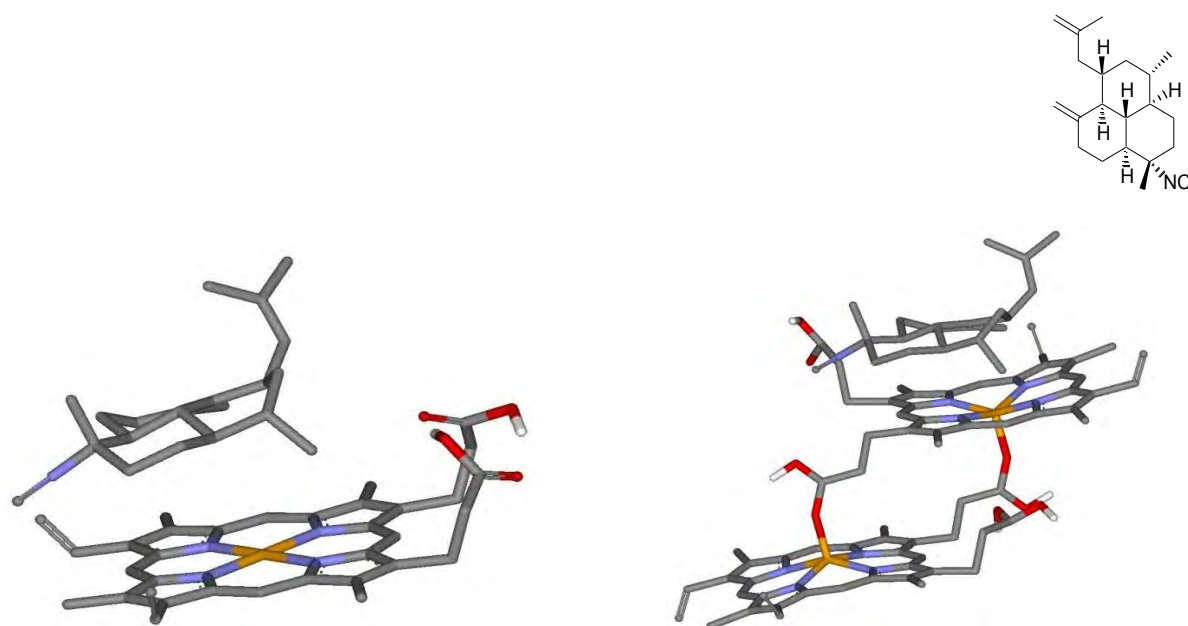


Figure 3.13: Lowest energy conformations for **1.38** docked against free heme (left) and the β -hematin dimer (right).

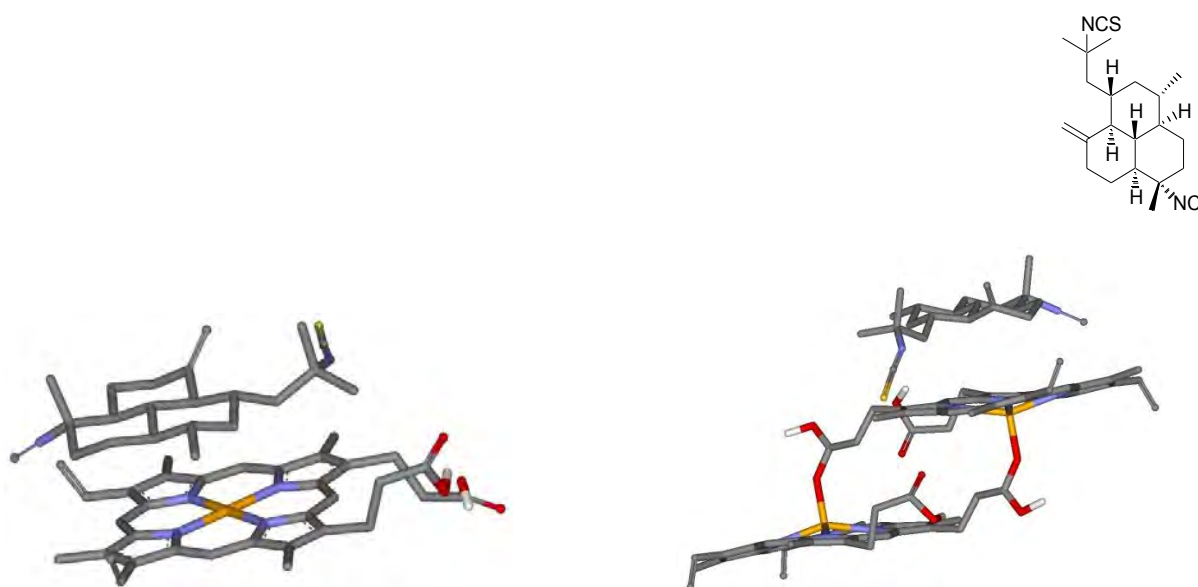


Figure 3.14: Lowest energy conformations for **1.39** docked against free heme (left) and the β -hematin dimer (right).

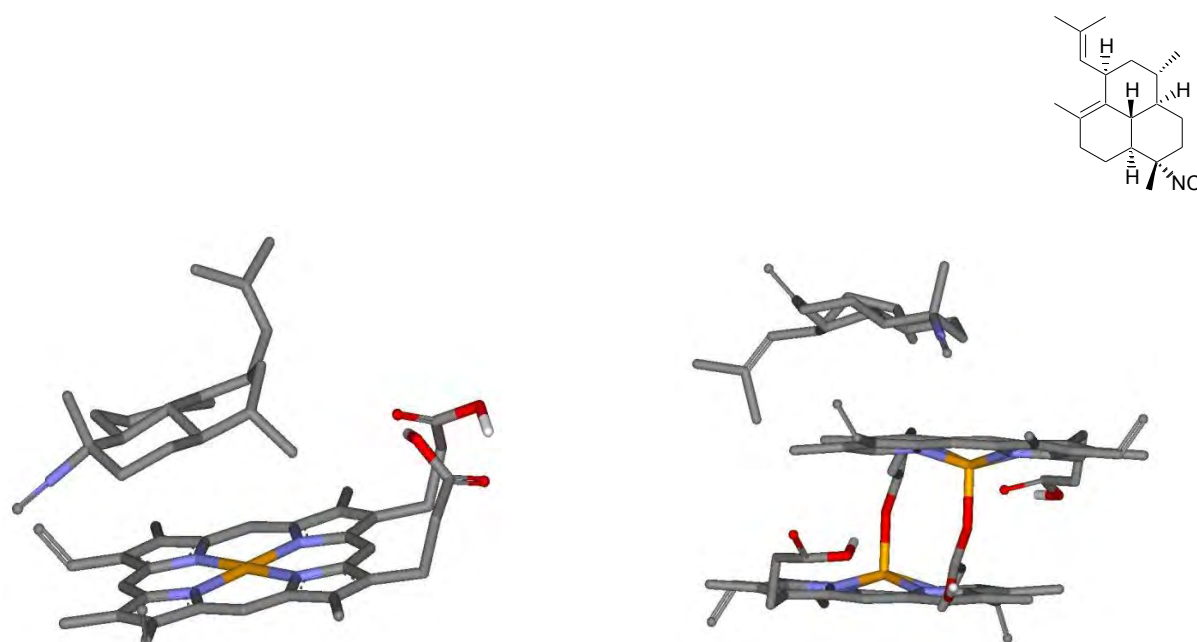


Figure 3.15: Lowest energy conformations for **1.40** docked against free heme (left) and the β -hematin dimer (right).

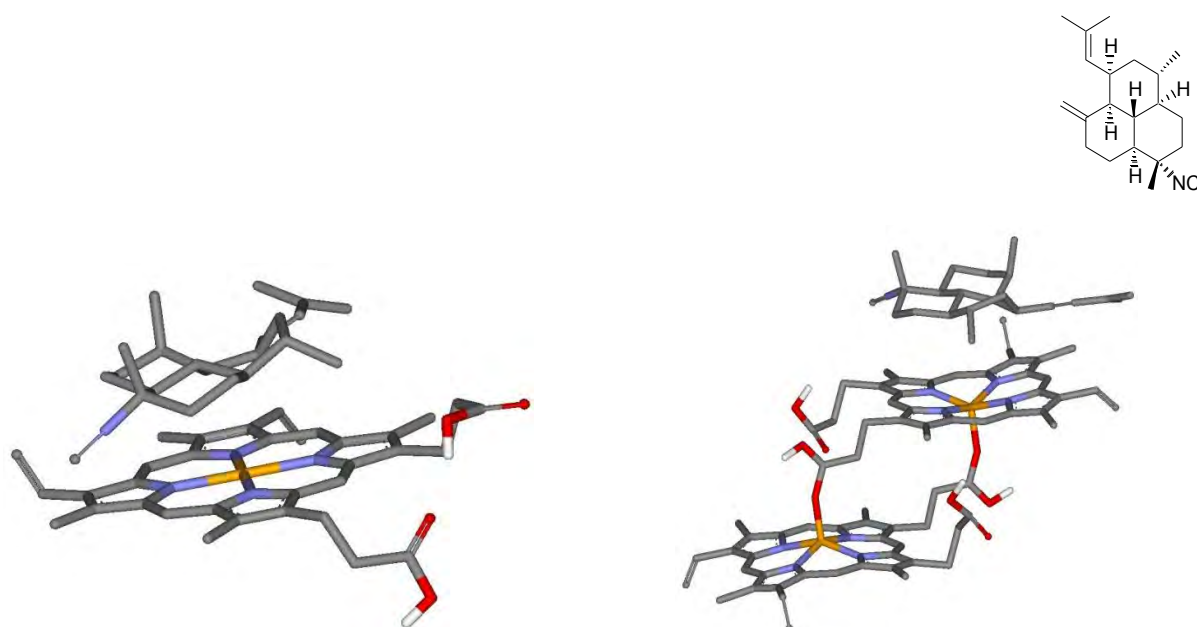


Figure 3.16: Lowest energy conformations for **1.41** docked against free heme via its carbon backbone (left) and via its hydroxyl functionality (right).

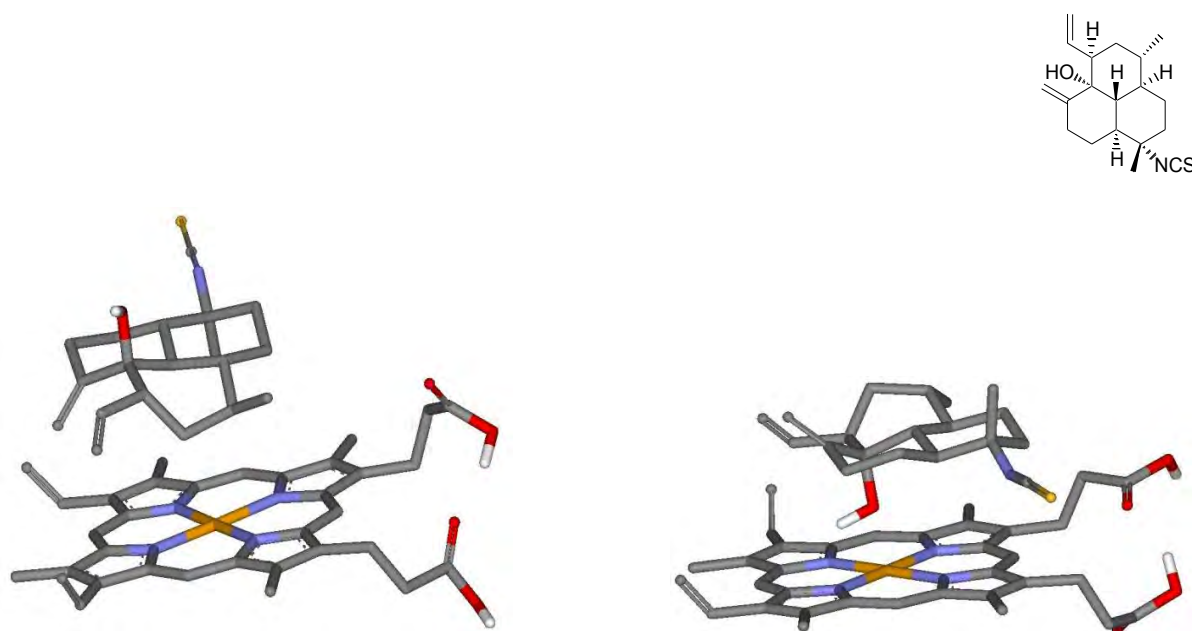


Figure 3.17: Lowest energy conformations for **1.42** docked against free heme (left) and the β -hematin dimer (right).

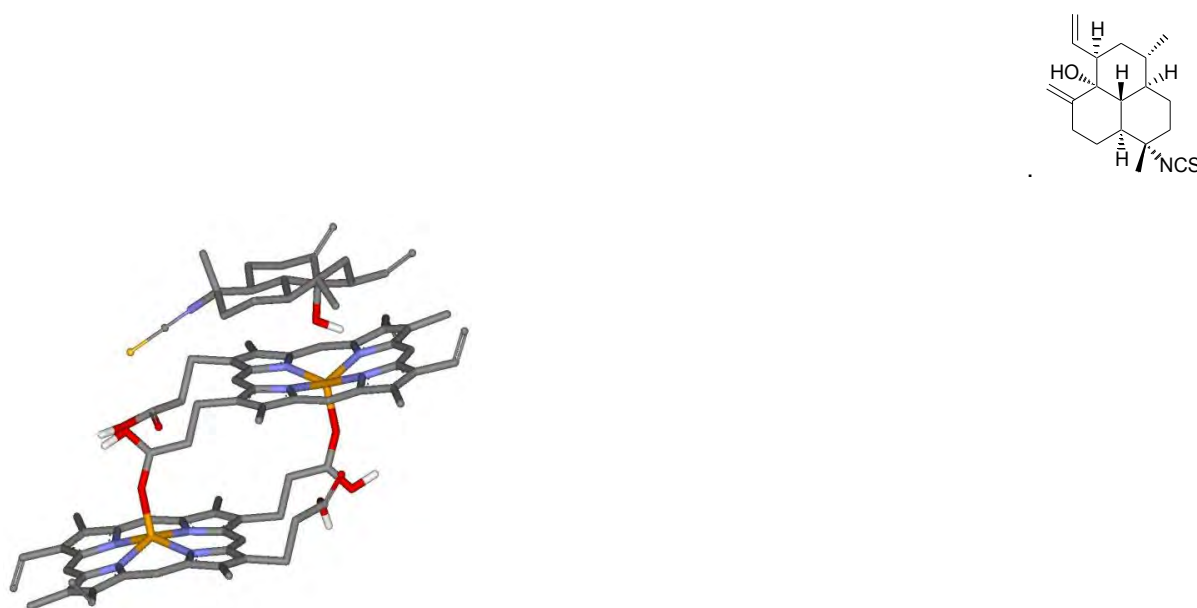


Figure 3.18: Lowest energy conformations for **1.42** docked against the β -hematin dimer

The majority of the marine compounds exhibit the same planar stacking behavior of CQ (**1.2**), with the carbon backbones aligning themselves with the porphyrin rings of both the heme receptors. In most cases the functional groups are directed away from the iron ring centers, with the exception being the hydroxyl group of structure **1.42** which in certain cases aligned itself with the ring center. These interactions agree with the electrostatic calculations performed in Chapter 2, with the positively charged carbon backbones aligning themselves with the negative porphyrin centers and the negative functionalities serving to orientate the molecules on their approach. Several of the structures (**1.30**, **1.39**, and **1.40**) also exhibited potential inhibition of lateral crystal growth by occupying the regions adjacent to the attached HD heme groups. This would be due to the relatively negative potentials of the inhibitor side chains interacting with the positive outer edges of the heme receptor rings. With the exception of structure **1.42**, none of the inhibitor molecules aligned themselves in such an orientation that would favour formal bond formation between the heteroatom functional groups and the iron centers on the receptors.

3.5 Summary

The two chief interactions that can be observed from these docking simulations are that the carbon molecular backbones are responsible for the attractive intermolecular interactions between the inhibitors and the heme receptors; and that the negative potentials of the heteroatom functionalities on these inhibitors have unfavorable, repulsive interactions with the receptors. Consequently, the inhibitory action of these molecules can be related to these two influences. The electrostatic attractions between the inhibitors' carbon frameworks and the heme surfaces allows for these molecules to occupy the binding positions that other heme molecules would use to propagate and form crystalline hemozoin.³⁵ Those marine compounds possessing similar flexible carbon tails/functional groups to the known inhibitor chloroquine have the ability to occupy not only the surface plane of the receptors, but are also capable of occupying the space lateral to these molecules and could potentially block heme approaches for both vertical and lateral crystal growth. The negative potentials possessed by the heteroatom functionalities on the inhibitors may exert a repulsive effect on incoming heme molecules, thereby discouraging their approach once the inhibitor has occupied

the binding site on the porphyrin ring. These results are in agreement with Wright *et al*'s pseudoreceptor models, in that the cyclic organic frameworks are critical to the interactions of these inhibitors with heme, as these frameworks are responsible for the positive electrostatic attractions which permit the molecules to bind to heme. The isonitrile functionality, whilst it may exert a repulsive effect post-binding, however is not an essential component for the molecules to bind to their heme receptors. Whether these groups are capable of forming formal bonds with heme should they adopt a less energetically favorable approach vector will be explored in Chapter 4.

INVESTIGATION OF INTER-MOLECULAR BOND FORMING OR BREAKING EVENTS

4.1 Semi-Empirical “Forced-Binding” Analyses

The simulated docking studies showed that the general trend for the group of compounds being investigated is for the molecules to align themselves parallel to the plane of the receptors through intermolecular electrostatics. Although this might be the most energetically favourable mode of molecular alignment, it does not rule out the possibility that other orientations may happen, albeit with much lower probability. These orientations may provide the necessary molecular orbital overlaps to form formal, intermolecular ligand-receptor bonds. To determine whether bonding would be possible, should the molecules approach the heme target along the correct vector to favour formal bonding, some “forced-binding” simulations were performed. These involved constructing complexes with the ligands bound to the iron centre of the heme porphyrin ring, breaking this bond and then performing energy minimizations on the system using semi-empirical methods.

4.1.1 Semi-empirical Methods

The least intensive of the *ab initio* methods are termed semi-empirical (SE) methods which follow the methodology of HF calculations but approximate or omit certain terms, e.g. the two-electron Hamiltonian integrals are often not explicitly included.⁶⁸ In order to correct for this, database parameterizations are used to account for such terms. This results in reduced computational time, though results may be very flawed if the atom types being evaluated are not adequately represented in the parameter database.⁶⁹ The most popular SE methods are the PM3 (Parameterized Method number 3)⁶⁸ and AM1¹⁰⁰ methods. Semi-empirical energy determinations are often used for their expediency as they are faster than DFT methods, yet still calculate electronic densities, thereby allowing for bond breaking/forming events to be simulated.

4.1.2 Energy Minimization Trajectories

Of the 18 runs, only 4 managed to achieve self-consistency. Upon analysis of the minimization trajectories, it was clear that the proximity of most of the functional groups of the marine models to the porphyrin centre caused extensive destabilization of the HP structure. These destabilizations in many cases lead to the iron atom actually leaving the ring to stabilize the system's energy. The most destabilizing functionality was the isonitrile group with none of the ligand-receptor complexes being able to achieve self-consistency. Both the isocyanate and the isothiocyanate groups were capable of forming reasonably stable bonded complexes with the iron centre in heme, with the isothiocyanate groups causing the least degree of ring destabilization. Examples of complexes of isocyanate, isothiocyanate and isonitrile inhibitors with the HP receptor are:

4.1.2.1 Isocyanates and Isothiocyanates

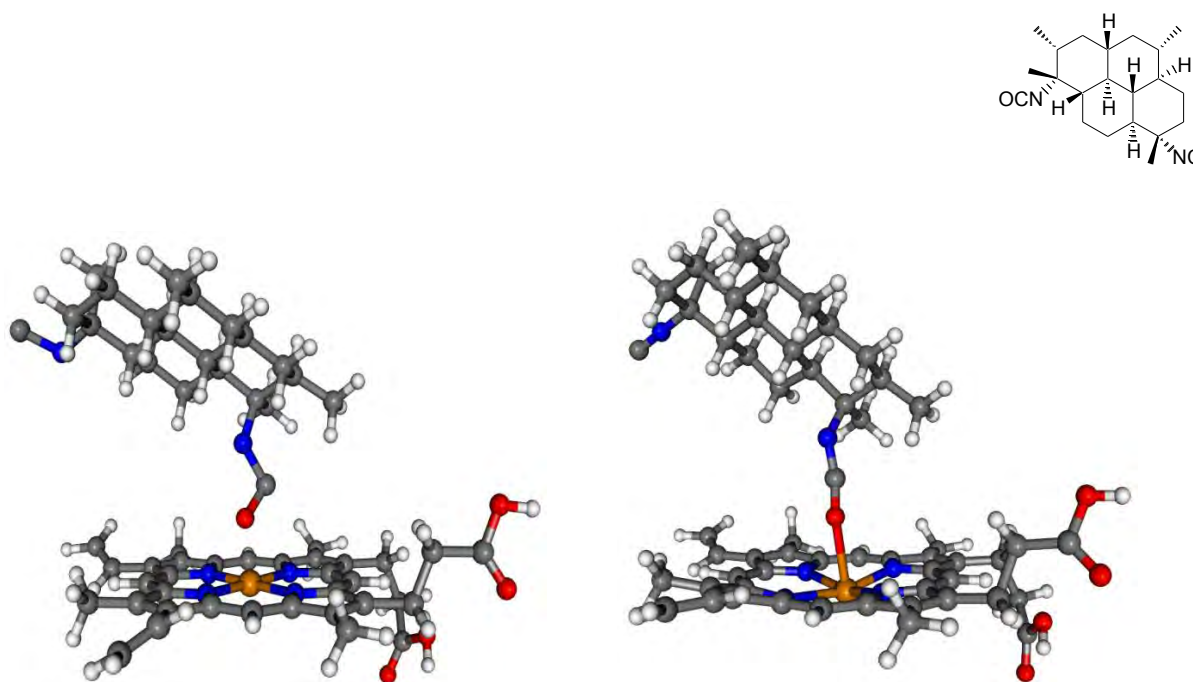


Figure 4.1: The initial (left) and AM1 optimized (right) configurations for isocyanate **1.33**.

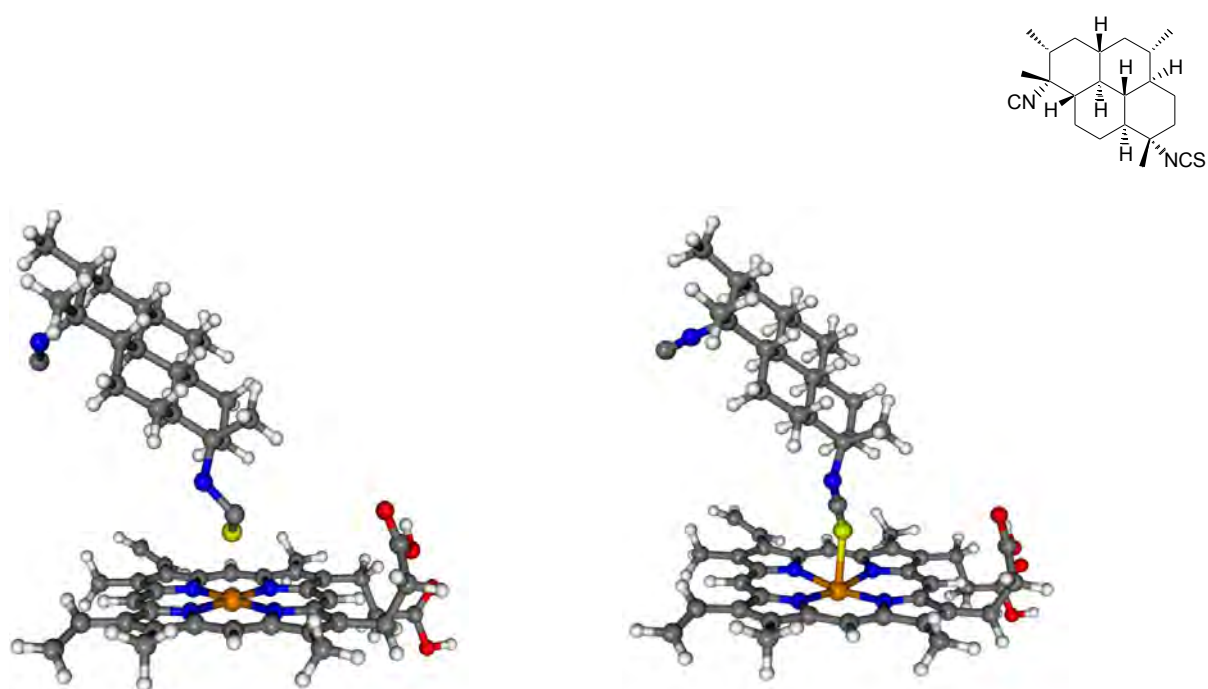


Figure 4.2: The initial (left) and AM1 optimized (right) configurations for isothiocyanate 1.31.

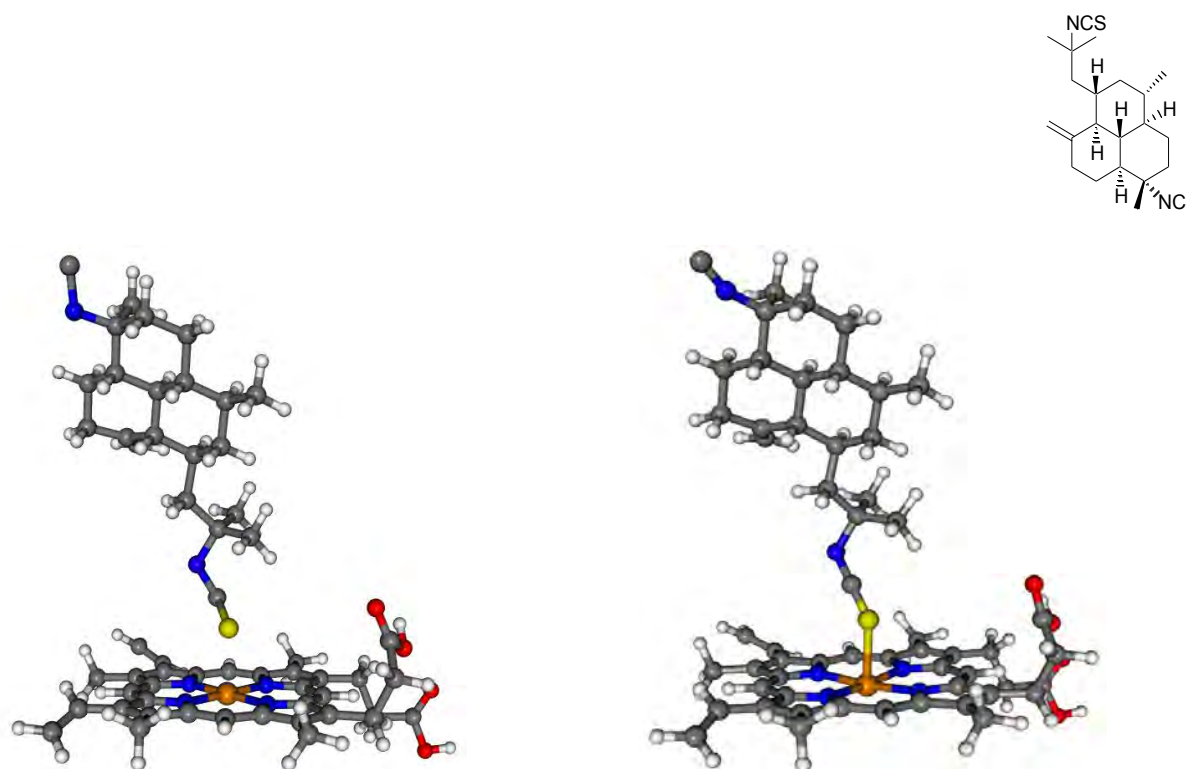


Figure 4.3: The initial (left) and AM1 optimized (right) configurations for isothiocyanate 1.39.

Figures 4.1 – 4.3 show how the isocyanate and isothiocyanate groups have the potential to form stable, formal bonds with the iron or the pyrrolic nitrogens in the heme receptors. This agrees with the predictions made in Chapter 2 on the basis of the shapes of the HOMO/LUMO molecular orbital shapes. Although the approach orientation necessary for bond formation might not be energetically favourable due to their electrostatic topologies, should the molecules approach in a suitable fashion then intermolecular bonding may in fact result. Comparatively, the isothiocyanate bonds put less strain on the ring, gauged by the lesser degree of nitrogen-iron bond angle deformation from their initial planar arrangement. The optimized isocyanate (**1.33**) shows an unsymmetrical depression of the porphyrin ring, with the iron atom being positioned out of the plane of ring to achieve a stable arrangement. The ambient energy required to maintain this unsymmetrical and strained arrangement will have to come from the environment in the case of a real system and so this arrangement, whilst theoretically possible, might not be feasible in nature.

4.1.2.2 Isonitriles

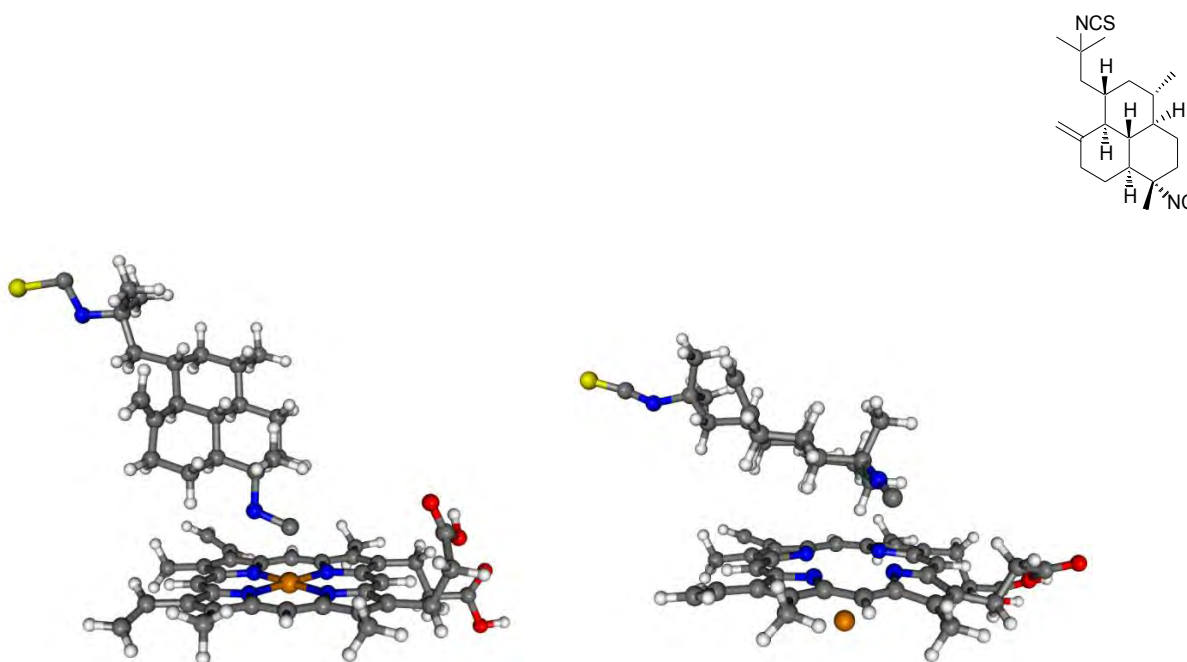


Figure 4.4: The initial (left) and AM1 minimized (right) configurations for isonitrile **1.39**.

Figure 4.4 illustrates the common behaviour of the ligand-heme system for the isonitrile groups upon minimization. The achievement of an energy minimum only occurs through deflection of the isonitrile group away from the ring and the ligand molecule's carbon backbone has begun to align itself with the FP molecular plane. The strain applied to the ring from the forced proximity of the two molecules results in the iron atom leaving the target molecule so as to reduce the applied stress. As was noted in Chapter 2, the isonitrile groups are not likely to interact in a stable manner with the porphyrin ring centre and are unlikely to be involved in an orbital overlap between the ligand molecule's HOMO orbital and the heme molecules' LUMOs. The inability of the isonitrile-FP complexes to achieve self-consistency in modelling raises some doubts as to the physical reality of such an interaction.

4.2 Molecular Dynamics

Although energy minimization trajectories provide some information about a particular system, they only concern themselves with the achievement of an energy minimum. In nature, whilst most systems will adopt their lowest energy conformations when possible, the abundance of energy in their surroundings will generally permit them to exist in a variety of arrangements, i.e. activation energy barriers can be surmounted. In order to explore these possible arrangements and the intermolecular interactions that are possible at higher energies, molecular dynamics methods are necessary.

In the modelling of chemical systems, there are two major groups of methodologies; static and dynamic. The key difference between these two approaches is that dynamic simulations hold the modelled systems at finite temperature, thereby allowing for certain degrees of atomic motion, whereas static systems do not. The advantage of the dynamics method is that a molecule's conformational space can be better explored at various ambient temperatures as certain rotation energy barriers may be overcome.¹⁰¹

Now a very basic *ab initio* molecular dynamics (AIMD) calculation will involve the integration of the nuclear motion equations and, at each time step, the forces exerted on the system will be computed from a minimization of the electronic energy at that particular nuclear arrangement. To ensure that the

Hamiltonian equation for the nuclei is properly conserved, the minimization must be carried out to a high level of accuracy and this is the part of any AIMD calculation that is most time consuming.⁶⁵ In order to reduce this computing time, the Car-Parrinello extended Lagrangian metadynamics approach is the most commonly used method in modern AIMD which has recently replaced matrix diagonalization techniques. It is used in conjunction with DFT energy calculations and involves the imbuing of the KS orbitals with fictitious time dependences at a finite temperature/kinetic energy, T_e . This temperature is much lower than the real nuclear temperature but still permits the orbitals to relax in response to nuclear motion. A set of Lagrangian multipliers is employed to maintain the orthonormality of the energy orbitals, and this allows for the calculating of the KS Hamiltonian eigenstates and for the achieving of wavefunction self-consistency to be computed simultaneously.^{74,75}

Due to there being a large number of potential combinations of different AIMD methodologies, it was necessary to select a specific combination and then to look at its various applications. For a method to accurately model the heme systems being explored, it would need to be capable of:

- Accounting for dynamical hydrogen bonding.
- Simulate intra-molecular interactions at a rigid surface.
- Successfully monitor reaction trajectories of potentially non-equilibratory states.
- Accurately model biologically active, organo-metallic complexes.

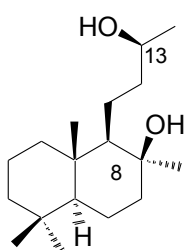
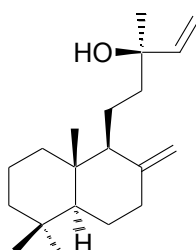
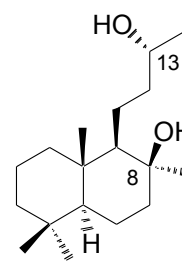
In the literature, the method of choice is the Carr-Parrinello Molecular Dynamics (CPMD) implementation of AIMD,¹⁰² incorporating the KS formulation of DFT and using the B3LYP gradient correction functional to compute the correlation energy term. This method has been show to meet all of the above mentioned requirements¹⁰³⁻¹⁰⁷ and shall be referred to as the „CPMD method’ in the text.

Due to the predictive nature of the CPMD method, it has the potential to draw attention to intermolecular events that may or may not happen in a physical system. This therefore requires an understanding of the details of the simulation to a degree that will allow for accurate discernment should unsuspected results be observed. Thus, before the CPMD method could be used to simulate the interactions occurring in the ligand-heme systems and to draw conclusions about these systems, its efficacy as an adequate *ab initio* dynamics method needed to be determined. The capabilities of the CPMD method were evaluated by using it to investigate the inter-molecular bonding responsible for the formation of a novel supra-molecular zipper that had been synthesized in our research group. The nature of the zipper's formation was investigated using a series of different established computational approaches and was then simulated using the CPMD method. This was done to see if the CPMD method could account for and agree with all the data of the other methods as a single yet efficient set of algorithms.

4.3 Application of an *Ab Initio* Molecular Dynamics Method to a Naturally Occurring Non-Oligomeric Molecular Zipper

4.3.1 Introduction

X-ray analysis of 14,15-bisnorlabdane-8b-13*R*-diol (**4.1**), prepared in a six-step synthesis from the commercially available diterpene (+)-manool (**4.2**), revealed a secondary structure comprising an infinite ribbon of hydrogen bonded molecules in which the C-8 and C-13 hydroxyl groups act as both hydrogen bond donors and acceptors (**Figure 4.5**), reminiscent of a supramolecular zipper.¹⁰⁸ Interestingly, the 13*S* epimers (**4.3**) could not be crystallized.

**4.1****4.2****4.3**

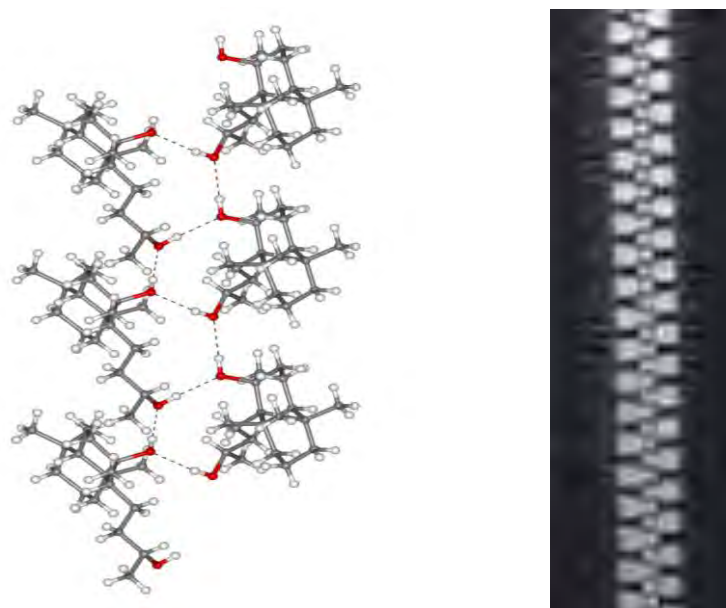


Figure 4.5: X-ray crystallography data showing the zipper network inherent in crystals of the (R) epimer (left). The hydrogen bonds act as the teeth in a normal zipper (right).

This arrangement is termed a non-oligomeric supramolecular zipper, in that the zipper “teeth” on either side of the zip are not connected to one other via a backbone structure as is the case in oligomeric zippers, e.g. DNA helices or in fact a normal zipper (**Figure 4.5**). Hydrogen bonds, because of their strength and directionality, are an ideal “adhesive” for the noncovalent assembly of molecular building blocks to form supramolecular zippers.¹⁰⁹ The formation of the supramolecular zipper from **4.1**, and its C-13 epimer (**4.3**), were studied *in vacuo* using various quantum mechanical and force field based techniques e.g. molecular mechanics, AM1 and DFT. Interestingly, self-assembly of the hydrogen-bonded secondary structure was only observed in **4.1**.

4.3.2 Thermodynamical Data

There is precedent in the literature for the use of AM1 and DFT (Keinan) computational algorithms in the simulation of non-oligomeric zippers.^{110,111} The mono-, di-, tri- and tetramers of **4.1** and **4.3** were optimized using each of the B3LYP/6-31G (d) and AM1 methods, along with a two layer hybrid of the two. This hybrid model is known as an ONIOM model and involved application of the high accuracy DFT (B3LYP) method to those atoms closest to and including the hydrogen bonding hydroxyl groups;

whilst the more expedient AM1 method was applied to the rest of the atoms in the system. The good agreement between models illustrated that the AM1 semi-empirical calculations were sufficient for this study. Association energies were calculated from the AM1 data,^{112,113} and indicate little difference between the (R) and (S) series:

Table 4.1: AM1 Thermochemical data (298K) for a polymeric series of the (R) and (S) epimers (kcal/mol)

	R				S			
n	1	2	3	4	1	2	3	4
ΔH_f	166.5	329.2	491.4	652	166	327.4	487.7	649.6
ΔG_f	121.2	251	377.9	509.3	121.3	250.5	380.8	509.5
Association Energies								
$\Delta H_f - \Delta H^\ddagger$	0	-3.7	-7.9	-13.8	0	-4.7	-10.4	-14.7

These activation energies were calculated by subtracting the enthalpy of formation of n monomers ($n \times \Delta H_f$ of the monomer) from the enthalpy of formation of the optimized n -meric systems. These energies indicate whether the polymeric systems increase or decrease in stability with an increase in the value of n . Interestingly, the (S) system exhibited remarkable stability with regards the formation of the trimeric form when compared to the (R) system and it may be the stability of this much smaller cluster that discourages zipper formation.

4.3.3 Steric Interferences and Energy Minimizations

Upon inspection of the generated (S) epimeric polymers, constructed by inverting the stereochemistry at C13 on the (R) system, it was observed that the methyl groups at the C13 centres were in sterically unfavourable proximities to the methyl groups at C8 on neighbouring molecules. The strain exerted on the zipper system by these interactions appeared to result in deformation of the zipper network and this could in turn disrupt the hydrogen bonding network holding the zipper together. These interactions are shown in the tetrameric (S) system in **Figure 4.6**.

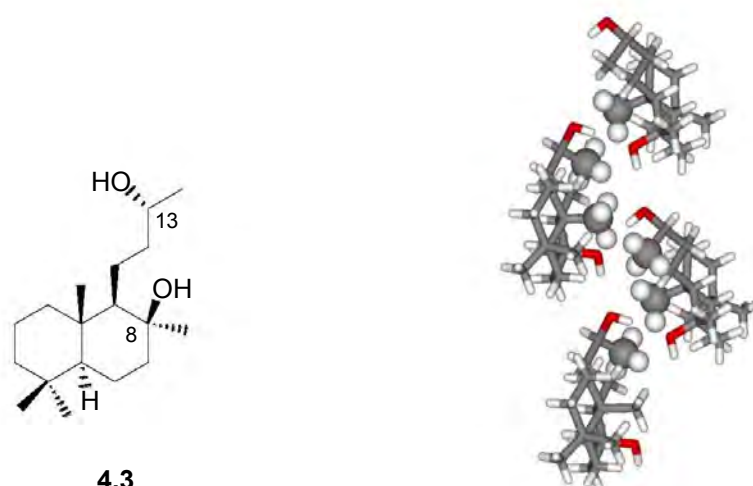


Figure 4.6: Enhancement of the sterically unfavourable proximities of methyl groups located at the C13 position of **4.3** on the (S) tetrameric system before energy minimization.

By visualizing the output trajectory of the subsequent energy minimization conducted on this system, it was observed that the monomers force themselves away from each other and lock together into a discontinuous non-linear network. This will achieve an alleviation of the steric strain applied by the unfavourable methyl proximities but will result in a breaking of the continuity of the zipper network as shown in **Figure 4.6**. This disruption of zipper integrity upon energy minimization is not observed in the (R) epimeric system.

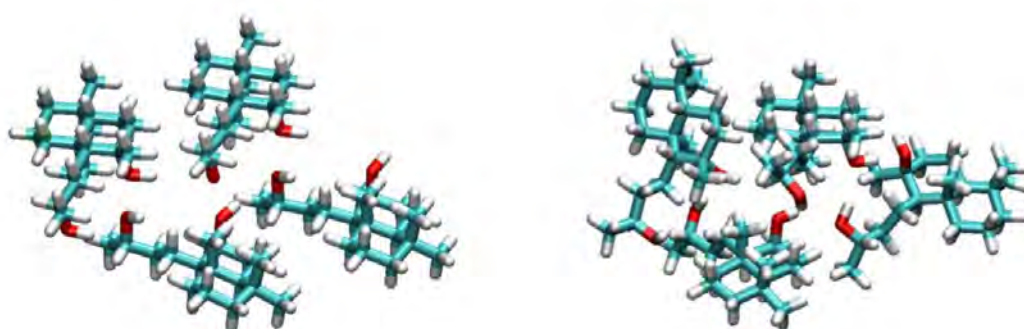


Figure 4.7: The starting (left) and AM1 optimized (right) arrangements of the (S) tetrameric system.

4.3.4 Differences in Hydrogen Bonding Between Polymeric (R) and (S) Systems

The integrity of the zipper structure is reliant on two bonding constructs. Firstly, the hydrogen bonds forming the central binding network within the super-structure must form a continual and stable network. Secondly, the 2° hydroxyl groups on the C13 carbons of the terminal zipper substituents must be made available for addition of subsequent monomers to extend the zip. In the optimized (R) system, the monomers comprising the super-structure all exhibit the correct spatial positions; and the complimentary hydroxyl groups at carbons 8 and 13 are well within hydrogen bonding distance. There is also a lack of hydrogen bonding potential at the terminal monomeric C13 positions, thereby permitting the sequestration of additional monomers into the growing zipper to extend the system. These networks can be seen in **Figure 4.7** and **Figure 4.8**.

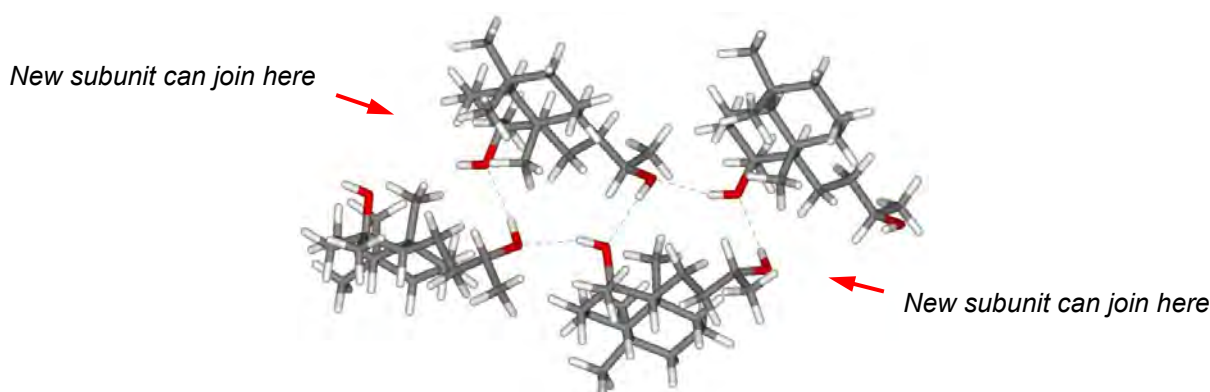


Figure 4.8: Proximity permitted hydrogen bonds (dotted blue lines) between hydroxyl groups on the minimized (R) tetrameric system.

In the case of the minimized (S) system, not only is the central network irregular but there is also the presence of a terminal bond that effectively „end-caps’ the network, thereby preventing the assimilation of more molecules into the zipper. This can be seen in **Figure 4.8** and suggests that the (S) epimer has a tendency to form small clusters of molecules rather than forming a zipper superstructure.

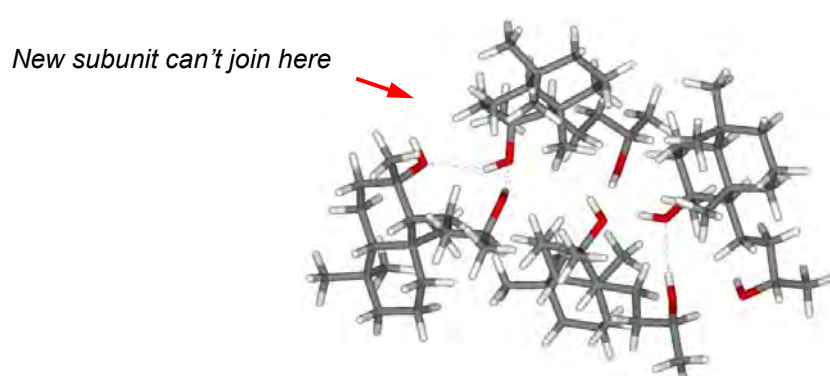


Figure 4.9: Proximity permitted hydrogen bonds (dotted blue lines) between hydroxyl groups on the minimized (S) tetrameric system.

4.3.5 Force Field Dynamics

The inter-atomic distances between the C10 and C13 hydroxyl groups were monitored for the tetrameric systems over steps of molecular mechanics dynamics and then plotted. This allowed for the stability of the hydrogen bonds to be observed over time. The distances monitored are shown below:

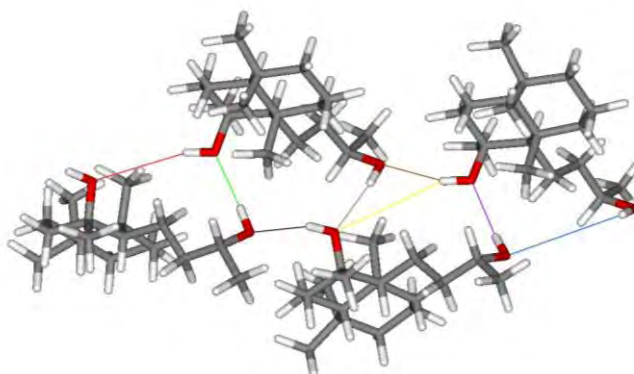
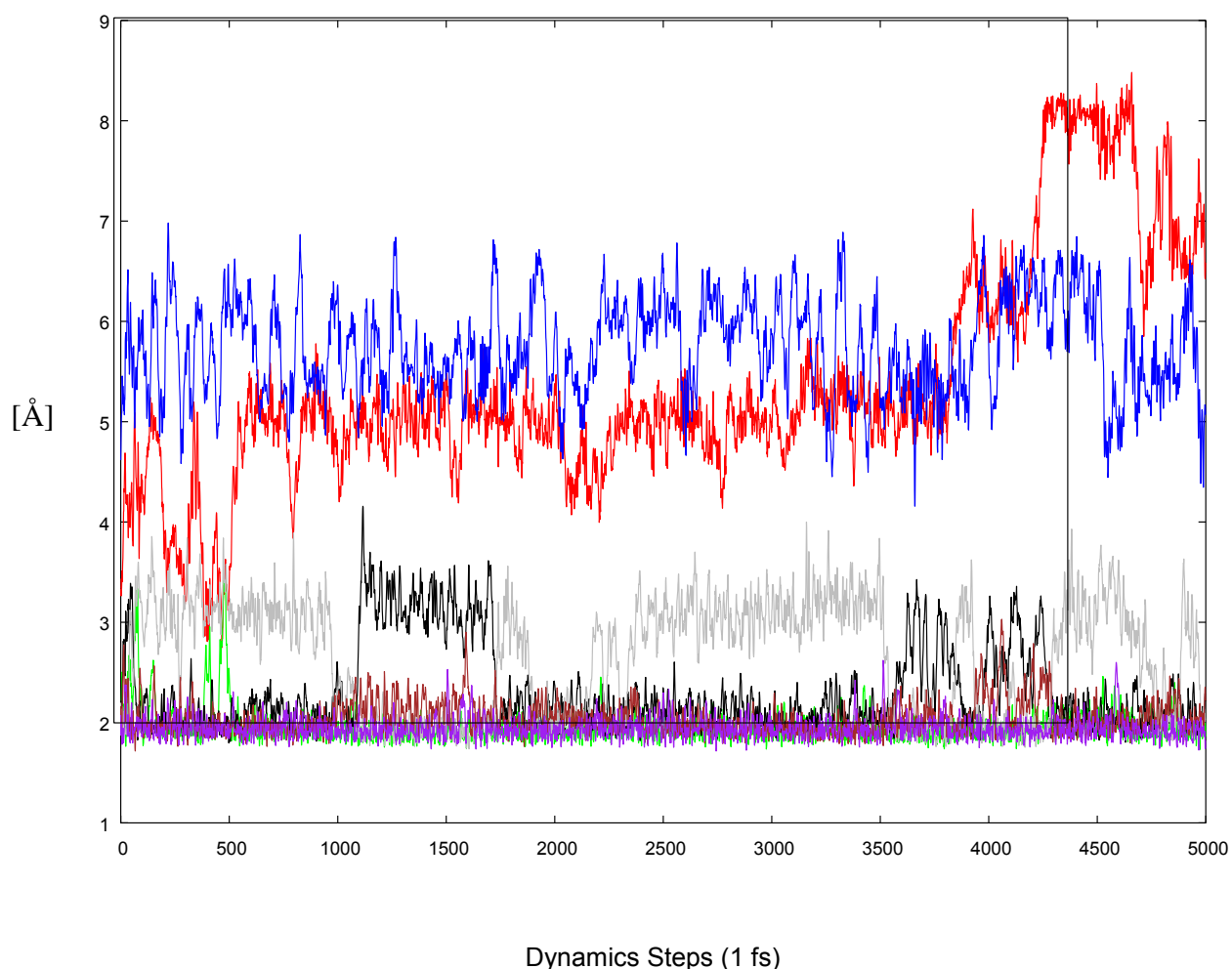


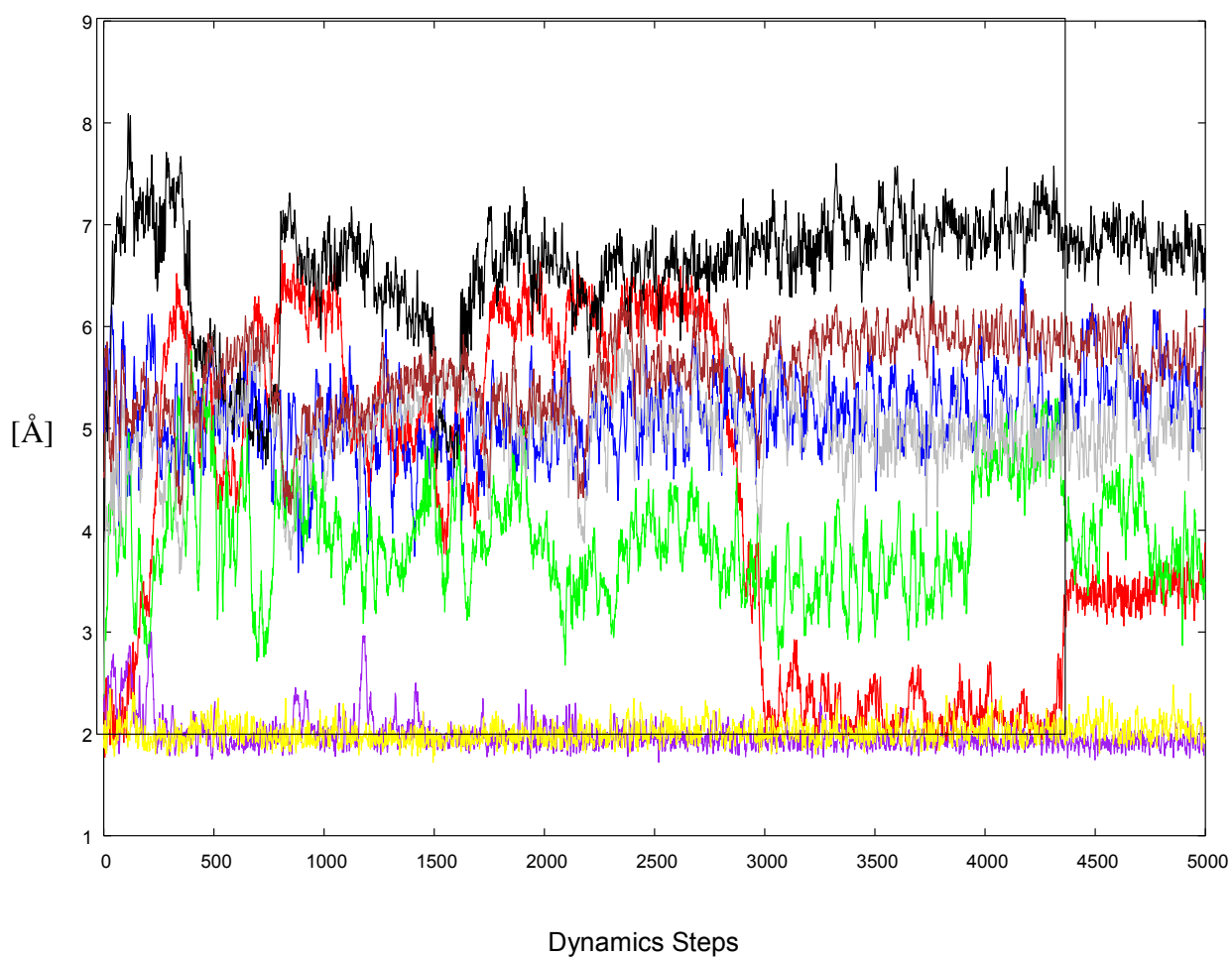
Figure 4.10: Interatomic distances monitored as a function of dynamical time. The (R) tetramer was used as a template for this figure and will not exhibit all of the hydrogen bonds illustrated here.

Graph 4.1 and **Graph 4.2** show the difference in hydrogen bond behaviour between the (S) and (R) systems at 300 K:



Graph 4.1: Plot of interatomic distance versus dynamical time for the (R) tetrameric system at 300 K.

The results illustrated in **Graph 4.1** show that the hydroxyl groups involved in the central bonding network remain within stable hydrogen bonding distance throughout the dynamical runs. This results in the zipper maintaining its integrity. The hydroxyl groups at the zipper ends, signified by the blue and red lines, tend to remain at a distance which does not permit hydrogen bonding. The 2° hydroxyl groups at these C13 positions are now made available for bonding to an incoming subunit, thereby permitting its assimilation and the extension of the zipper; in agreement with the energy minimization trajectory data (see **Figure 4.7**).



Graph 4.2: Plot of interatomic distance versus dynamical time for the (S) tetrameric system at 300 K.

In contrast to the bonding pattern seen in the (R) tetramer, the central bonding network of the (S) system breaks down upon the commencement of the dynamics, with only two of the inter-atomic distances remaining consistently with hydrogen bonding distance. Around dynamical step 3000, one of the terminal hydroxyl groups moves into hydrogen bonding distance (represented by the red line) suggesting the formation of the „end-capping’ bond mentioned in Section 4.3.4. Formation of this terminal bond would discourage the assimilation of additional subunits into the zipper, thus inhibiting its extension. This data is consistent with the energy minimization trajectory data (**Figure 4.8**).

4.3.6 Car-Parrinello Molecular Dynamics

4.3.6.1 The (R) System

In the (R) system, the zipper network is left intact throughout the simulations, with the hydrogen bonds remaining constant between the C10 and C13 hydroxyl functionalities. By extending the unit cell in two dimensions, the zipper superstructure can be seen to extend infinitely, allowing for crystal growth. The stability of the bonding network agreed with the molecular mechanics and energy minimization data from the previous computational analyses.

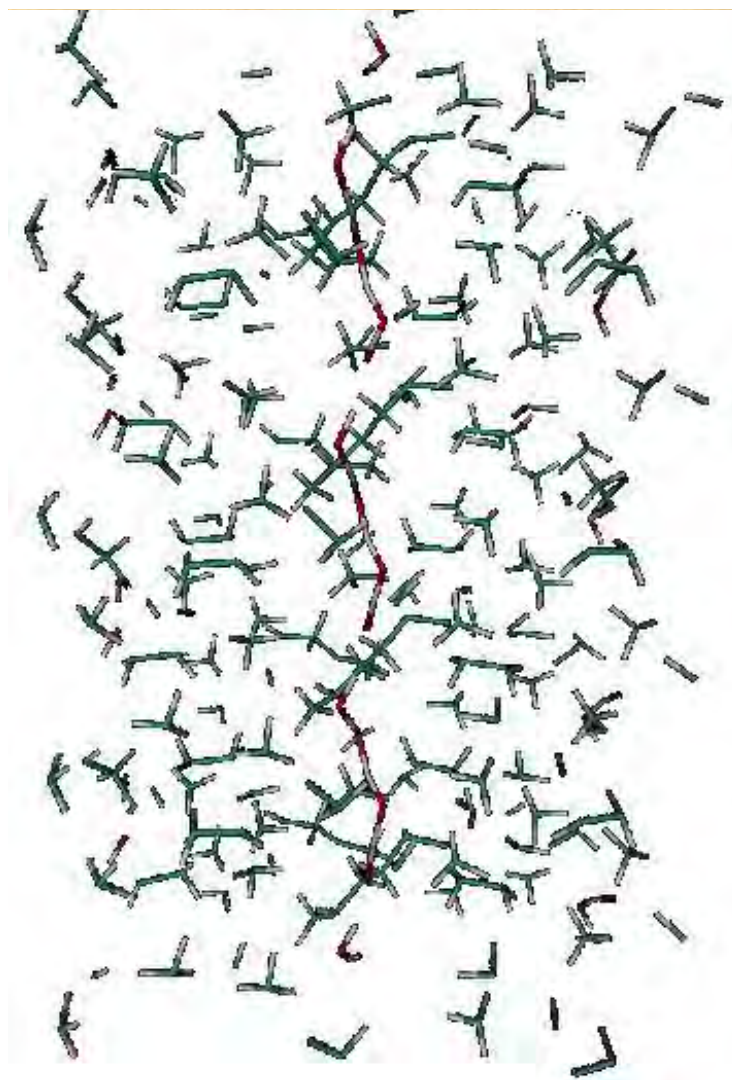


Figure 4.11: Extended zipper network formation, shown as red-white bonds along the central axis.

Interestingly, the dynamic runs showed evidence of potential proton transfer between hydrogen bonded hydroxyl moieties on adjacent monomers in the (R) system but not in the (S) system. This transfer appears to be unidirectional, with the proton moving either up or down the direction of the bonding network. The zip thus behaves as a proton „switch’,¹¹⁴ with single proton relay migrations occurring along the hydrogen bond network.

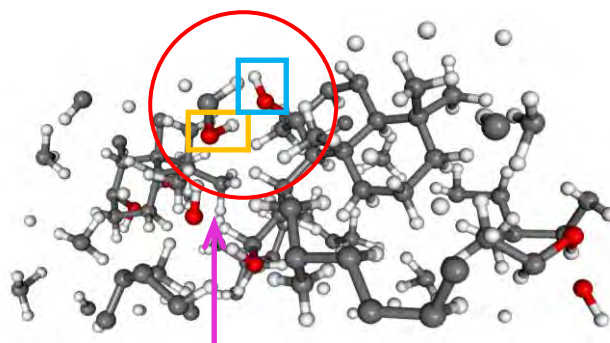


Figure 4.12: Stage one of transfer with hydrogen-oxygen bond at minimum extension. The proton donor is the lower of the two hydroxyl groups within the circle (orange rectangle), the acceptor is the higher (blue rectangle) and the arrow indicates direction of the zipper hydrogen bond network.



Figure 4.13: Stage two of transfer with the hydrogen-oxygen bond of the donor hydroxyl group (orange rectangle) extending towards the acceptor.

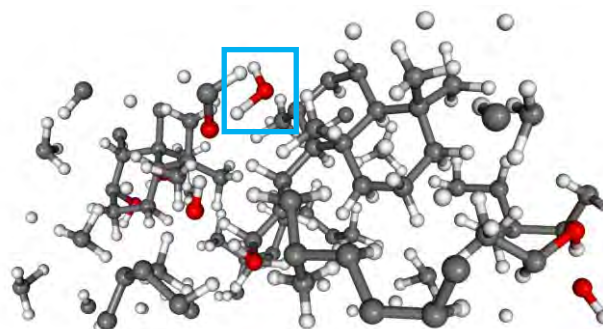


Figure 4.14: Stage three of transfer with the proton migrating from the donor hydroxyl group to the acceptor (blue rectangle).

4.3.6.2 The (S) System

In the (S) system, similar behaviour was observed as in the energy minimization runs wherein the zipper integrity is lost as the bulky methyl groups move apart to alleviate the excess steric strain on the system. A consequence of this strain is that the zipper breaks up into smaller micro-clusters rather than forming an extended network (**Figure 4.14**), in agreement with the data obtained from the molecular mechanics and energy minimization methods; and may provide an explanation as to why we were unable to crystallize the (S) epimer.

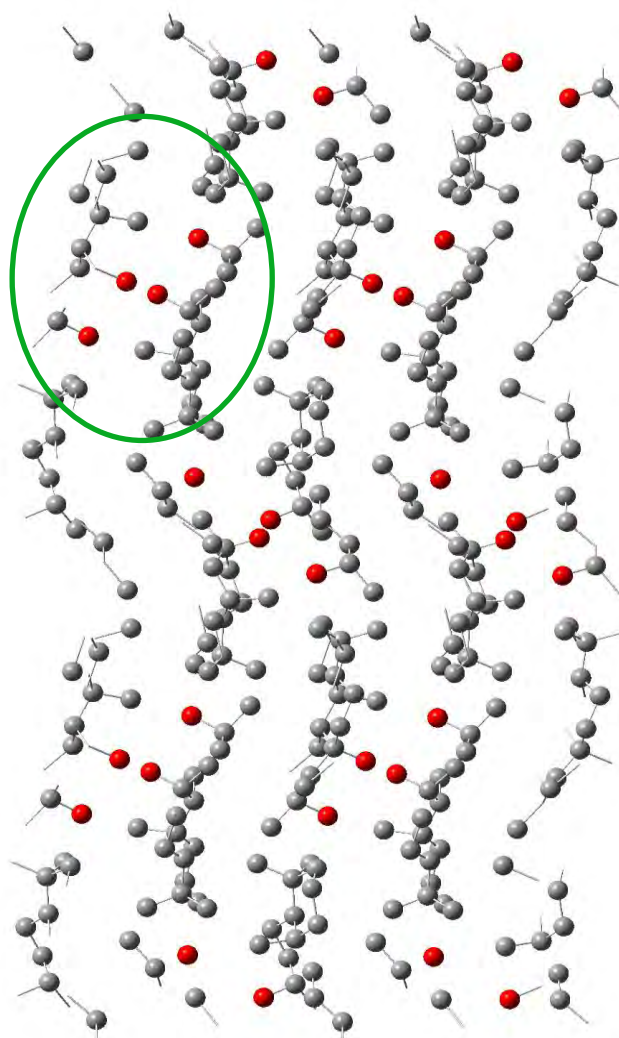


Figure 4.15: Disruption of zipper hydrogen bond network during finite temperature CPMD run (hydrogens not shown). The green circle indicates the hydrogen-bonded micro-clusters which compromise the formation of a linear (S) crystal network.

4.3.7 Summary

The information from the various computational analyses has shown that the difference in spatial arrangement of the two epimeric monomers translates into very different behaviour in polymeric systems. While the (R) system can maintain a stable and extensive hydrogen-bonded supramolecular network, the (S) system cannot, preferring to exist in smaller micro-clusters rather than a larger network. The stability of this zipper network in the (R) epimer's case may very well be responsible for its ability to exist as a crystalline solid whilst the (S) epimer proved difficult to crystallize.

4.4 Discussion of the CPMD Method's Efficacy

The CPMD method has shown itself to be capable of accurately describing dynamical molecular systems, providing valuable information around intermolecular interactions. It is able to incorporate the accuracy of density functional theory into dynamical analysis with the added ability to predict potential bond forming and breaking events. It was able to highlight the key structural differences between the two epimeric polymer systems and even suggest a potential proton transfer network within the (R) polymeric system, something which can now be investigated further in the laboratory. All this, coupled with its expedience, makes it an accurate, predictive and efficient simulation method that should provide valuable insights into the interactions occurring between the marine compounds (1.30 – 1.42) and their heme targets.

4.5 CPMD Simulations of Heme Systems

Those systems explored in section 4.1.2 were subjected to analysis using the CPMD method. The same starting configurations were used as initial arrangements for the unit cells undergoing dynamical simulation. Simulations of the inhibitor molecules interacting with the β -hematin dimer model were not performed due to the very long computational times required to achieve wavefunction convergences. As convergence of the molecular wavefunctions is required at each step of dynamics, this would have

only permitted a few steps of the dynamical trajectory to be computed and the results would not have been meaningful enough to draw accurate conclusions.

4.5.1 The Isocyanate and Isothiocyanate Systems

The CPMD runs confirmed the stability of the FP-isocyanate and FP-isothiocyanate complexes. The intermolecular bonds remained intact throughout all 3000 steps of dynamics, without any serious deformation of the porphyrin ring's symmetry. The starting and final configurations are shown below:

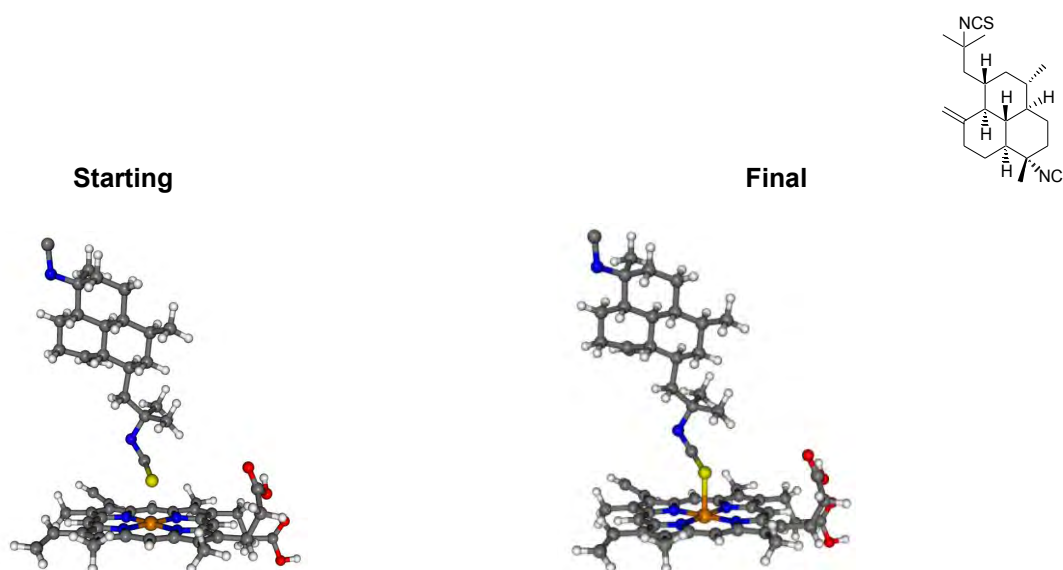


Figure 4.16: Starting arrangement (left) and the system after after 3000 steps of CPMD dynamics for the isothiocyanate (1.39) – FP system.

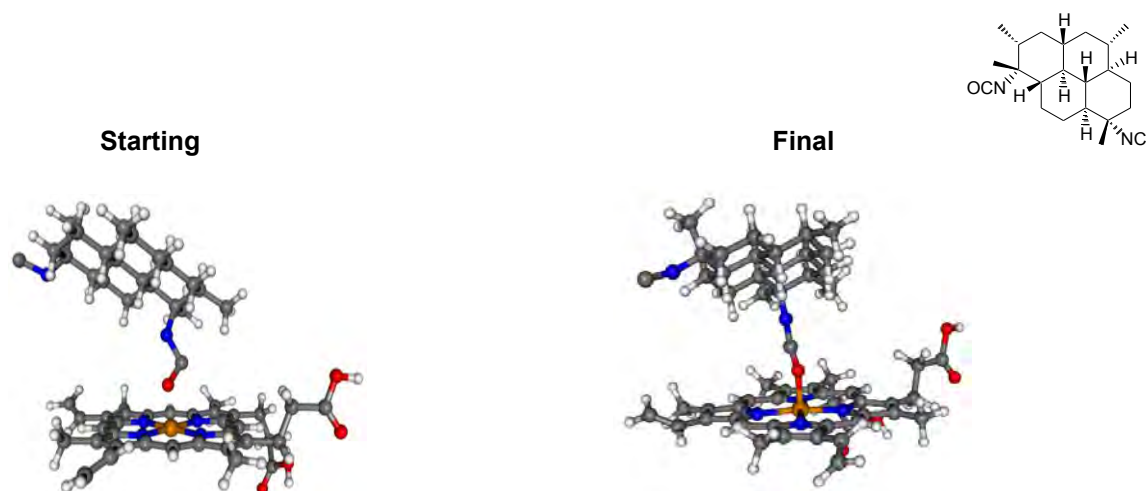


Figure 4.17: Starting arrangement (left) and the system after after 3000 steps of CPMD dynamics for the isocyanate (1.33) – FP system.

The figures above show the formation of stable bonds between the functional groups and the iron atom at the porphyrin ring centre. This is in agreement with the bonding orbital analysis (Section 2.3.2) which showed that the shape and parity of the HOMO and LUMO orbitals on the isocyanate and isothiocyanate functionalities could present a suitable match for those of the free heme receptor (Section 2.4.2). It also agrees with the *ab initio* forced binding (Section 4.1.2) simulations which suggested that intermolecular bonding could occur should there be sufficient ambient energy (activation energy) for bond formation.

4.5.2 The Isonitrile System

The CPMD runs confirmed the results from the forced binding simulation (section 4.1.2) with the isonitrile – FP bond breaking within 563 steps of dynamics.

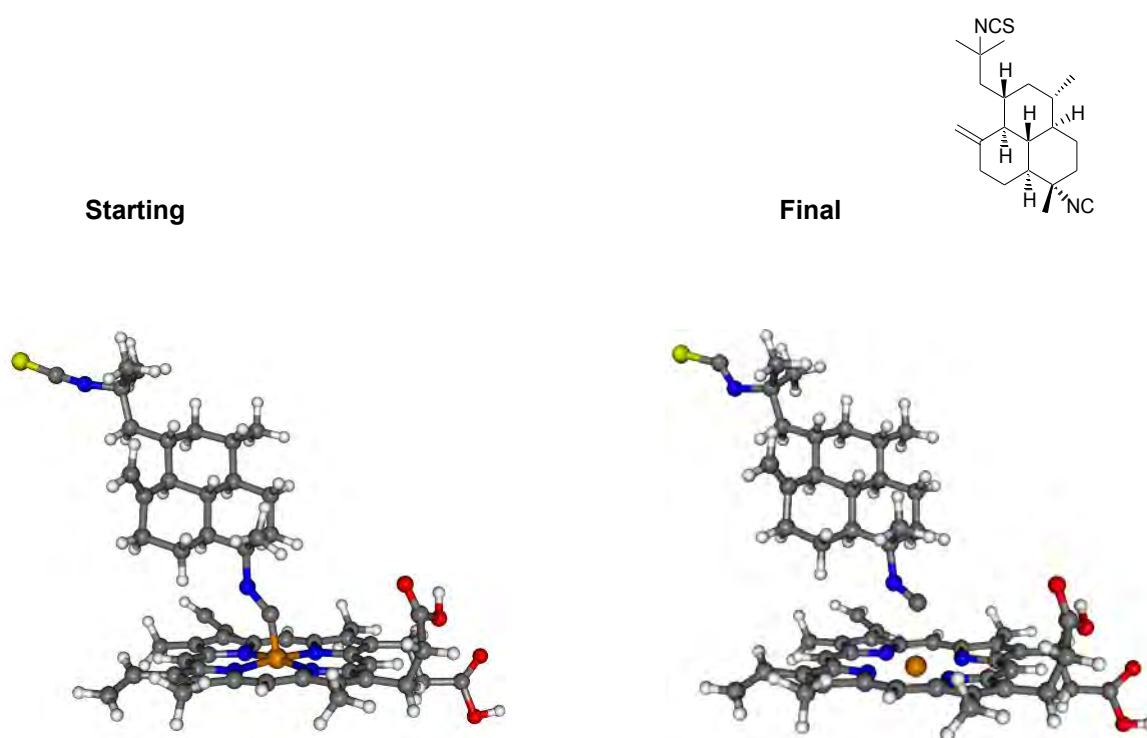


Figure 4.18: Starting and final (563rd dynamical frame) configurations for CPMD dynamics run on the isothiocyanate (1.39) – FP system.

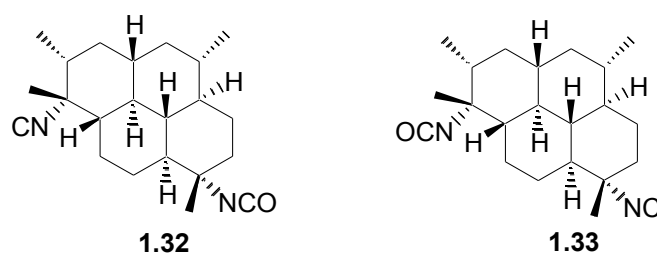
The figures above show that the isonitrile – iron atom bond, whilst initially possible, is not stable enough to withstand the dynamical shifting of the system and breaks very early into the simulation. The bonding orbital analysis (Section 2.3.2) suggested that the ideal orbitals for intermolecular bonding are not situated on the isonitrile functionality. Thus, whilst the CPMD method suggests that an isonitrile – iron bond is possible, it is a very weak bond and will most likely only occur in occasional, isolated instances. The apparent instability of the isonitrile – iron bond is puzzling since isonitriles are regarded as strong σ -donors (better than CO) and are also capable of extensive back-acceptance of π -electrons from metals in low oxidation states.

4.6 What Is the Computational Evidence Telling Us?

The data obtained during the CPMD simulations represented the final piece of data comprising the computational evaluation of the marine compounds, their receptors (FP and HD) and their intermolecular interactions. The conclusions that can be drawn from the data of Chapters 2 – 4 are:

- The isocyanate and isothiocyanate functional groups on the marine compounds are much better suited to forming intermolecular bonds with the central iron atom in heme receptors, should sufficient energy be available to the system, than isonitrile groups; and that these bonds are more stable under constant temperature dynamical simulations.
- When in proximity to the heme receptors, the marine isonitriles, isocyanates and isothiocyanates prefer to interact electrostatically along their carbon molecular framework, with functional groups orientated away from the porphyrin ring centres, rather than forming intermolecular bonds.

Looking at the IC_{50} values determined by Wright *et al*, for these compounds, the compound with the lowest IC_{50} value is **1.33** (9.4 nM) and contains isonitrile and isocyanate groups. A very similar structure (**1.32**), which only differs from **1.33** in that the locations of these functionalities have been reversed, has an IC_{50} of 219.96 nM, a 23.4 fold decrease in efficacy.



The computational analyses have shown that the isocyanate groups are capable of forming stable intermolecular bonds with their heme targets and that these two molecules possess similar electrostatic potentials as shown in **Figure 4.18**.

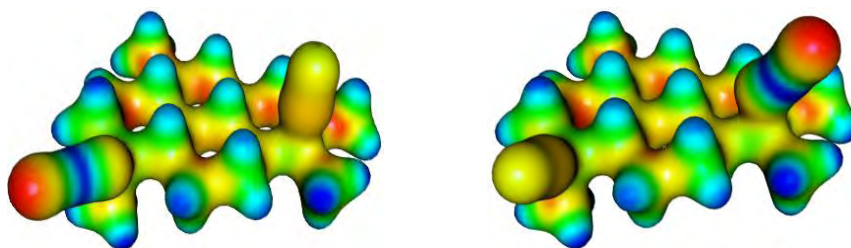
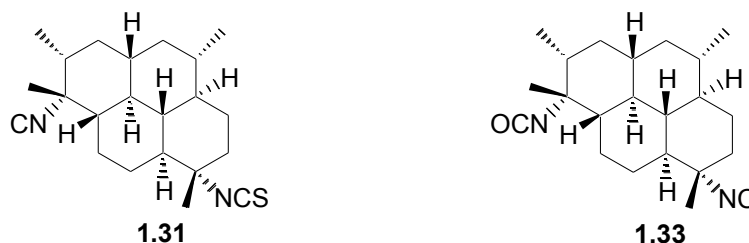


Figure 4.19: The very similar electrostatic potentials of structures **1.32** (left) and **1.33** (right).

These compounds however exhibit very different experimental IC_{50} values; a trend which can also be seen in the 13 fold decrease in inhibition efficacy between **1.33** and the isothiocyanate containing **1.31**.



The computational analyses have suggested that the isothiocyanate functionality is capable of forming the most stable bonds with the heme models' iron atom out of the isonitrile, isocyanate and

isothiocyanate functionalities, yet there is still a reduction in IC_{50} as a result of the structural differences between **1.31** and **1.33**.

In a biological context, a single change in the three dimensional arrangement of a compound can have a profound effect on its activity against chiral targets, e.g. proteins. The heme receptor molecules, however, are achiral in nature and their porphyrin rings would be open to approach by the marine compounds from any direction. Consequently, subtle changes in the structural geometry of compounds exerting their inhibitory capacity through the establishment of intermolecular bonds with the heme targets should not have such a significant effect on experimental IC_{50} values. This suggests that the inhibitory action of these compounds is not solely dependent on their ability to bind themselves to heme because if it was, compounds **1.31** and **1.32** would theoretically be more biologically active than **1.33**. It is important to note though that when the isonitrile group is not present in a compound, its biological activity is greatly compromised, e.g. **1.30** with a lone isothiocyanate functionality has an IC_{50} of greater than 30160, whilst **1.31** with both isonitrile and isocyanate functionalities has an IC_{50} of 126.

Another factor must therefore be involved that results in isonitrile-containing compounds having an increased biological potency when compared to the other marine compounds. It could be that the isonitrile functionality, along with the specific three-dimensional arrangement of the compounds containing it, allows for interaction with stereochemically and/or isonitrile specific receptor proteins, or other such structures, on the route to the site of inhibitory action in the food vacuole. This would mean that the isonitrile groups, whilst not being better heme-binding functionalities, enable a molecule to enter the malarial food vacuole more effectively than the other marine compounds and then exert its inhibitory action through the intermolecular electrostatic interactions explored in Chapter 3. This 'bond-less' binding mechanism has been proposed as the means by which the aminoquinoline family of compounds inhibits plasmodial proliferation.¹¹⁵

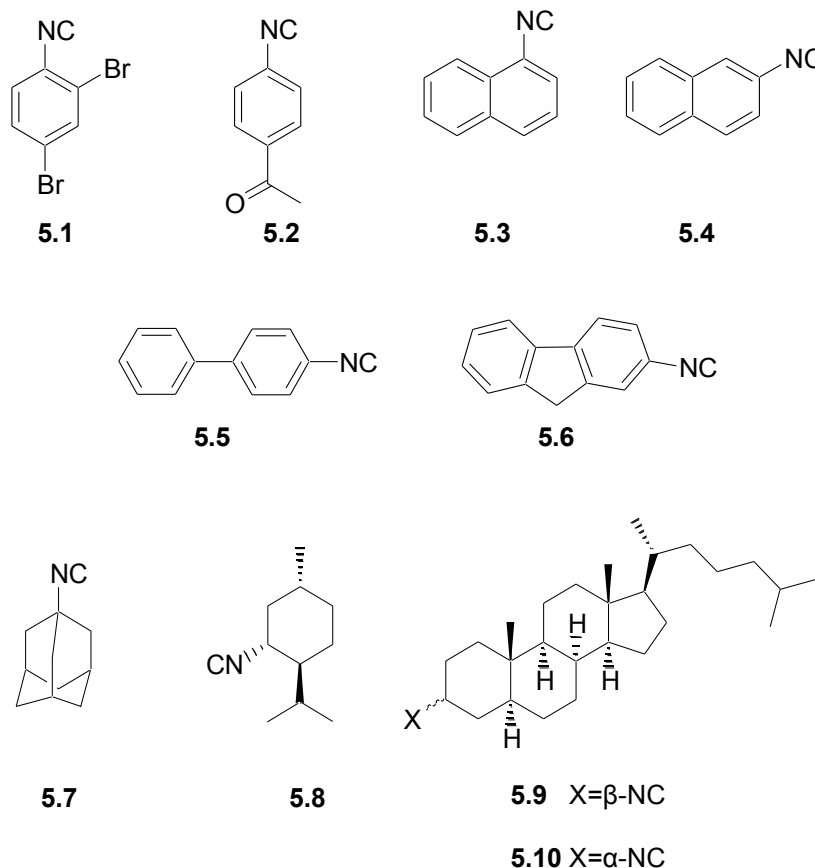
4.7 The Validity of Wright *et al*'s Pseudoreceptor Model

Wright *et al*'s pseudoreceptor model was constructed through building a surface around a superimposition of models of **1.30** – **1.42** and then weighting each model's influence on the overall receptor according to its IC₅₀ value. They then concluded that compounds which fitted this receptor would be effective at binding heme targets through intermolecular interactions. The computational analyses conducted in Chapters 2 – 4 refute Wright *et al*'s heme binding hypothesis; however they do not question the validity of the pharmacophore model proposed by Wright *et al*, derived from their pseudoreceptor, for design of novel anti-malarial isonitriles. The binding studies performed in Chapter 3 suggest that the marine compounds interact with the heme targets in a similar fashion to the known inhibitor chloroquine and that analogues of these compounds may indeed function as effective inhibitors of heme detoxification by *P. falciparum*. Whilst theoretical studies strongly suggest that the isonitrile group does not form strong intermolecular bonds with the heme structures in the parasitic food vacuole, its biological significance is not in question. We therefore proposed that a greatly simplified bi- or tricyclic compound possessing a tertiary isonitrile functionality may be as active as the marine isonitrile compounds studied by Wright *et al*.

SYNTHESIS OF MARINE ANTI-MALARIAL ISONITRILE ANALOGUES

5.1 Introduction

Publication of the anti-malarial activities of the marine compounds isolated by Köning and Wright⁶⁴ and then tested by Wright *et al*³⁰ drew due attention in the literature, and several research groups began to attempt the synthesis of, in most cases, simple analogues of these compounds. Of particular interest to the research detailed in this thesis are the synthetic analogues constructed by Singh *et al* (5.1 – 5.10)³ and Schwarz and co-workers (5.11 and 5.12),⁶ all of which were assessed for their *in vitro* anti-malarial activities against *P. falciparum*.



Whilst all of the synthesized isonitriles were found to inhibit plasmodial growth to some degree, **5.7** (1-isocyanoadamantane) was the most active (**Table 5.1**). Interestingly, **5.7** was also the only tertiary

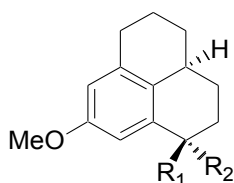
isonitrile in the cohort of synthetic isonitriles, with its antiplasmodial activity being an order of magnitude less than chloroquine.

Table 5.1: *In vitro* anti-malarial activity of isonitriles **5.1 – 5.10** against *P. falciparum* (strain **NF - 45**)³

Compound	IC ₅₀ ^a (µg/mL)
5.1	50.00
5.2	2.00
5.3	50.00
5.4	50.0
5.5	1.00
5.6	2.00
5.7	0.40
5.8	50.00
5.9	>50.00
5.10	>50.00
Artemisinin	0.03
Chloroquine	0.04

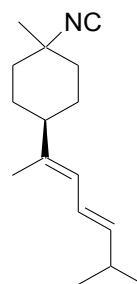
^a 50.00 µg/mL was the highest concentration used in the study.

Similar tricyclic structural analogues of Köning and Wright's anti-malarial marine diterpene isonitriles, were found to exhibit similarly potent activity against *P. falciparum* proliferation in a study by Schwarz *et al.*⁶



5.11 R1 = Me, R2 = NC (55%)

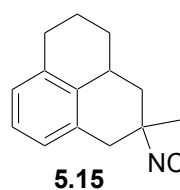
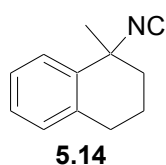
5.12 R1 = NC, R2 = Me (72%)

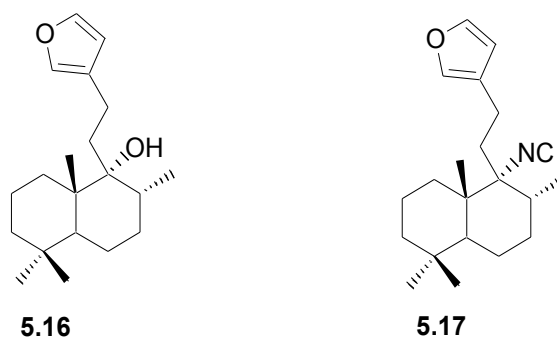


5.13

When tested against two different strains of *P. falciparum*, **5.11** and **5.12** were found to be effective anti-plasmodial agents (IC_{50} 0.10 and 0.17 $\mu\text{g/mL}$ respectively) against strain **NF – 45**; while the corresponding nitrile compounds were virtually inactive. The studies of Singh and Schwarz highlighted the increased anti-plasmodial activity of tertiary isonitriles over their secondary equivalents.

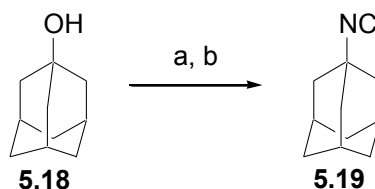
One of the references cited by Schwarz *et al*, a synthetic study by Kitano *et al*, reported a very interesting reaction for the conversion of tertiary alcohols to isonitriles.¹¹⁶ Kitano *et al* subsequently developed an improved method for the conversion of tertiary alcohols to isonitriles during their investigations of the antifouling capabilities of the analogues of the marine sesquiterpene 3-isocyantheonellin (**5.13**). The modified Kitano procedure was not available to Schwarz *et al* when they attempted the synthesis of **5.11** and **5.12**. This newly proposed method for isonitrile synthesis involved the reaction of a tertiary alcohol with trimethylsilyl cyanide (TMSCN) in the presence of a silver salt (AgX).¹¹⁷ We were intrigued by this reaction and were surprised that it had not found wider acceptance given the plethora of naturally occurring tertiary alcohols. The major focus of our synthesis now became the exploration of the general applicability of Kitano *et al*'s method for the conversion of tertiary alcohols to isonitriles. A variety of synthetic tertiary alcohols can be obtained through nucleophilic alkylation of carbonyl centres via standard Grignard or organo-lithium procedures. Consequently, we endeavoured to investigate Kitano *et al*'s reaction by first attempting the synthesis of bicyclic isonitrile (**5.14**) so as to familiarize ourselves with the reaction procedure and to modify the reaction procedure where/if necessary. Once the successful conversion of a tertiary alcohol to a tertiary isonitrile had been achieved we envisaged the synthesis of tricyclic isonitriles (analogous to **5.15**) in tandem with the conversion of some of the plethora of plant tertiary alcohol natural products in our laboratory's collection, e.g. hispanalone (**5.16**) into its isonitrile derivative (**5.17**). The efficient conversion of tertiary alcohols to isonitriles would thus provide entry to a library of synthetic tertiary isonitriles for testing against *P. falciparum*.





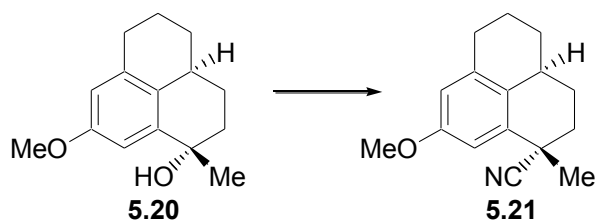
5.2 Kitano *et al*'s Synthesis of Isonitriles

The first paper published by Kitano *et al* proposing a procedure for the direct conversion of alcohols to isonitriles, i.e. the one cited by Schwarz *et al*, provided the details for the reaction presented in **Scheme 5.1**. Interestingly, this was the same isonitrile synthesized by Singh *et al* (**5.7**) using different methodology.³

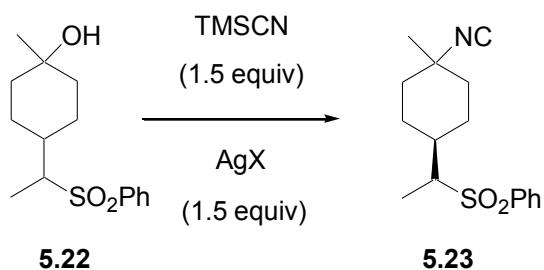


Scheme 5.1: Kitano *et al*'s first procedure for the conversion of a tertiary alcohol (**5.18**) to an isonitrile (**5.19**). (a) TMSCN, ZnX₂, DCM; (b) TBAF.¹¹⁶

This reaction involved the treatment of the adamantyl alcohol (**5.18**) with zinc reagents (ZnI₂, ZnBr₂, or ZnCl₂) and TMSCN in dichloromethane (DCM) followed by desilylation with tetrabutylammonium fluoride (TBAF) to produce the isonitrile (**5.19**) in yields ranging from 68% to 95% (depending on the zinc reagent used). Although Schwartz *et al* did attempt to use this method for the interconversion of tricyclic tertiary alcohol **5.20** into the corresponding isonitrile, the reaction repeatedly produced the nitrile (**5.21**), with no evidence of the isonitrile.

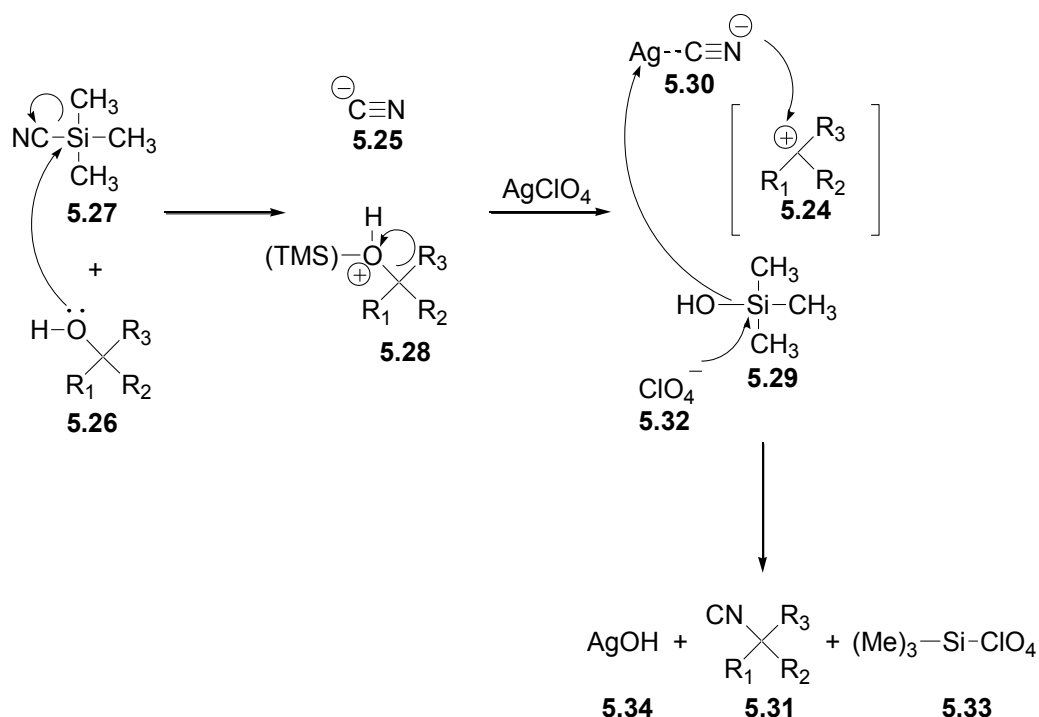


Consequently, we decided not to use Kitano *et al*'s first conversion method (**Scheme 5.1**) and instead focused on their modified method, involving the reaction of the alcohol with TMSCN in the presence of a silver salt (**Scheme 5.2**).



Scheme 5.2: Kitano *et al*'s modified procedure for the conversion of a tertiary alcohol (**5.22**) to an isonitrile (**5.23**).¹¹⁷

Kitano *et al* did not publish a mechanism for this reaction and so we have proposed the putative mechanism presented in **Scheme 5.3**.



Scheme 5.3: Proposed mechanism for the conversion of a tertiary alcohol (5.26) to the corresponding isonitrile (5.31) via Kitano *et al.*'s procedure.

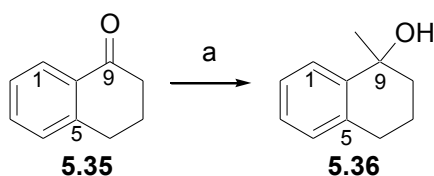
The mechanism proposed in **Scheme 5.3** is based on a classic S_N1 nucleophilic substitution reaction that proceeds via a carbocation intermediate (5.24). In an S_N1 mechanism the nucleophile attacks a carbocation, which is a hard acid according to hard/soft acid-base theory,¹¹⁸ whilst in an S_N2 mechanism the nucleophile attacks the carbon atom of a molecule which is a softer acid. The more electronegative atom in an ambident nucleophile is a harder base than the more electropositive atom and so, if the cyanide ion favours N attack (necessary to produce the isonitrile functionality), the reaction character then becomes more S_N1 in nature. The cyanide ion (5.25), despite its ambident character, favours alkylation at the carbon; however, should the ion be „complexed’ with a heavy metal counter-ion such as silver, alkylation occurs preferentially at the nitrogen. This harder mode of attack, coupled with an aprotic solvent (DCM) which will not cause hydrogen bonds that would hinder attack with the nitrogen atom, will result in the insertion of the isonitrile functionality to occur via an S_N1 mechanism. In step one, the hydroxyl proton on the tertiary alcohol (5.26) is replaced by the trimethylsilyl group (TMS) from TMS-CN (5.27) to form a trimethyl-silate (TMSO) group on 5.28, whilst the cyanide ion (5.25) dissociates into solution. In step two, the TMSO leaving group breaks away

from **5.28** to produce the carbocation intermediate (**5.24**), while collecting the proton which was replaced in step one to form trimethyl-silanol (TMSOH, **5.29**). In the third step, the addition of the silver perchlorate salt (AgClO_4) provides Ag^+ as the heavy atom counter-ion for the cyanide ion (**5.30**), thereby facilitating nucleophilic attack with the nitrogen atom to afford **5.31**. The perchlorate ion (ClO_4^- **5.32**) then replaces the hydroxyl group on TMSOH to form $(\text{Me})_3\text{SiClO}_4$ (**5.33**) and the free hydroxyl is then picked up by the Ag^+ ion (previously complexed with the cyanide ion) to form silver (I) hydroxide (AgOH , **5.34**) as a white precipitate.¹¹⁸⁻¹²⁰

5.3 Synthesis of Bicyclic Isonitrile

5.3.1 Methylation of α -Tetralone

α -Tetralone (**5.35**), a commercially available bicyclic ketone, was alkylated with MeLi according to standard procedures (**Scheme 5.4**) to afford the tertiary alcohol **5.36** in a yield of 93%.¹²¹ Purification of the product was achieved by re-crystallization from hexane and ^{13}C NMR analysis confirmed the success of the reaction as the carbonyl signal at δ_{C} 198.7, corresponding to C-9 in **5.35**, was not present, whilst a signal at δ_{C} 71.1 had emerged (**Figure 5.1**), confirming the structure of **5.36** as 1-methyl-1,2,3,4-tetrahydro-naphthalen-1-ol.



Scheme 5.4: Synthesis of tertiary alcohol **5.36**. (a) MeLi, anhydrous THF, -78°C .

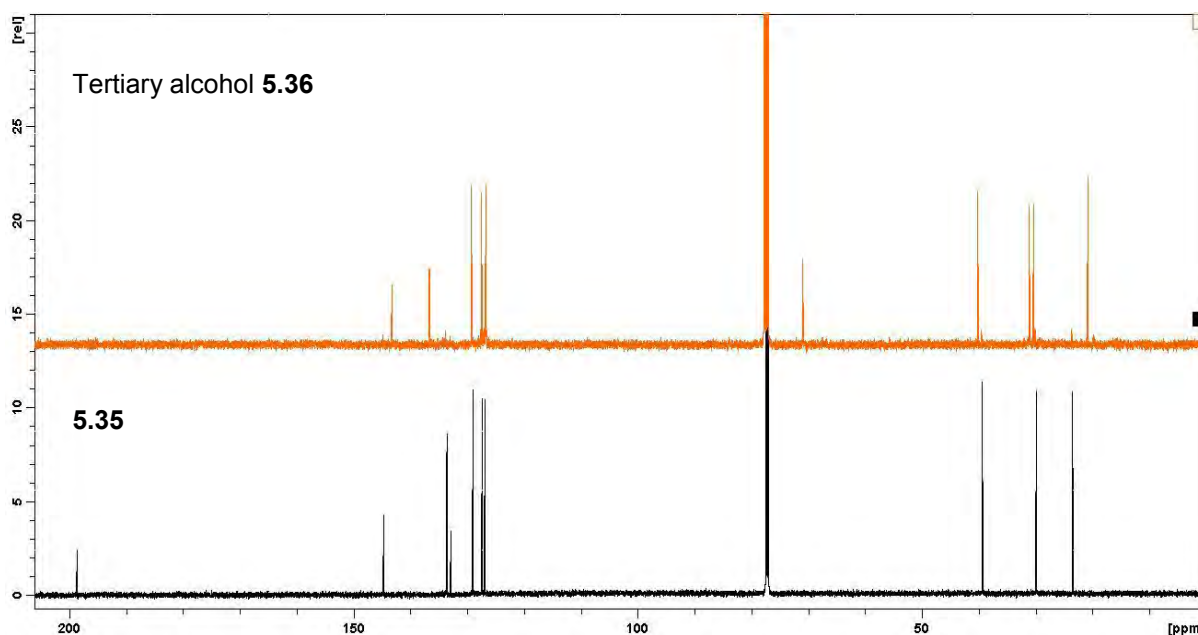
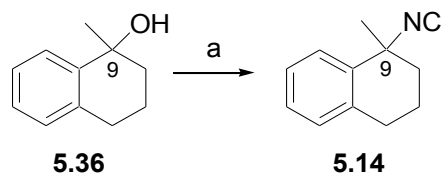


Figure 5.1: ^{13}C NMR (150 MHz) spectra of **5.35** (bottom) and **5.36** (top).

5.3.2 Preparation of Bicyclic Isonitrile **5.14**



Scheme 5.5: Synthesis of isonitrile **5.14**. (a) TMSCN, AgClO_4 , anhydrous DCM.

With the tertiary alcohol **5.36** in hand, we began our first attempts at the conversion of this compound into the isonitrile **5.14**. TMSCN proved to be a very difficult reagent to work with, not least because it is a masked form of hydrogen cyanide (HCN). HCN is liberated in the event of TMSCN coming into contact with water and the reaction was consequently carried out in anhydrous DCM and under an inert argon atmosphere. Paradoxically, these rigorous reaction conditions were not specified in either of Kitano *et al*'s procedures. As part of our safety precautions a cyanide antidote kit was always at hand. Our initial attempts at the reaction involved the AgClO_4 salt being added first, followed by DCM and finally TMSCN which was delivered via a gas-tight needle through a septum. When the reaction was conducted in this manner, only a small amount of starting material remained after the work-up

and so we decided to add the TMSCN first in DCM followed by the AgClO_4 . This presented a safety problem because the solid AgClO_4 would need to be added without breaching the air-tight seal thus potentially releasing HCN. To achieve this, we used a double-necked round-bottom flask equipped with a custom-made angled side arm that could be rotated to deliver the solid AgClO_4 into the reaction mixture once the TMSCN and DCM had been added through a septum on the other neck of the flask. When this method was used, gas bubbles (possibly of HCN) were observed in the solution as the AgClO_4 was added. We did not expect any gaseous products (**Scheme 5.3**) and were not surprised when post work-up analysis of the reaction contents revealed that the expected product had not formed in the reaction. On reflection we realised that we had been leaving the reaction to stir overnight before quenching with NaHCO_3 in an effort to ensure that the reaction had been completed. We proposed that the product, if it had formed, might be adhering to the precipitated AgOH discarded in the work-up. In order to rectify this, we allowed the reaction to run for only two hours before quenching and then promptly filtered the reaction solution through celite, followed by passing the filtrate through a short silica plug with 2:1 hexane:ethyl acetate. When the reaction was performed in this way, we isolated the product from unchanged **5.36** in low yield (24%). After further purification on HPLC, ^{13}C NMR data indicated that no signal was present at δ_{C} 71.1, as had been the case for C-9 in the spectrum of **5.36** (**Figure 5.2**).

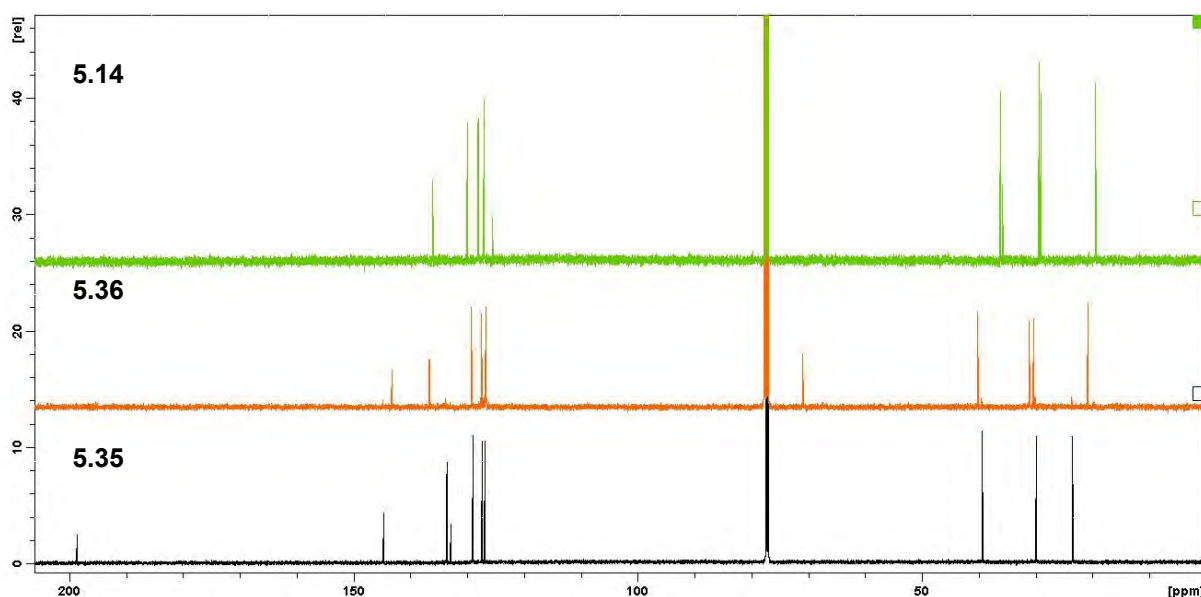


Figure 5.2: ^{13}C NMR (150 MHz) spectra of **5.14** (top), **5.36** (middle) and **5.35** (bottom).

Surprisingly the isocyanato triplet, a characteristic feature of isonitriles, was not evident in the ^{13}C NMR spectrum. Arising from $^{13}\text{C} - ^{14}\text{N}$ coupling, the signal of the carbon atom in the isonitrile functionality is split into a triplet that resonates at $\delta_{\text{C}} 150 - 170$.^{3,6,30} The splitting of the carbon signal arises from the ^{14}N quantum spin number (n) of 1 which results in a $2n + 1$ splitting pattern. It was thought that the absence of this triplet in our sample was because the isonitrile carbon is a very slowly relaxing species, requiring a longer data acquisition time.

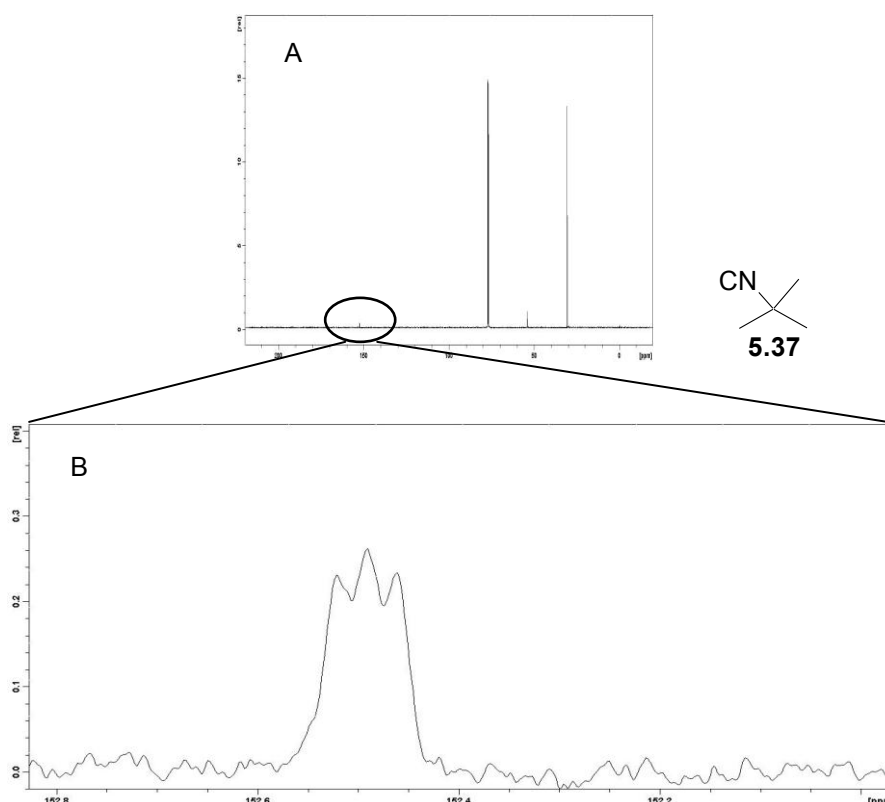


Figure 5.3: Relative intensity of the isocyanato peak to the other peaks in commercial *tert*-butyl isocyanide (**5.37**, Frame A). Structure of the isocyanato triplet caused by $^{13}\text{C} - ^{14}\text{N}$ coupling (Frame B).

The ^{13}C NMR spectrum of commercially available *tert*-butyl-isocyanide (**5.37**, **Figure 5.3**) shows the comparatively weak signal strength of the isocyanato triplet in a saturated sample and we anticipated that a longer data acquisition with an increased d_1 delay time might increase the signal/noise ratio.

Using *tert*-butyl isonitrile as a reference sample, we experimented with several different delay and acquisition times. The combination of a 5 second d_1 delay and a 24 hour acquisition time, gave the strongest isocyanato signal in the ^{13}C NMR spectrum of **5.37**. When this method was applied to **5.14**, a triplet signal at δ_{C} 167.9 was evident in the ^{13}C NMR spectrum (**Figure 5.4**). Compound **5.14** appeared to be unstable on prolonged storage in CDCl_3 . Weak absorptions at 2190 cm^{-1} and at 1589 cm^{-1} were observed, however, which would indicate that the isonitrile (and not the corresponding nitrile) was present.¹²² HREIMS data unequivocally established the molecular formula of **5.14** as $\text{C}_{12}\text{H}_{13}\text{N}$ ($\text{C}_{12}\text{H}_{13}\text{N}$ requires 171.1048, observed 171.1044).

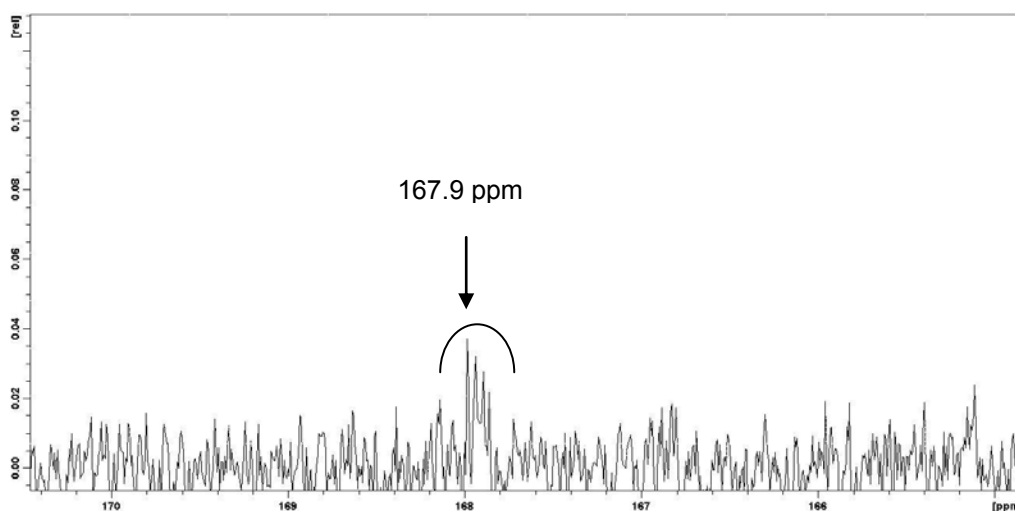
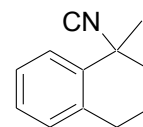


Figure 5.4: ^{13}C NMR (150 MHz) spectrum of **5.14**, showing the isocyanato triplet at δ_{C} 167.9.

5.4 Computational Analysis of Bicyclic Isonitrile 5.14

5.4.1 Molecular Bonding Orbital Maps and Electrostatic Potential of 5.14

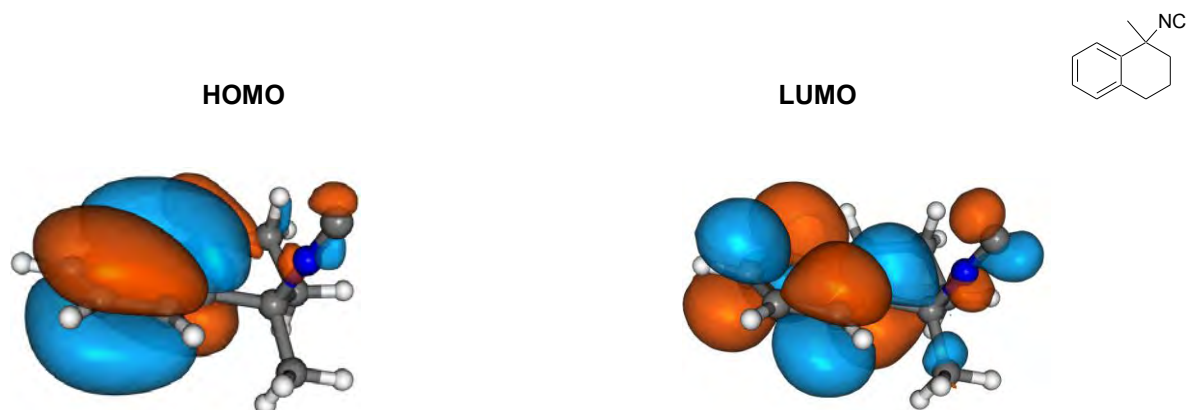


Figure 5.5: Electronic density maps of **5.14** HOMO and LUMO molecular orbitals.

Isonitrile **5.37** was subject to the same computational analyses as performed on Wright *et al*'s marine compounds (**1.30** – **1.42**), (Chapters 2 and 3), to determine if firstly, it possessed similar electronic properties to these anti-malarials and secondly to explore the potential of **5.14** to inhibit heme detoxification. Inspection of the molecular bonding orbital maps of **5.14** reveals a greater contribution by the isonitrile carbon and nitrogen atoms' orbitals to the HOMO and LUMO.

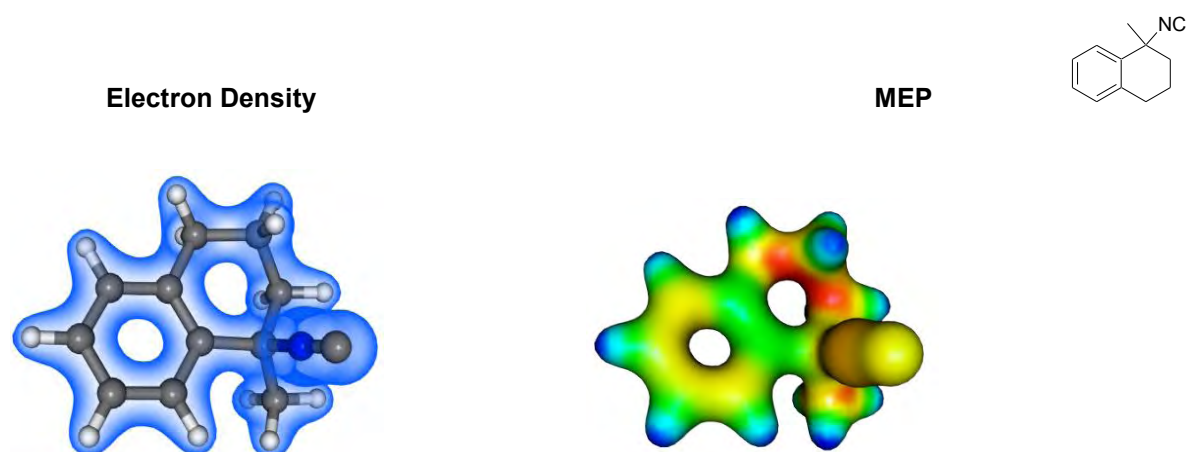


Figure 5.6: Molecular electrostatic potential (right) superimposed on a map of total electronic density (left) for structure **5.14**.

Electrostatic potential on the β -face of **5.14** (as shown in **Figure 5.6**) is relatively more negative and there are fewer positive nodes due to the lack of hydrogens orientated out of the molecular plane. Accordingly, as the model has regions of both positive and negative potential, we hypothesized that **5.14** would exhibit interesting interactions with heme and its dimer, possibly with „bond-less’ electrostatic associations as observed for the aminoquinolines, e.g. chloroquine (**1.2**).¹¹⁵

5.4.2 Docking of Bicyclic Isonitrile **5.14**

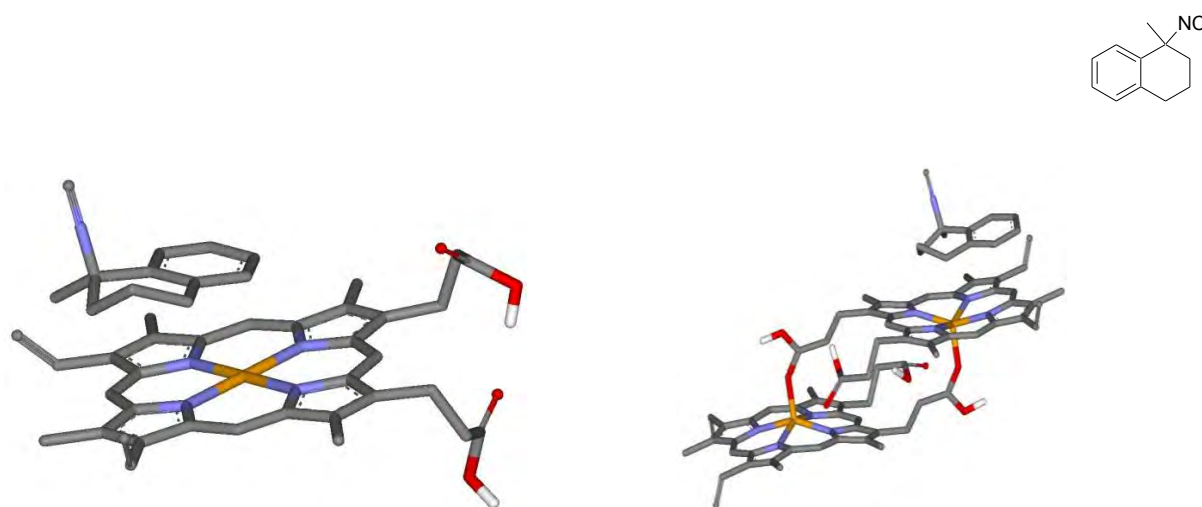


Figure 5.7: Lowest energy conformations for **5.14** docked against free heme (left) and the β -hematin dimer (right).

Examination of the results of the docking study of **5.14** with both heme and its dimer revealed that the carbon framework of **5.14** appears to behave in a similar fashion to CQ (Section 3.4.1), i.e. the aromatic ring orientates itself towards the iron ring centre. The isonitrile group is directed away from the receptor surfaces of both heme and the heme dimer in a similar fashion to the marine natural products (Section 3.4.2) and this model agrees with the electrostatic calculations (Section 5.7.2). The negative potential of the isonitrile will cause it to orientate itself away from the similarly negative flexible tails and pyrrolic nitrogens of heme. Consequently, once the molecule’s carbon framework has docked itself onto the porphyrin surface and established a „bond-less’ intermolecular attraction

reminiscent of the aminoquinoline family of inhibitor compounds,¹¹⁵ the approach of other heme groups will not be electrostatically favourable because of the exposed isonitrile group and further crystal growth will likely be inhibited. As the computational analyses suggested that **5.14** would potentially have heme-binding capabilities, we tested this hypothesis using the modified hemochrome (Phi- β) assay of Egan *et al.*⁶¹

5.5 Hemochrome Assay of Bicyclic Isonitrile 5.14

Isonitrile **5.14** showed promising activity in the hemochrome assay (Section 1.7.2) when compared to the known heme-binding chloroquine (**1.2**), resulting in greater intensification of the red shifted Soret absorption band at 404 nm (Figure). This indicates a higher concentration of free hematin in the solution and indicates that the sequestration of hematin into β -hematin crystals has been inhibited. The red line in **Figure 5.8** is the control sample containing only hematin and its slight absorption at 404 is due to the natural self-assembly of β -hematin in the reaction vessel.

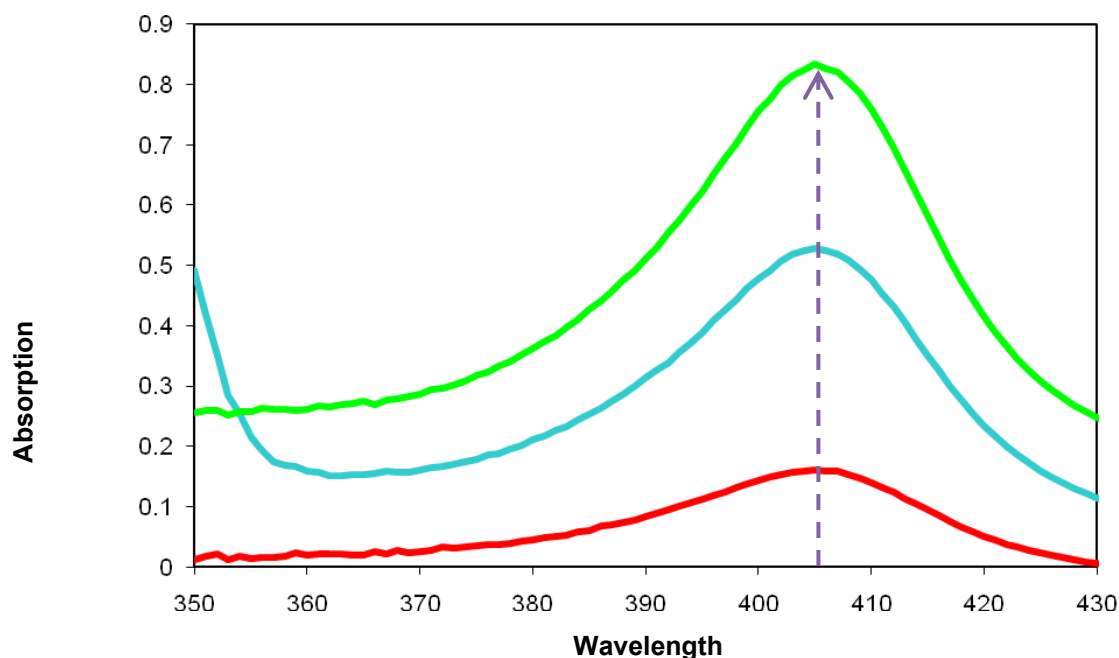
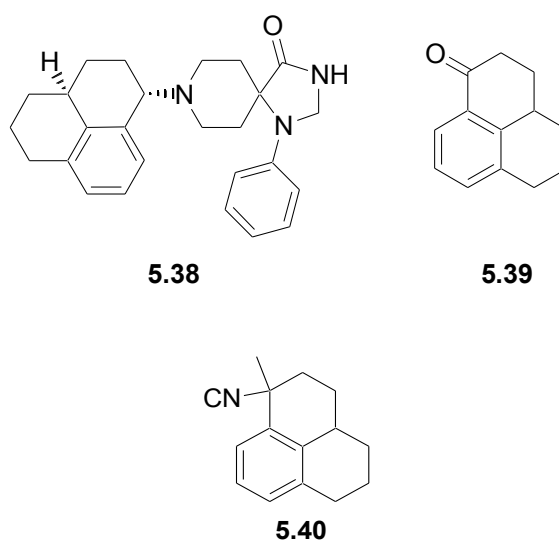


Figure 5.8: Absorption versus wavelength plots for the hemochrome assay of isonitrile **5.14** (green) and chloroquine (blue) after one hour of incubation. The absorptions at 404 nm are the Soret bands for the three systems (purple arrow) and the red line indicates the reference zero-line.

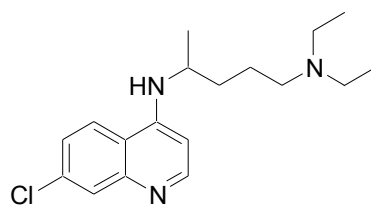
Regrettably time constraints prevented screening of this compound in *in vivo* anti-plasmodial assays.

5.6 A Tricyclic Precursor for Isonitrile Synthesis

In the synthesis of an orphanin FQ receptor agonist (**5.38**), Wichmann *et al* described a method for the synthesis of a tricyclic ketone, 2,3-dihydro-1H-phenalen-1-one (**5.39**),¹²³ which we envisaged as a precursor for the synthesis of tricyclic isonitrile analogues, e.g. **5.40**. the demethoxy analogue of **5.11** and **5.12** synthesized by Schwarz *et al*.⁶

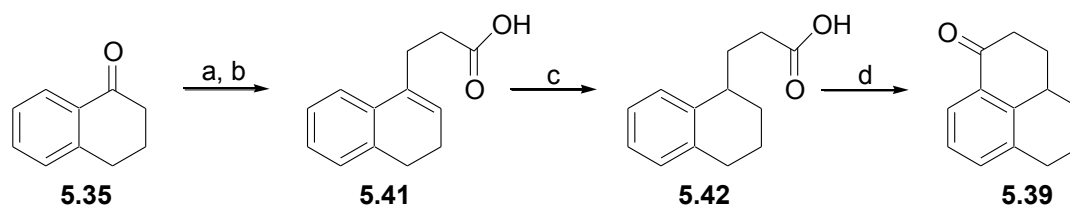


The use of **5.39** as a precursor would provide several advantages. Firstly, the ketone functionality could undergo nucleophilic alkylation with Grignard or organolithium reagents to produce a library of different analogues. Secondly, the aromatic ring in **5.39**, present in our active bicyclic isonitrile (**5.37**) should theoretically enable the molecule to bind to heme targets more effectively. One of the key structural features of chloroquine (**1.2**), and in fact most of the known inhibitors of heme detoxification,⁵⁵ is the aromatic aminoquinoline group which the various computational analyses (See Chapters 2-4) and current literature have shown to interact strongly with the heme receptor models.¹¹⁵



1.2

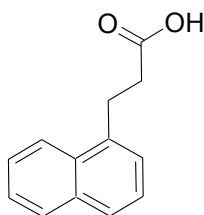
The synthesis of **5.39** was performed using the methods of Wichmann *et al* according to **Scheme 5.6**.¹¹⁹



Scheme 5.6: Synthesis of 2,3-dihydro-1H-phenalen-1-one (**5.39**). (a) diethyl succinate, KO^tBu, ^tBuOH, reflux; (b) AcOH, HCl, reflux; (c) Pd-C (5%), H₂; (d) PPA, 130°C.

5.6.1 Preparation of γ,δ -Unsaturated Acid **5.41**

This step involved a Stobbe-type condensation¹²⁴ of α -tetralone (**5.35**) and diethyl succinate with potassium *tert*-butylate in *tert*-butanol and subsequent hydrolysis/decarboxylation in acetic acid/hydrochloric acid to yield the γ,δ -unsaturated acid **5.41** along with the anticipated 3-(naphthalen-1-yl)-propionic acid (**5.43**), approximately 5%, as an impurity. Wichmann *et al* stated that the amount of this impurity present is dependent on reaction time and so the reaction times reported in their synthesis were strictly adhered to.

**5.43**

To separate the acid from the starting material, the reaction mixture was partitioned between ether and aqueous NaOH. Acidification of the aqueous layer afforded the organic acid (**5.41**) as a brown precipitate (53%). Crystallization of a portion of this precipitate from hexane:ethyl acetate, followed by re-crystallization from hot hexane yielded **5.41** as a pure off-white solid that was subsequently used for the hydrogenation, step.

5.6.2 Hydrogenation of **5.41** to Afford the Saturated Acid **5.42**

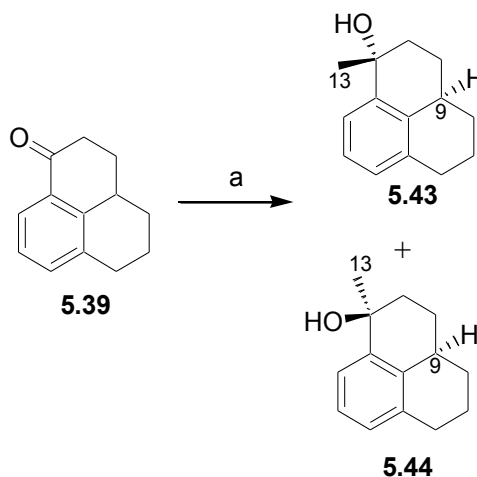
Hydrogenation of **5.41** with palladium on carbon (5%) and H₂ at atmospheric pressure quantitatively yielded the saturated racemic acid **5.42**. The success of the reaction was confirmed by the absence of the methine signal at δ_{H} 5.91 in the ¹H NMR spectrum of **5.41**, and the appearance of the methylene signal at δ_{H} 1.75 in the ¹H NMR spectrum of **5.42**. Column chromatography (toluene/ethyl acetate) was used to purify the racemic product before the next step which involved cyclization to form **5.39**.

5.6.3 Preparation of Tricyclic Ketone **5.39**

The acid **5.42** was transformed into the tricyclic ketone **5.39** in an intramolecular Friedel-Crafts acylation using polyphosphoric acid (PPA) as the acid catalyst. Purification on a short silica column produced sufficiently clean **5.39** (81%) for alkylation with MeLi as used previously on the bicyclic system.

5.6.4 Methylation of Tricyclic Ketone **5.39**

Compound **5.39** was alkylated using methyl lithium (MeLi) to produce the diastereomeric pairs (represented by **5.43** and **5.44**, enantiomers not shown) as detailed in **Scheme 5.8**.¹²¹ These pairs were separated using normal phase high performance liquid chromatography (HPLC) with a 7:1 hexane:ethyl acetate solvent system.



Scheme 5.7: Synthesis of the diastereomers **5.43** and **5.44** (enantiomers not shown). (a) MeLi, anhydrous THF, -78°C .

Using NOESY (nuclear Overhauser enhancement spectroscopy) NMR correlation studies, these two pairs were successfully differentiated by monitoring the through-space interactions occurring between the methyl protons at 13-Me and the methine proton at C-9. In the case of the anti-diastereomer (**5.43**), the protons at these two positions are on opposite sides of the molecule, thereby increasing their interatomic distances and preventing any through-space NOE correlations (**Figure 5.9**).

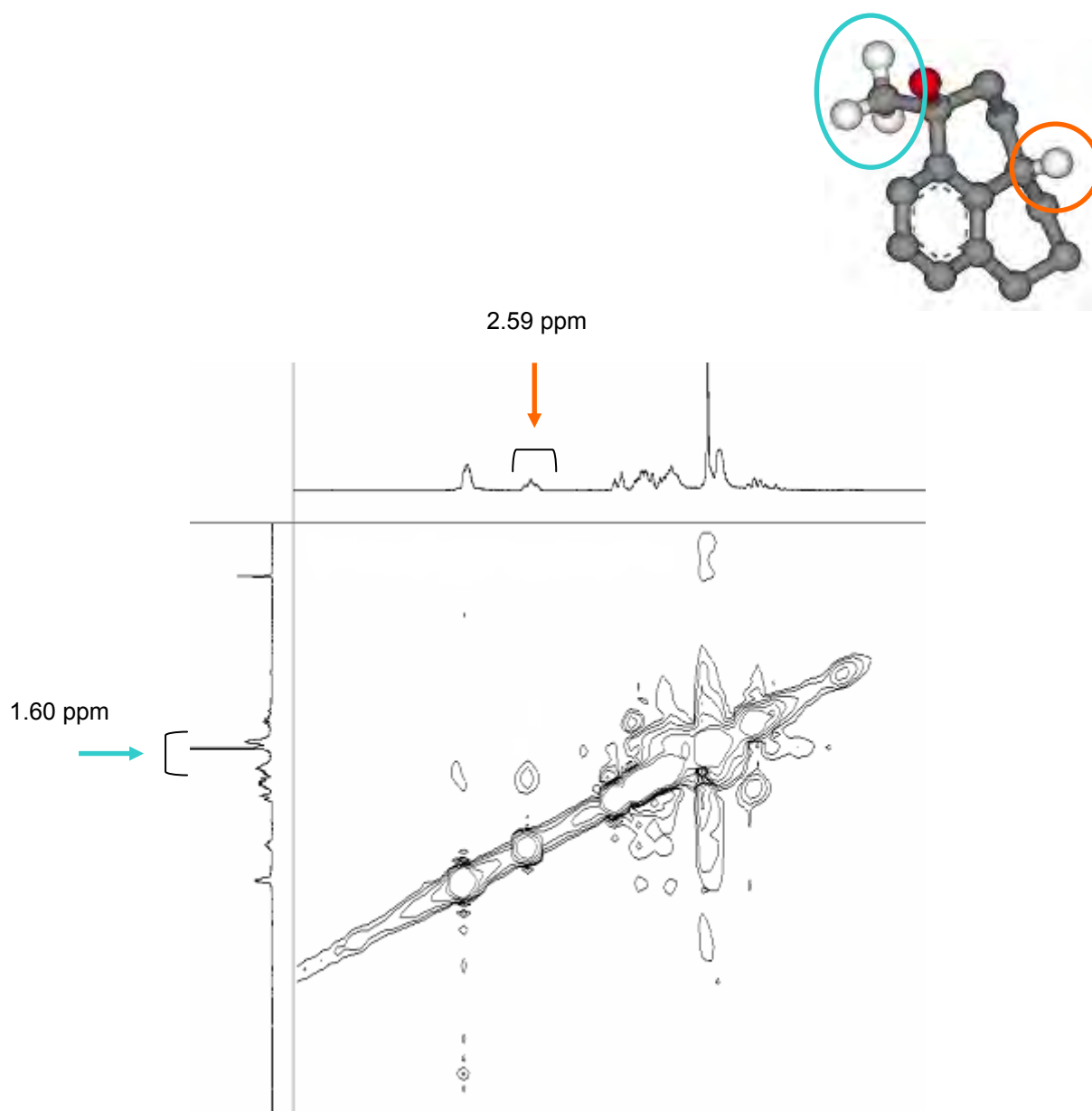


Figure 5.9: A section of the NOESY spectrum for **5.43**. The increased interatomic distance between the methyl (blue) protons and the methine proton at position C-9 (orange) results in no correlation between the two signals in the spectrum.

In the case of the *syn*-diastereomer however, these two sets of protons are on the same side of the molecule and the now reduced interatomic distance allows for through-space NOE interactions to occur (**Figure 5.10**).

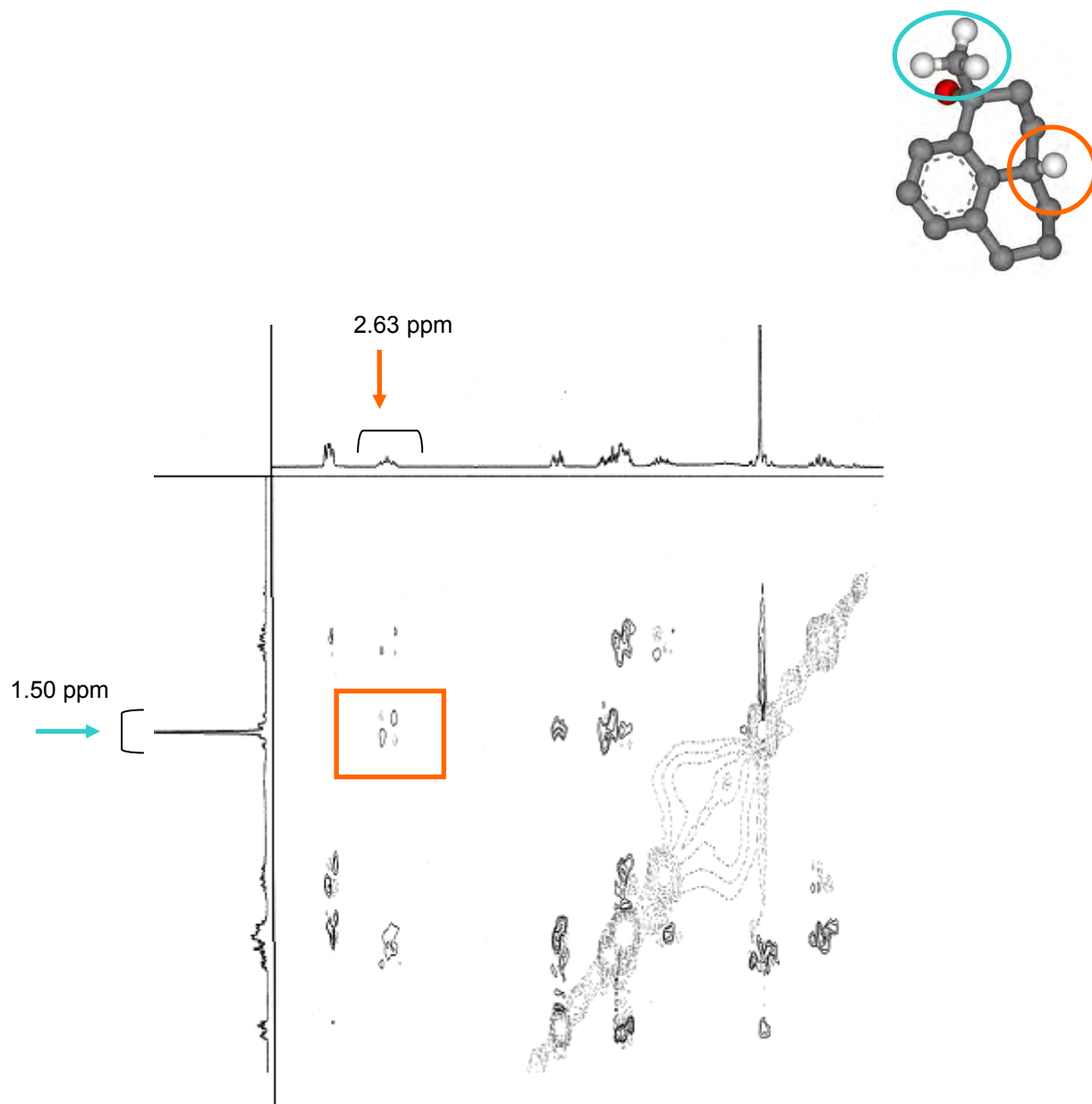


Figure 5.10: A section of the NOESY spectrum for **5.43**. The reduced interatomic distance between the methyl (blue) protons and the methine proton at position C-9 (orange) results in correlation between the two signals in the spectrum (orange rectangle).

5.7 Attempted Synthesis of Tricyclic Isonitriles using the Method of Kitano *et al*

Before this reaction was attempted on the isolated diastereomeric pairs (**5.42** and **5.43**), it was first tried on a mixture of diastereomers using the same process that had proven successful for the bicyclic system (Section 5.3.2). After two attempts, the reaction had returned only starting material. We then decided to try a different solvent, i.e. benzene, in the hopes of promoting the S_N1 reaction. We chose benzene as it is a non-polar, aprotic solvent that should not hamper transfer of the cyanide ion with the improved solubility of AgClO₄ in benzene an added attraction. By increasing the solubility of the silver salt, we hoped to make the Ag⁺ and ClO₄⁻ ions more available for the reaction. Unfortunately, the reaction was again unsuccessful and the tricyclic isonitrile could not be synthesized. It must be noted that in Schwarz *et al*'s synthetic endeavour, they too were unable to convert a tricyclic tertiary alcohol to its corresponding isonitrile by means of Kitano *et al*'s earlier synthetic method (**Scheme 5.1**). We similarly attempted the conversion of the plant natural product **5.16** into its isonitrile derivative **5.17**, also with no success.

5.9 Conclusion

A bicyclic tertiary isonitrile (**5.14**) was successfully synthesized and the *in vitro* assay data indicates that this compound was capable of inhibiting β-hematin formation, apparently to a possibly greater degree than the known inhibitor chloroquine. Whether the compound is capable of exerting an equally potent degree of inhibitory action *in vivo* will need to be determined through screening against *P. falciparum*. Whilst Kitano *et al*'s synthetic methodology enabled the conversion of the simple bicyclic tertiary alcohol to its corresponding isonitrile, it was not suitable for the preparation of isonitriles in more complex compounds. Our lack of success at the conversion of isonitriles in more complex compounds appears to concur with the findings of Schwarz *et al* and may explain why this procedure has not found wider acceptance in the chemistry literature.

In conclusion, tertiary isonitriles have been shown in the literature to be highly effective inhibitors of *P. falciparum* proliferation and our studies have highlighted their ability to possibly hinder plasmodial heme detoxification processes as determined in an *in vitro* screen. The pharmacophore model suggested by Wright *et al*'s pseudoreceptor model has been shown to provide valuable structural information for the design of novel inhibitor compounds that exert their activity in a similar fashion to the chloroquine family of compounds, i.e. via "bond-less" intermolecular attractions with heme structures in the plasmodial food vacuole. Whilst the isonitrile grouping may not form formal bonds with the heme target, molecules containing this functionality still exhibit potent inhibitory potential. The computational methodologies employed in this study, used to assess the inhibitory potential of **5.14**, have successfully predicted the ability of the compound to inhibit β -hematin formation *in vitro* and therefore may provide an avenue for the rational design of new anti-malarial drugs interacting with the detoxification of heme process in the parasite.

EXPERIMENTAL PROCEDURES

6.1 Chapter Two Experimental

6.1.1 General

Models were constructed in DS Visualizer¹²⁵ (unless otherwise stated) and exported in .mol2 format. DFT calculations (energy optimizations, frequency analyses and full population analyses) were performed using the Gaussian 03 suite of algorithms with the 6-31G(d) vector basis set and the B3LYP functional.^{71,72,113} Bonding orbital maps were generated from population analysis data with the CUBEGEN program as implemented in the Gaussian 03 suite and visualized in Molekel.¹²⁶ Molecular electrostatic potentials (MEPs) were generated by superimposing electrostatic data from the population analyses onto maps of total electronic density obtained from the DFT calculations using the software package Molekel. All structures and isosurfaces were visualized using Molekel with bond order being characterized by the number of hydrogen atoms present.

6.1.2 Construction of Chloroquine and Marine Isonitrile, Isocyanate and Isothiocyanate Electronic Models

Models were constructed and were subsequently minimized using spin-restricted DFT structural optimizations, followed by full frequency analyses to ensure that all structures were true stationary points.

6.1.3 Molecular Bonding Orbitals of Chloroquine and Marine Isonitriles, Isocyanates and Isothiocyanates

Full orbital population analyses were performed. Highest occupied and lowest unoccupied molecular orbital maps (HOMO and LUMO) were generated and visualized using isocontour values of 0.02 e/bohr³. Both negative and positive parity orbital lobes were rendered.

6.1.4 Construction of Hematin and β -Hematin Dimer Electronic Models

The receptor model for the hematin dimer (HD) was obtained from the Cambridge Structural Database (CSD code 162267) and the free heme group model (FP) was obtained from the Protein Database (PDB code 2q9f).^{127,128} The FP model was subjected to energy optimizations using unrestricted DFT calculations in the singlet and triplet electronic states; whilst the quintet electronic state model was optimized using the LANL2DZ¹²⁹ pseudopotential to describe the iron atom and then the UB3LYP/6-31G(d) method for all other atoms. A single-point spin unrestricted energy calculation was performed on the HD crystal structure in the singlet electronic state.

6.1.5 Molecular Bonding Orbitals of Free Heme and β -Hematin Dimer Models

Full orbital population analyses were performed on the minimized triplet FP model and the singlet HD crystal structure. HOMO and LUMO orbital maps were generated and visualized using isocontour values of 0.01 e/bohr³. Both negative and positive parity orbital lobes were rendered.

6.1.6 Molecular Electrostatic Topologies of Chloroquine, Marine Isonitriles, Isocyanates and Isothiocyanates; and Heme Targets

Molecular electrostatic potentials (MEPs) were generated and visualized. The colour scale is as follows:

- Red – Highly Electronegative
- Yellow – Moderately Electronegative
- Green – Neutral
- Light Blue – Moderately Electropositive
- Deep Blue – Highly Electropositive

6.2 Chapter Three Experimental

6.2.1 General

Models were constructed in DS Visualizer (unless otherwise stated) and DFT calculations (energy optimizations, frequency analyses and full population analyses) were performed using the Gaussian 03 suite of algorithms with the 6-31G(d) vector basis set and the B3LYP functional. All output data was visualized using DS Visualizer.

6.2.2 Validation of a Theoretical Malarial 1-Deoxy-D-xylulose-5-phosphate Reductoisomerase Enzyme Model

6.2.2.1 Ligand Model Preparation

The ligand models of structures **3.1** – **3.32** were constructed with phosphonate moieties in the deprotonated state, and was subjected to DFT structural optimization. The minimized structures were imported into AutoDockTools¹³⁰ as implemented in the MGLTools¹³¹ graphical

user interface. AutoDock atom types were assigned, Gasteiger charges were added and non-polar hydrogens were merged. Bond torsions were assigned and aromatic elements identified. These files were then exported as PDBQT files (**P**rotein **D**atabase with **C**harges (**Q**) and **T**orsions).

6.2.2.2 Receptor Model Preparation

The *EcDXR* model was obtained by removing FOS from the binding site of the reference crystal structure (Protein Data Bank code 1Q0L)⁸⁷ and the model was desolvated using AutoDockTools; the NADPH cofactor was retained in the structure to yield the primed *EcDXR* structure for future docking. The primed *PfDXR* model was constructed in the unsolvated state and included the bound NADPH cofactor.⁸² Non-polar hydrogens on both models were merged using the AutoDockTools set, followed by computation of atomic charges with the Gasteiger charge equilibration method. The following catalytic residues within the active sites were kept flexible:

EcDXR: Ser186, Ser222, Asn227, Lys228, Glu231

PfDXR: Ser199, Ser135, Asn140, Lys141, Glu144

6.2.2.3 Generation of Grid Maps and Statistical Docking

Grid maps for each of the ligands were generated across the active sites, with surrounding residues, using a grid box of 60³ points (0.375 Å point spacing) referenced to the bound NADPH. The dockings were executed according to a Lamarckian genetic algorithm to create populations containing 150 individuals and allowing for a maximum of 2.5 x 10⁶ energy evaluations for each of 10 unique docks per ligand. The results were clustered and the lowest energy conformer from each cluster printed as part of the docking log file along with its associated energies. These conformers were extracted from the log file using custom scripting and visualized.

The lowest energy conformers from each dock were then visually analyzed and the ligand scoring data used to decide upon the optimal conformation for each docking run. The reference docking protocol was achieved by docking a minimized FOS structure back into the primed *EcDXR* structure.

6.2.3 Statistical Docking Analyses of Chloroquine and Marine Isonitriles, Isocyanates and Isothiocyanates

6.2.3.1 Ligand Model Preparation

The ligand models of structures **1.30** – **1.42** were constructed and subjected to DFT structural optimization. The minimized structures were imported into AutoDockTools, AutoDock atom types were assigned, Gasteiger charges were added and non-polar hydrogens were merged. Bond torsions were assigned and aromatic elements identified. The assigned Gasteiger charges were substituted with Mulliken¹³² atomic charges from the DFT optimization output logs. For all atoms other than polar hydrogens and their attached heavy atom, Mulliken charges were computed with attached hydrogens' charges merged into the heavy atom. For polar hydrogens, unmerged charges were used for both the hydrogen and the heavy atom.

6.2.3.2 Receptor Model Preparation

The minimized heme models from Section 2.5 were imported into AutoDockTools, AutoDock atom types were assigned, Gasteiger charges were added and non-polar hydrogens were merged. All rotational elements on the heme targets, i.e. vinyl and carboxylic acid groups, were treated as the flexible residues. The Gasteiger charges were substituted for Mulliken atomic charges as previously mentioned.

6.2.3.3 Generation of Grid Maps and Statistical Docking

Grid maps for each of the ligands were generated across the active sites, with surrounding residues, using a grid box of 50^3 points (0.325 Å point spacing) referenced to the iron atom. The dockings were executed according to a Lamarckian genetic algorithm to create populations containing 150 individuals and allowing for a maximum of 2.5×10^6 energy evaluations for each of 10 unique docks per ligand. The results were clustered and the lowest energy conformer from each cluster printed as part of the docking log file along with its associated energies. These conformers were extracted from the log file using custom scripting and visualized.

6.3 Chapter Four Experimental

6.3.1 Semi-Empirical “Forced-Binding” Analysis

Each of the marine compounds was artificially bonded to the iron centre of the FP model to produce force-bound complexes. In the case of compounds possessing two functional groups, individual complexes were generated with each of the functional groups being bound to the receptor. The intermolecular bond was subjected to a brief structural optimization within the DS Visualizer program and the bond was then removed. The resultant bi-molecular systems of structures **1.31**, **1.33** and **1.39** (both functional groups) then was subjected to AM1 energy optimizations as implemented in Gaussian 03. The output logs of these runs were examined and their trajectories visualized using Molekel.

6.3.2 Application of an *Ab Initio* Molecular Dynamics Method to a Naturally Occurring Non-Oligomeric Molecular Zipper

6.3.2.1 General

Structures and trajectories were visualized using Molekel, DS Visualizer and VMD.¹³³

6.3.2.2 Zipper Model Construction

All molecular construction, structural optimization and quench dynamics were done using the Cerius 2.0 program.¹³⁴ The zipper models were constructed in two stages:

1. Monomer preparation

The structure of the (R) epimer was obtained from the X-ray crystal data and the Universal 1.02 forcefield was applied.¹³⁵ Atomic charges were computed using the charge equilibration method (convergence criterion 5.0E-4, max iterations 50) with the Qeq_charged 1.0 parameter set. An energy minimization was then performed (max displacement 2.00 Å, ABNR termination 50.0 kcal mol⁻¹, QN termination 0.100 kcal mol⁻¹, asymmetric atomic limit 200, total atomic limit 100) for over 500 iterations with standard convergence (0.0100 kcal mol⁻¹ RMS atomic force, overall energy diff. 1.000E-3 kcal mol⁻¹, overall RMS displacement 3.0000E-3 Å). The model then was subjected to molecular dynamics with constant NVE using the quench dynamics method at 300 K (1.0E5 steps, temperature scaling applied 50.0 K, 2000 steps between quenches, 0.0010 ps time step, max coordinate optimization steps 500, coordinate steps per cycle 10, charge equilibration at each step for 50 iterations); and then at 600 K (1.2E6 steps, temperature scaling applied 50.0 K, 6000 steps between quenches, 0.0010 ps time step, max coordinate optimization steps 500, coordinate steps per cycle 10, charge equilibration at each step for 50 iterations) with the minimum structure from the first

dynamical run being used for the second run. The final (R) epimer was then rearranged to produce the (S) epimer by exchanging the methyl and proton groups at the C13 position.

2. *N-meric system preparation*

Polymers comprising n monomeric units were constructed for $n = 2-6$. These polymers were built by arranging (R) and (S) monomers into a zipper structure and then adding (artificial) formal bonds where hydrogen bonds would be present. The Universal 1.02 force field was applied, atomic charges were added and the energies minimized (as per monomers) for over 1500 iterations. Upon energy convergence, the artificial hydrogen bonds were removed, the Dreiding 2.21 force field was applied,¹³⁶ atomic charges were re-calculated and the energies minimized for over 1500 iterations. The models were then subjected to molecular dynamics with constant NVE using the quench dynamics method at 600 K (1.2E6 steps, temperature scaling applied 50.0 K, 8000 steps between quenches, 0.0010 ps time step, max coordinate optimization steps 500, coordinate steps per cycle 10, charge equilibration at each step for 50 iterations), the minimum conformers were taken and their energies minimized.

6.3.2.3 *Energy Minimizations*

Mono-, di-, and trimeric systems of the (R) and (S) epimers were minimized using SE, DFT and ONIOM hybrid methods as implemented in the Gaussian 03 suite. The semi-empirical and DFT calculations were done at the AM1 and B3LYP/6-31G(d) levels respectively, whilst the ONIOM was a hybrid of the two. The carbon structures adjacent to the hydrogen bonding hydroxyl groups were treated at the 6-31G(d) level and the remaining groups were treated at the AM1 level. Association energy data was obtained from the AM1 calculations. Structures and trajectories were visualized using Molekel and DS Visualizer.

6.3.2.4 Car-Parrinello Molecular Dynamics

The CPMD analyses involved three steps: wavefunction optimization, temperature equilibration and dynamical runs. All steps were performed using a point group delta value of 1.0E-6, the BLYP gradient correction functional and Goedecker pseudopotentials for all atom types.¹³⁷ All runs were performed using the CPMD program.¹³⁸

1. Wavefunction Optimization

The unit cell structure (orthorhombic) and translational vectors for the (R) epimer were obtained from the X-ray crystal data. The (S) epimer unit cell was constructed by inverting the symmetry at all C-13 centres within the (R) cell. Wavefunction optimizations of the two systems were performed with an orbital convergence of 1.0E-7 and a spherical planewave cut-off of 30 Rydberg.

2. Temperature Equilibration

Once wavefunction convergence had been achieved, the cells were then subjected to 200 steps of equilibratory CPMD dynamics, to obtain orbital velocities, at 300.0 K with maximum ionic temperature variations of ± 50.0 K.

3. Dynamical Runs

The cells were then subjected to 1.0E4 steps of dynamics at 300.0 K with Nosè-Hoover thermostating¹³⁹ maintaining ionic and electronic kinetic energies. The dynamical runs used a time step of 4 au and a fictitious atomic mass of 400 amu. The unit cells of output trajectories were extended using custom scripting and then visualized.

6.3.3 CPMD Simulations of Heme Systems

The systems that were subjected to the “force-binding’ analyses in Section 6.3.1 were subjected to analysis using the CPMD method. The same starting configurations for structures **1.31**, **1.33** and **1.39** were used as initial arrangements for the unit cells undergoing dynamical simulation. All runs were performed using the CPMD program.

The unit cells (orthorhombic) were constructed by translating the starting configuration co-ordinates from the structural files to new positions using the iron atom as the centre of the cell (0,0,0). Translational vectors were assigned the maximum co-ordinate values in their respective directions and were kept orthogonal to one another. The same sequence of wavefunction optimization, equilibration dynamics and full dynamics was applied as in Section 7.3.2.4 with the same parameters; with there being only two deviations. Firstly, extended form pseudopotentials were used for all atom types as the iron atom could not be expressed using standard potentials; extended form potentials were used for all atoms so as to maintain uniformity. Secondly, a pre-configured conjugate gradient energy minimizing function (PCG) was used in place of the standard ODIIIS method. The PCG minimizer is a slower but more robust method that was necessary to handle the size of the heme systems.¹⁴⁰

6.4 Chapter Five Experimental

6.4.1 General

6.4.1.1 Analytical

Infra-red spectra were recorded on a Perkin-Elmer Spectrum 2000 FT-IR and DigiLab FTS 3100 Excalibur HE spectrometer with compounds as films (neat) on KBr discs. NMR spectra were acquired on Bruker 400 MHz Avance and 600 MHz Avance II spectrometers using standard pulse sequences. Chemical shifts are reported in ppm, referenced to residual

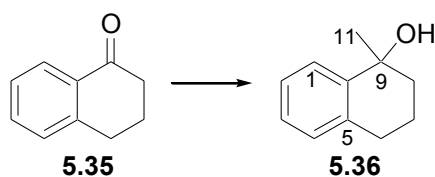
solvent resonances (CDCl_3 δ_{H} 7.25, δ_{C} 77.0). Coupling constants are reported in Hz directly from the NMR spectra. Low and high resolution mass spectra were recorded on a Finnigan GCQ spectrometer at 70 eV. High resolution fast atom bombardment mass spectra (Micromass 70-70E spectrometer) were obtained by Prof. L. Fourie of the Mass Spectrometry Unit, Northwest University, Potchefstroom, South Africa. High resolution electron impact mass spectra (Thermo DFS magnetic Sector mass spectrometer) were obtained by Dr. M. Ferreira of the Mass Spectrometry Service, University of the Witwatersrand, Johannesburg, South Africa.

6.4.1.2 Chromatography

General laboratory solvents were distilled from glass before use. Analytical normal phase thin layer chromatography was performed on DC-Plastiekfolien 60 RP18 F₂₅₄ plates. Plates were viewed under UV light (254 nm) and developed either with I₂ or by spraying with 10 % H₂SO₄ in MeOH followed by heating. Flash chromatography was performed using Kieselgel 60 (230-400 mesh) silica gel. Normal phase semi-preparative HPLC separations were performed on a Whatman Magnum 9 Partisil 10 column using a Spectra-Physics Spectra Series P100 isocratic pump and a Waters 410 Differential Refractometer.

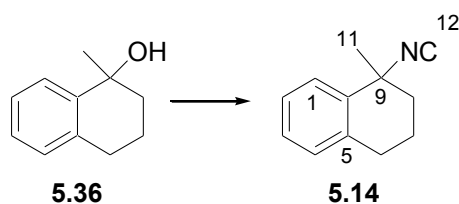
6.4.1.3 Synthesis

All reactions requiring anhydrous conditions were conducted in flame-dried apparatus either under a dry argon atmosphere or using an anhydrous calcium chloride drying tube. Dry solvents were prepared by standard procedures as described by Perrin and Amarego¹⁴¹ and stored over the appropriate drying agent under an atmosphere of dry nitrogen. Immediately prior to their use in anhydrous reactions, THF was distilled from Na/benzophenone ketyl, while CH₂Cl₂ was distilled from calcium hydride and stored over 4 Å molecular sieves under nitrogen. Organic extracts were dried over anhydrous MgSO₄. All reactions were magnetically stirred.

6.4.1 Methylation of α -Tetralone

α -Tetralone (**5.35**, 500 mg, 0.455 mL, 3.4 mmol) was taken up in dry THF (25 mL) with stirring under an argon atmosphere. The solution was cooled to $-78\text{ }^{\circ}\text{C}$ and MeLi (7 mL, 1.6M in THF) was added. The reaction was allowed to warm to room temperature, stirred (12 h) and quenched with sat. NaHCO_3 solution (100 mL). The reaction mixture was extracted with diethyl ether (2 x 100 mL). The combined organic layers were washed with water (2 x 100 mL), brine (1 x 100 mL), dried over MgSO_4 and evaporated to give a brown oil which was crystallized from hot hexane to yield **5.36** as off-white needles (420 mg, 2.59 mmol, 76 %).

1-Methyl-1,2,3,4-tetrahydro-naphthalen-1-ol (5.36): off-white needles; mp. $79\text{ }^{\circ}\text{C}$; IR ν_{max} 3411, 2928, 2352, 1688, 1453 cm^{-1} ; ^1H NMR (CDCl_3 , 600 MHz) δ 7.58 (1H, d, $J = 7.6$, H-1), 7.20 (2H, br s, H-2 and H-3), 7.06 (1H, d, $J = 7.2$, H-4), 2.79 (2H, t, $J = 5.4$, H₂-6), 1.95 (2H, t, $J = 7$, H₂-8), 1.60 (2H, br s, H₂-7), 1.56 (3H, s, H₃-11); ^{13}C (CDCl_3 , 150 MHz) δ 142.9 (C, C-10), 136.2 (C, C-5), 128.8 (CH, C-1), 127.1 (CH, C-2), 126.3 (CH, C-3), 126.3 (CH, C-4), 70.6 (C, C-9), 39.8 (CH_2 , C-8), 30.7 (CH_3 , C-11), 29.9 (CH_2 , C-6), 20.4 (CH_2 , C-7); HREIMS m/z 162.1048 (calcd for $\text{C}_{11}\text{H}_{14}\text{O}$ [M^+], 162.1045).

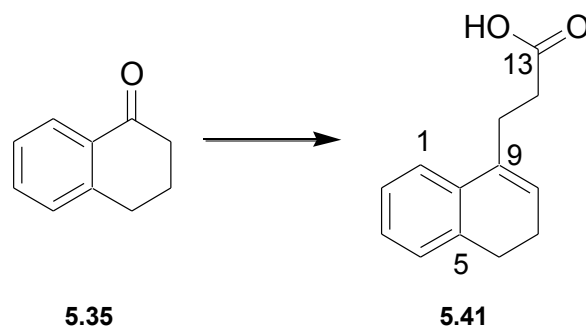
6.4.2 Preparation of Bicyclic Isonitrile **5.14**

Alcohol **5.36** (128 mg, 0.79 mmol) was taken up in 1 mL dry DCM under an inert argon atmosphere. TMSCN (210 μ L, 1.58 mmol) was injected, solid AgClO_4 (164 mg, 0.79 mmol) was added and the mixture was stirred at r.t. for 2 h. The reaction was subsequently quenched with 1 mL sat. NaHCO_3 solution, stirred for 10 min and then filtered through a celite plug. The plug was washed with ethyl acetate (100 mL) and the combined organic layers concentrated under reduced pressure. The products were then passed through a short silica column (2:1 hexane:ethyl acetate) and purified with HPLC (7:1 hexane:ethyl acetate) to yield **5.14** as a brown oil.

1-Isocyano-1-methyl-1,2,3,4-tetrahydro-naphthalene (5.14): brown oil; IR ν_{max} 2937, 2361, 2190, 1589, 1015 cm^{-1} ; ^1H NMR (CDCl_3 , 600 MHz) δ 7.47 (1H, d, $J = 7.6$, H-1), 7.22 (2H, br s, H-2 and H-3), 7.09 (1H, d, $J = 7.2$ Hz, H-4), 2.82 (2H, t, $J = 6$ Hz), 1.90 (2H, t, $J = 6.9$, H₂-8), 1.72 (3H, s, H₃-11), 1.57 (2H, br s, H₂-7); ^{13}C (CDCl_3 , 150 MHz) δ 167.9 (C, t, C-12), 135.8 (C, C-10), 135.7 (C, C-5), 129.7 (CH, C-1), 127.8 (CH, C-2), 127.7 (CH, C-3), 126.7 (CH, C-4), 68.0 (C, C-9), 38.7 (CH_2 , C-8), 29.2 (CH_3 , C-11), 19.2 (CH_2 , C-7). HREIMS m/z 171.1048 (calcd for $\text{C}_{12}\text{H}_{13}\text{N}$ [M^+], 171.1044).

6.4.3 Hemochrome Assay of Bicyclic Isonitrile **5.14**

The assay was performed according to the procedure of Egan *et al.*⁶¹ Hematin stock solution (20.2 μ l; 1.680 mM), prepared by dissolving bovine hemin in 0.1 M NaOH (used within 60 min of preparation), was dispensed in a series of Eppendorf tubes (33.6 nmol/Eppendorf tube). Tubes were prepared (in triplicate) containing 2.02 μ l of isonitrile **5.14** and chloroquine (**1.2**) at a concentration of 1.680 mM, prepared by dissolving the drug in 1.0 M methanol. Once dissolved in methanol, the 0.1 M NaOH portion of the solution was neutralized with 2.02 μ l of 1.0 M HCl to prevent drug precipitation. Concentrations were predetermined to give 0–10 equivalents relative to hematin in the final solution. After mixing, 11.74 μ l of 12.9 M acetate solution (pH 5.0), pre-incubated in a thermostated water bath at 60 °C, was added. The final hematin concentration was 1.0 mM and the final solution pH was 4.5. The reaction mixtures were incubated at 60 °C for 60 min. They were then quenched at room temperature by adding 900 μ l of 5% (v/v) pyridine (200 mM Hepes buffer, pH 8.2) to buffer the mixtures to a final pH between 7.2 and 7.5. This was followed by adding 1100 μ l of 5% (v/v) pyridine solution (20 mM Hepes buffer, pH 7.5). Solutions were shaken to ensure complete dissolution of hematin and the β -hematin was allowed to settle at ambient temperature for at least 15 min. Supernatants were carefully transferred to a cuvette without disturbing the precipitate. Absorbances were from 350–700 nm on a Carey 100 UV/Vis spectrometer using glass cuvettes.

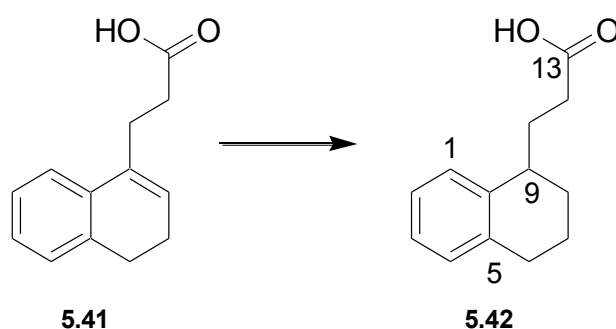
6.4.4 Preparation of γ,δ -Unsaturated Acid **5.41**

α -Tetralone (**5.35**, 9.1 mL, 68.4 mmol) was added to a stirred mixture of diethyl succinate (9.6 mL, 57.3 mmol) and potassium *tert*-butylate (11.73 g, 104.5 mmol) in *tert*-butanol (50 mL). The mixture was heated under reflux for an hour and then evaporated. HCl (20 mL, 8 M) was added and the product was extracted with diethyl ether (2 x 100 mL). The combined organic layers were washed with brine, dried with MgSO₄ and evaporated to give a brown oil which was subsequently heated in a mixture of conc. acetic acid (50 mL) and conc. HCl (50 mL) for 3 hours under reflux. The mixture was evaporated, added to water (125 mL) and extracted with ethyl acetate (2 x 100 mL). The combined organic layers were washed with NaOH (120 mL, 3 M), acidified with conc. HCl, extracted with ethyl acetate (2 x 100 mL), washed with water (2 x 100 mL) and the combined aqueous phases back extracted with ethyl acetate (2 x 100 mL). Combined organic layers were washed with brine (50 mL), water (2 x 50 mL), dried with MgSO₄ and evaporated to give the crude product as a brown oil which crystallized on standing. Purification was achieved using column chromatography, crystallization from ethyl acetate and hexane (1:19) and recrystallization from hexane to produce 3-(3,4-dihydro-naphthalen-1-yl)-propionic acid as off-white needles (**5.41**, 1.81 g, 8.94 mmol, 13 %) and the crude product as a brown oil (7.78 g, 38.51 mmol, 56 %)

3-(3,4-dihydro-naphthalen-1-yl)-propionic acid (5.41): off-white needles; mp. 191 °C; IR (Disc) ν_{\max} 3019, 2930, 1707, 1433 cm⁻¹; ¹H NMR (CDCl₃, 600 MHz) δ 7.24 (1H, d, J = 6.7 Hz, H-1), 7.22 (1H, d, J = 7.7 Hz, H-4), 7.20 (1H, t, J = 7.7 Hz, H-3), 7.15 (1H, t, J = 7.6 Hz, H-2), 5.91 (1H, t, J = 3.8 Hz, H-8), 2.81 (2H, t, J = 7.8 Hz, H₂-6), 2.74 (2H, t, J = 7.3, H₂-12), 2.61

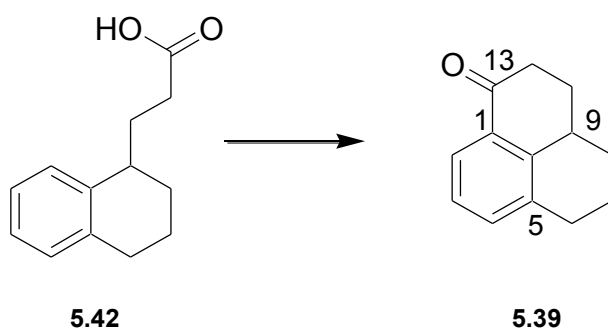
(2H, t, $J = 8.0$, H₂-11), 2.26 (2H, q, $J = 7.8$, H₂-7); ¹³C NMR (CDCl₃, 150 MHz) δ 179.6 (C, C-13), 136.7 (C, C-9), 134.6 (C, C-5), 134.2 (C, C-10), 127.7 (CH, C-4), 126.9 (CH, C-3), 126.4 (CH, C-1), 125.5 (CH, C-2), 122.3 (CH, C-8), 33.2 (CH₂, C-11), 28.2 (CH₂, C-12), 27.5 (CH₂, C-6), 23.0 (CH₂, C-7); HREIMS m/z 202.0983 (calcd for C₁₃H₁₄O₂ [M⁺], 202.0994).

6.4.5 Hydrogenation of **5.41** to Afford the Saturated Acid **5.42**



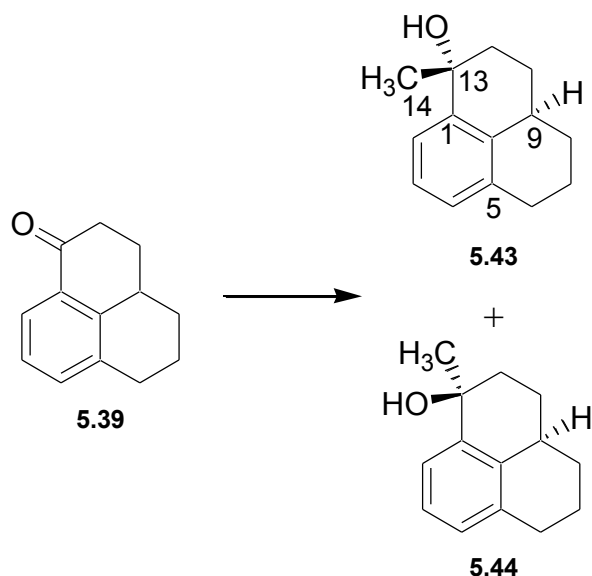
5.41 (400 mg, 2.12 mmol) was dissolved in methanol (4 mL) and hydrogenated over Pd-C (0.04 g) for 47 hours. The catalyst was filtered off and the mixture evaporated to give a colourless oil which was then purified on a silica column (3:1 toluene:ethyl acetate) to yield 3-(1,2,3,4-tetrahydro-naphthalen-1-yl)-propionic acid as a white powder (**5.42**, 287.4 mg, 1.51 mmol, 71 %).

3-(1,2,3,4-tetrahydro-naphthalen-1-yl)-propionic acid (5.42): white powder; IR (Disc) ν_{\max} 3020, 2935, 1709, 1421, 1218 cm⁻¹; ¹H NMR (CDCl₃, 600 MHz) 8.61 (1H, br s, 13-OH), 7.20 (1H, d, $J = 6.7$, H-1), 7.14 (1H, d, $J = 7.6$, H-4), 7.11 (1H, t, $J = 7.6$, H-3), 7.08 (1H, t, $J = 7.6$, H-2), 2.84 (2H, t, $J = 4.2$, H₂-6), 2.77 (1H, m, $J = 7.7$, H-9), 2.46 (2H, t, $J = 8.2$, H₂-12) 2.10 (2H, q, $J = 8.0$, H₂-11), 1.88 (2H, m, $J = 7.8$, H₂-7), 1.75 (2H, q, $J = 4.8$, H₂-8); ¹³C NMR (CDCl₃, 150 MHz) δ 180.1 (C, C-13), 139.9 (C, C-5), 137.1 (C, C-10), 129.1 (CH, C-4), 128.5 (CH, C-1), 125.7 (CH, C-3), 125.6 (CH, C-2), 36.8 (CH₂, C-8), 31.9 (CH, C-9), 31.3 (CH₂, C-12), 29.6 (CH₂, C-7), 27.3 (CH₂, C-6), 19.7 (CH₂, C-11); HREIMS m/z 204.1159 (calcd for C₁₃H₁₆O₂ [M⁺], 204.1150).

6.4.6 Preparation of Tricyclic Ketone **5.39**

A stirred mixture of **5.42** (105 mg, 0.526 mmol) and polyphosphoric acid was heated at 130 °C for 2 hours and then poured into ice water. The product was extracted with ethyl acetate (3 x 10 mL) and combined organic layers were washed with water (10 mL), saturated NaHCO₃ solution (10 mL), water (10 mL) and brine (10 mL); followed by drying with Na₂SO₄ and evaporation to produce a brown oil which was purified on a silica column (3:1 hexane:ethyl acetate) to yield 2,3,3a,4,5,6-hexahydro-phenalen-1-one as a brown solid (**5.39**, 78 mg, 0.426 mmol, 81 %).

2,3,3a,4,5,6-Hexahydro-phenalen-1-one (5.39): brown solid; IR (Disc) ν_{\max} 2932, 2867, 1678, 1586, 1282 cm⁻¹; ¹H NMR (CDCl₃, 600 MHz) δ 7.87 (1H, d, J = 7.6, H-2), 7.27 (1H, d, J = 7.6, H-4), 7.21 (1H, t, J = 7.6, H-3), 2.86 (2H, t, J = 6.7, H₂-6), 2.80 (1H, m, J = 4.8, H-9), 2.62 (2H, t, J = 5.2, H₂-12), 2.02 (2H, q, J = 4.5, H₂-11), 1.78 (2H, m, J = 4.3, H₂-7), 1.41 (2H, q, J = 11.2, H₂-8); ¹³C NMR (CDCl₃, 150 MHz) δ 198.9 (C, C-13), 143.3 (C, C-10), 136.5 (C, C-5), 134.3 (C, C-1), 131.9 (CH, C-4), 126.1 (CH, C-2), 125.0 (CH, C-3), 39.3 (CH₂, C-12), 36.5 (CH₂, C-8), 30.8 (CH₂, C-7), 30.3 (CH₂, C-6), 28.9 (CH, C-9), 22.6 (CH₂, C-11); HREIMS m/z 186.1050 (calcd for C₁₃H₁₄O [M⁺], 186.1045).

6.4.7 Methylation of Tricyclic Ketone **5.39**

A solution of **5.39** (100 mg, 0.54 mmol) in dry THF (5 mL) was cooled to -78 °C under N₂. A standard 1.6 M diethyl ether solution of MeLi (1.4 mL, 2.21 mmol) was added drop-wise to the mixture and the reaction was allowed to stir for 20 hours after warming to room temperature. The reaction was quenched by addition of an ice cold NaHCO₃ slurry (25 mL) and the product then extracted with ethyl acetate (3 x 20 mL). Combined organic layers were washed with water (2 x 20 mL) and brine; followed by drying with Na₂CO₃ and evaporation to produce 1-methyl-2,3,3a,4,5,6-hexahydro-1H-phenalen-1-ol as a yellow-brown oil (101.7 mg, 0.50 mmol, 93 %).

Purification on HPLC, using a solvent system of 7:1 hexane:ethyl acetate, yielded the diastereomeric pairs of 1-methyl-2,3,3a,4,5,6-hexahydro-1H-phenalen-1-ol: *anti*-1-methyl-2,3,3a,4,5,6-hexahydro-1H-phenalen-1-ol (**5.43**, 8 mg) as a yellow oil and *syn*-1-methyl-2,3,3a,4,5,6-hexahydro-1H-phenalen-1-ol (**5.44**, 30 mg) as a yellow solid.

Anti-1-methyl-2,3,3a,4,5,6-hexahydro-1H-phenalen-1-ol (5.43): yellow oil; IR (Disc) ν_{\max} 3020, 2933, 2861, 2401, 1216 cm⁻¹; ¹H NMR (CDCl₃, 600 MHz) δ 7.41 (1H, d, J = 7.8, H-2), 7.15 (1H, t, J = 7.6, H-3), 7.01 (1H, d, J = 7.6, H-4), 2.84 (2H, t, J = 6.4, H₂-6), 2.51 (1H, m, J

= 4.6, H-9), 2.06 (2H, t, J = 3.6, H₂-12), 2.04 (2H, m, J = 4.4, H₂-7), 1.92 (2H, q, J = 4.0, H₂-11), 1.60 (3H, s, H₃-14), 1.36 (2H, q, J = 11.2, H₂-8); ¹³C NMR (CDCl₃, 150 MHz) δ 141.5 (C, C-1), 137.0 (C, C-10), 136.5 (C, C-5), 128.1 (CH, C-4), 126.3 (CH, C-3), 123.8 (CH, C-2), 70.2 (C, C-13), 39.4 (CH₂, C-12), 37.4 (CH₂, C-8), 30.8 (CH₃, C-14), 30.6 (CH₂, C-7), 29.5 (CH₂, C-6), 27.1 (CH, C-9), 22.6 (CH₂, C-11); HREIMS *m/z* 202.1359 (calcd for C₁₄H₁₈O [M⁺], 202.1358).

Syn-1-methyl-2,3,3a,4,5,6,-hexahydro-1H-phenalen-1-ol (5.44): yellow solid; IR ν_{\max} 3020, 2933, 2861, 2401, 1216 cm⁻¹; ¹H NMR (CDCl₃, 600 MHz) δ 7.42 (1H, d, J = 7.8, H-2), 7.14 (1H, t, J = 7.6, H-3), 6.97 (1H, d, J = 7.6, H-4), 2.80 (2H, t, J = 6.4, H₂-6), 2.63 (2H, m, J = 4.4, H₂-7), 2.10 (2H, t, J = 3.6, H₂-12), 1.93 (1H, m, J = 4.6, H-9), 1.81 (2H, q, J = 4.0, H₂-11), 1.50 (3H, s, H₃-14), 1.32 (2H, q, J = 11.2, H₂-8); ¹³C NMR (CDCl₃, 150 MHz) δ 142.9 (C, C-1), 136.4 (C, C-10), 136.4 (C, C-5), 127.5 (CH, C-4), 126.1 (CH, C-3), 123.7 (CH, C-2), 72.4 (C, C-13), 40.5 (CH₂, C-12), 37.1 (CH₂, C-8), 32.3 (CH₃, C-14), 30.5 (CH, C-9), 29.7 (CH₂, C-6), 29.2 (CH₂, C-7), 22.6 (CH₂, C-11); HREIMS *m/z* 202.1359 (calcd for C₁₄H₁₈O [M⁺], 202.1358).

6.4.8 Attempted Synthesis of Tricyclic Isonitriles using the Method of Kitano *et al*

A mixture of diastereomers **5.43** and **5.44** (104 mg, 0.51 mmol) was taken up in 2 mL dry DCM under an inert argon atmosphere. TMSCN (128 μL, 1.02 mmol) was injected, solid AgClO₄ (106 mg, 0.51 mmol) was added and the mixture was stirred at r.t. for 2 h. The reaction was subsequently quenched with 2 mL sat. NaHCO₃ solution, stirred for 10 min and then filtered through a celite plug. The plug was washed with ethyl acetate (100 mL) and the combined organic layers concentrated under reduced pressure. The products were then passed through a short silica column.

6.4.9 Attempted Synthesis of 10-Isocyano-hispanalone **5.17**

Hispanalone (**5.16**, 154 mg, 0.49 mmol) was taken up in 2 mL dry DCM under an inert argon atmosphere. TMSCN (150 μ L, 1.20 mmol) was injected, solid AgClO_4 (102 mg, 0.49 mmol) was added and the mixture was stirred at r.t. for 2 h. The reaction was subsequently quenched with 2 mL sat. NaHCO_3 solution, stirred for 10 min and then filtered through a celite plug. The plug was washed with ethyl acetate (100 mL) and the combined organic layers concentrated under reduced pressure. The products were then passed through a short silica column.

REFERENCES

1. Snow, R. W.; Guerra, C. A.; Noor, A. M.; Myint, H. Y. *Nature*, **2005**, *434*, 214-217.
2. Sachs, J.; Malaney, P. *Nature*, **2002**, *415*, 680-685.
3. Singh, C.; Srivastav, N. C.; Puri, S. K. *Bioorg. & Med. Chem. Lett.*, **2002**, *12*, 2277-2279.
4. Rosenthal, P.J. *J. Exp. Biol.*, **2003**, *206*, 3735-3744.
5. Winstanely, P. A. *Parasitology Today*, **2000**, *16*, 146-153.
6. Schwarz, O.; Brun, R.; Bats, J. W.; Schmalz, H-G. *Tetrahedron Lett.*, **2002**, *43*, 1009-1013.
7. Ridley, R. G. *Nature*, **2002**, *415*, 686-693.
8. Bremen, J. *Am. J. Trop. Med. Hyg.*, **2001**, *64*, 1-11.
9. Meshnick, S; Dobson, M. In *Antimalarial Chemotherapy. Mechanisms of Action, Resistance, and New Directions in Drug Discovery*; Rosenthal, P., Ed.; Humana, Totowa, New Jersey, 2001, pp. 15-26.
10. Ridley, R. G.; Hudson, A. T. *Expert Opin. Ther. Pat.*, **1998**, *8*, 121-136.
11. O'Neill, P.; Bray, P.; Hawley, S.; Ward, S.; Park, B. *Pharmacol. Therapeut.*, **1998**, *77*, 29-58.
12. Tilley, L.; Loria, P.; Foley, M. In *Antimalarial Chemotherapy. Mechanisms of Action, Resistance, and New Directions in Drug Discovery*; Rosenthal, P., Ed.; Humana, Totowa, New Jersey, 2001, pp. 87-122.
13. Report No. WHO/CDS/RBM/2001.33 (World Health Organization, Geneva, 2001).
14. Wellems, T.; Plowe, C. *J. Infect. Dis.*, **2001**, *184*, 770-776.
15. Dorsey, G.; Fidock, D.; Wellems, T.; Rosenthal, P. In *Antimalarial Chemotherapy. Mechanisms of Action, Resistance, and New Directions in Drug Discovery*; Rosenthal, P., Ed.; Humana, Totowa, New Jersey, 2001, pp. 153-172.
16. Report No. WHO/MAL/98.1086 (World Health Organization, Geneva, 1998).
17. White, N. *Antimicrob. Agents. Chemoth.*, **1997**, *41*, 1413-1422.
18. Sherman, I. In *Malaria – Parasite Biology, Pathogenesis and Protection*; Sherman, I., Ed.; ASM, Washington D-C, 1998, pp. 177-184.
19. Wolfe, E. *Am. J. Trop. Med. Hyg.*, **2001**, *64*, 178-186.
20. Looareesuwan, S.; Chulay, J.; Canfield, C; Hutchinson, D. *Am. J. Trop. Med. Hyg.*, **1999**, *60*, 533-541.
21. Vaidya, A. In *Antimalarial Chemotherapy. Mechanisms of Action, Resistance, and New Directions in Drug Discovery*; Rosenthal, P., Ed.; Humana, Totowa, New Jersey, 2001, pp. 203-218.
22. Fichera, M.; Roos, D. *Nature*, **1997**, *390*, 407-409.
23. Clough, B.; Wilson, R. In *Antimalarial Chemotherapy. Mechanisms of Action, Resistance, and New Directions in Drug Discovery*; Rosenthal, P., Ed.; Humana, Totowa, New Jersey, 2001, pp. 265-286.
24. Watkins, W. M.; Mosobo, M. *T. Roy. Soc. Trop. Med. H.*, **1993**, *87*, 75-79.

25. Macreadie, I.; Ginsburg, H.; Sirawaraporn, W.; Tilley, L. *Parasitology Today*, **2000**, *16*, 438-444.
26. Francis, S.; Sullivan, D. G.; Goldberg, D. *Annu. Rev. Microbiol.*, **1997**, *51*, 97-123.
27. Coombs, G. *Trends Parasitol.*, **2001**, *17*, 532-537.
28. Shenai, B.; Sijwali, P.; Singh, A.; Rosenthal, P. *J. Biol. Chem.*, **2000**, *275*, 29000-29010.
29. Eggleston, K.; Duttin, K. Goldberg, D. *J. Biol. Chem.*, **1999**, *274*, 32411-32417.
30. Wright, A. D.; Wang, H.; Gurrath, M.; Köning, G. M.; Kocak, G.; Neumann, G.; Loria, P.; Foley, M.; Tilley, L. *J. Med. Chem.*, **2001**, *44*, 873-885.
31. Loria, P.; Miller, S.; Foley, M.; Tilley, L. *Biochem. J.*, **1999**, *339*, 363-370.
32. Ginsburg, H.; Famin, O.; Zhang, J.; Krugliak, M. *Biochem. Pharmacol.* **1998**, *56*, 1305-1313.
33. Slater, A. F. G.; Cerami, A. *Nature*, **1992**, *355*, 167-169.
34. Buller, R.; Peterson, M. L.; Almarsson, O.; Leiserowitz, L. *Crystal Growth & Design*, **2002**, *2*, 553-562.
35. Hyde, J. E. *Acta Tropica*, **2005**, *94*, 191-206.
36. Wilson, R. *J. Mol. Biol.*, **1996**, *261*, 155-172.
37. Jomaa, H. *Science*, **1999**, *285*, 1573-1576.
38. Waller, R. *Proc. Natl. Acad. Sci. USA*, **1998**, *95*, 12352-12357.
39. Surolia, N.; Surolia, A. *Nature Med.*, **2001**, *7*, 167-173.
40. Bannister, L. *Parasitology Today*, **2000**, *16*, 427-433.
41. Alzeer, J. *J. Med. Chem.*, **2000**, *43*, 560-568.
42. Dunn, C. R.; Banfield, M. J.; Barker, J. J.; Higham, C. W.; Moreton, K. M.; Turgut-Balik, D.; Brady, R. L.; Holbrook, J. J. *Nat. Struct. Biol.*, **1996**, *3*, 912-915.
43. Keough, D. T.; Ng, A. L.; Winzor, D. J.; Emmerson, B. T.; de Jersey, J. *Mol. Biochem. Parasitol.*, **1999**, *98*, 29-41.
44. Kirk, K. *J. Biol. Chem.*, **1994**, *269*, 3339-3347.
45. Gero, A. M.; Dunn, C. G.; Brown, D. M.; Pulenthiran, K.; Gorovits, E. L.; Bakos, T. Weis, A. L. *Curr. Pharm. Des.*, **2003**, *9*, 867-877.
46. Fidock, D. A.; Nomura, T.; Talley, A. K.; Cooper, R. A.; Dzekunov, S. M.; Ferdig, M. T.; Ursos, L. M.; Sidhu, A. B.; Naude, B.; Deitsch, K. W. *Mol. Cell.*, **2000**, *6*, 861-871.
47. Sirawaraporn, W.; *Exp. Parasitol.*, **1997**, *87*, 245-252.
48. Hyde, J. E. *TRENDS in Parasitol.*, **2005**, *21*, 494-498.
49. Ridley, R. G. *Nature*, **2002**, *415*, 686-693.
50. Stocks, P. A.; Raynes, K. J.; Ward, S. A. In *Antimalarial Chemotherapy: Mechanisms of Action, Resistance and New Directions in Drug Discovery*; Rosenthal, P., Ed.; Humana, Totowa, New Jersey, 2001, pp. 235-253.
51. Clough, B.; Wilson, R. J. M. In *Antimalarial Chemotherapy: Mechanisms of Action, Resistance and New Directions in Drug Discovery*; Rosenthal, P., Ed.; Humana, Totowa, New Jersey, 2001, pp. 265-286.

-
52. Meshnick, S. R. In *Antimalarial Chemotherapy: Mechanisms of Action, Resistance and New Directions in Drug Discovery*; Rosenthal, P., Ed.; Humana, Totowa, New Jersey, 2001, pp. 191-201.
53. Chibale, K., Biot, C. *Infectious Disorders – Drug Targets*, **2006**, *6*, 173-204.
54. Sullivan, D., Pisciotto, J. M. *Parasitology International*, **2008**, *57*, 89-96.
55. Egan, T. J., Marques, H. M. *Coord. Chem. Rev.*, **1999**, *1*, 493-517.
56. Duraisingh, Cowman, *Acta Tropica*, **2005**, *94*, 181-190.
57. Hyde, J. E. *TRENDS in Parasitol.*, **2005**, *21*, 494-498.
58. Slater, A. F. G., Swiggard, W. J., Orton, B. R., Flitter, W. D., Goldberg, D. E. Cerami, A., Henderson, G. B. *Proc. Natl. Acad. Sci. U.S.A*, **1990**, *1*, 325-329.
59. Bohle, D. S., Dinnebier, R. E., Madsen, S. K., Stephens, P. W. *J. Biol. Chem.*, **1997**, *272*, 713-716.
60. Egan, T. J., Chen, J., Y-J., de Villiers, K. A., Mabotha, T. E., Naidoo, K. J., Ncokazi, K. K., Langford, S. J., McNaughton, D., Pandiancherri, S., Wood, B. R. *FEBS Letters*, **2006**, *580*, 5105-5110.
61. Egan, T. J., Ncokazi, K. K. *Anal Biochem.*, **2004**, *338*, 306-319.
62. Sadasivan, N., Eberspaecher, H. I., Fuchsman, W. H., Caughey, W. S. *Biochemistry*, **1969**, *8*, 534.
63. Egan, T. J., Hempelmann, E., Mavuso, W. W. *J. Inorg. Biochem.*, **1999**, *73*, 101-107.
64. König, G. M.; Wright, A. D. *J. Org. Chem.*, **1996**, *61*, 3259-3267.
65. Iftimie, R.; Minary, P.; Tuckerman, M. E. *Proc. Natl. Acad. Sci.*, **2005**, *102*, 6654-6659.
66. Lee, H-S.; Tuckerman, M. E. *J. Phys. Chem. A*, **2006**, *110*, 5549-5560.
67. Allan, D.C.; Payne, M. C.; Teter, M. P. *J. Chem. Soc. Faraday Trans.* 1990, *86*, 1221-1226.
68. Hehre, W. J.; Yu, J.; Kluzinger, P.E.; Lou, L. *A Brief Guide to Molecular Mechanics and Quantum Chemical Calculations*; Wavefunction, Inc.: Irvine, 1998; pp 7- 28.
69. Lee, H-S.; Tuckerman, M. E. *J. Phys. Chem. A*, 2006, *110*, 5549-5560.
70. Møller, C.; Plesset, M.S. *Phys. Rev.* 1934, *46*, 618.
71. Becke, A. D. *Phys. Rev. A* 1988, *38*, 3098.
72. Lee, C. T.; Yang, W. T.; Parr, R. G. *Phys. Rev. B* 1998, *37*, 785.
73. Perdew, J. P.; Burke, K.; Ernzerhof, M. *Phys. Rev. Lett.* 1996, *77*, 3865.
74. Huey, R., Morris, G. M., Olson, A. J., Goodsell, D. S., A semiempirical free energy force field with charge-based desolvation. *J. Comput. Chem.*, 2007, *28*, 1145-1152.
75. Car, R.; Parrinello, M. *Phys. Rev. Lett.* 1985, *55*, 2471.
76. Araujo, J. C., de Mesquita Carneiro, J. W., de Araujo, M. T., Leited, F, H. A., Tarantod, A. G. *Bioorganic and Medicinal Chemistry*, **2008**, *16*, 5021-5029.
77. Dunning, T. H., Jr.; Hay, P. J. In *Modern Theoretical Chemistry v. 3*, Schaefer, H. F., III, Ed.; v. 3, New York, 1976.
78. Ramos, M. J., Pinto, M. M. M., Afonso, C. M. M., Portela, C. *Journal of Computer-Aided Molecular Design*, **2003**, *17*, 585-595.

-
79. Sousa, S. F., Fernandes, P. A., Ramos, M. J. *Proteins*, 2006, **65**, 1, 15-26.
80. Cornell, W. D., Cieplak, P., Bayly, C. I., Gould, I. R., Merz, K. M. Jr., Ferguson, D. M., Spellmeyer, D. C., Fox, T., Caldwell, J. W., Kollman, P. A. *J. Am. Chem. Soc.*, 1995, **117**, 5179-5197.
81. Morris, G. M., Goodsell, D. S., Halliday, R. S., Huey, R., Hart, W. E., Belew, R. S., Olson, A. *J. Comput. Chem.*, **1998**, **19**, 1639-1662.
82. Goble, J. L., Adendorff, M. R., de Beer, T. A. P., Stephens, L. L., Blatch, G. L. *Protein and Peptide Letters*, **2010**, **17**, 109-120.
83. Takahashi, S., Kuzuyama, T., Watanabe, H., Seto, H. *Proc. Natl. Acad. Sci.*, **1998**, **95**, 9879-9884.
84. Argyrou, A.; Blanchard, J.S. *Biochem.*, **2004**, **43**, 4375-4384.
85. Yajima, S.; Nonaka, T.; Kuzuyama, T.; Seto, H.; Ohsawa, K. *J. Biochem. (Tokyo)*, **2002**, **131**, 313-317.
86. Reuter, K.; Sanderbrand, S.; Jomaa, H.; Weisner, J.; Steinbrecher, I.; Beck, E.; Hintz, M.; Klebe, G.; Stubbs, M. *J. Biol. Chem.*, **2002**, **277**, 5378-5384.
87. Mac Sweeney, A.; Lange, R.; Fernandes, R.P.; Schulz, H.; Dale, G.E.; Douangamath, A.; Proteau, P.J.; Oefner, C. *J.Mol.Biol.*, **2005**, **345**, 115-127.
88. Kuzuyama, T.; Shimizu, T.; Takahashi, S.; Seto, H. *Tet. Lett.*, **1998**, **39**, 7913-7916.
89. Jomaa, J.; Wiesner, J.; Sanderbrand, S.; Altincicek, B.; Weidemeyer, C.; Hintz, M.; Turrbachova, I.; Eberl, M.; Zeidler, J.; Lichtenthaler, H.; Soldati, D.; Ewald Beck, E. *Science*, **1999**, **285**, 1573-1576.
90. Herforth, C.; Wiesner, J.; Heidler, P.; Sanderbrand, S.; Van Calenbergh, S.; Jomaa, H.; Link, A. *Bioorganic & Medicinal Chemistry*, **2004**, **12**, 755-762.
91. Silber, K.; Heidler, P.; Kurz, T.; Klebe, G. *J. Med. Chem.*, **2005**, **48**, 3547-3563.
92. Haemers, T.; Wiesner, J.; Van Poecke, S.; Goeman, J.; Henschker, D.; Beck, E.; Jomaa, H.; Van Calenbergh, S. *Bioorganic & Medicinal Chemistry Letters*, **2006**, **16**, 1888-1891.
93. Gießmann, D.; Heidler, P.; Haemers, T.; Van Calenbergh, S.; Reichenberg, A.; Jomaa, H.; Weidemeyer, C.; Sanderbrand, S.; Wiesner, J.; Link, A. *Chemistry and Biodiversity*, 2008, **5**, 643-656.
94. Singh, N., Cheve, G., Avery, M.A., McCurdy, C.R. *J. Chem. Inf. Model.*, **2006**, **46**, 1360-1370.
95. Kuzuyama, T.; Takahashi, S.; Takagi, M.; Seto, H. *J. Biol. Chem.*, **2000**, **275**, 19928-1992.
96. Morris, G. M., Huey, R. S., Lindstrom, W., Sanner, M. F., Belew, R. K., Goodsell, D. S., Olson, A. J. *Online publication in Wiley InterScience (www.interscience.wiley.com)*, **2009**.
97. Gasteiger, J., Marsili, M. *Tetrahedron*, **1980**, **36**, 3219-3228.
98. Manchester, J.I., Paulsen, M. D. and Ornstein, R. L. In Pullman, A. et al. (eds). *Modelling of Biomolecular Structures and Mechanisms*. Kluwer, Dordrecht, **1995**, pp. 181-188.
99. Curioni, A., Mordasini, T., Andreoni, W. *Journal of Computer-Aided Molecular Design*, **2004**, **18**, 773-784.
100. Dewar, M. J. S. *J. Am. Chem. Soc.*, **1985**, **107**, 3902-3909.

-
101. Doltsinis, N.L.; Marx, D. *Journal of Theoretical and Computational Chemistry*, **2002**, *1*, 19-49.
102. Marx, D.; Hutter, J. In *Modern Methods and Algorithms of Quantum Chemistry*; Grotendorst, J., Ed.; Forschungszentrum: Juelich, 2000, Vol. 3, pp. 329-477.
103. Yamauchi, Y.; Ozawa, S.; Nakai, H. *J. Phys. Chem. A* **2007**, *111*, 2062-2066.
104. Rodriguez-Forteza, A.; Iannuzzi, M.; Parrinello, M. *J. Phys Chem. B* **2006**, *110*, 3477-3484.
105. Teplyakov, A. V.; Kong, M. J.; Bent, S. F. *J. Am. Chem. Soc.* **1997**, *119*, 11100-11101.
106. Konecny, R.; Doren, D. J.; *J. Am. Chem. Soc.* **1997**, *119*, 11098-11099.
107. Wasserman, S. A.; Cozzarelli, N. R. *Science (Washington, D.C.)*, **1986**, *232*, 951.
108. van Wyk, A. W. W. PhD Thesis, Rhodes University, 2007.
109. Corbin, P.S., Zimmerman, S.C., Thiessen, P. A., Hawryluck, N.A., Murray, T.J. *J. Am Chem Soc.*, **2001**, *123*, 10475
110. Munro, O. Q., du Toit, K., Drewes, S. E., Crouch, N. R., Mulholland, D. A. *New J. Chem.*, **2006**, *30*, 197-207.
111. Keinan, S., Ratner, M. A., Marks, T. J. *Chem. Phys. Let.*, **2004**, *392*, 291-296.
112. Ochterski, J. W. *Gaussian Inc.*, **2000**.
113. Gaussian 03, Revision E.01, M. J. Frisch, G. W. Trucks, H. B. Schlegel, G. E. Scuseria, M. A. Robb, J. R. Cheeseman, J. A. Montgomery, Jr., T. Vreven, K. N. Kudin, J. C. Burant, J. M. Millam, S. S. Iyengar, J. Tomasi, V. Barone, B. Mennucci, M. Cossi, G. Scalmani, N. Rega, G. A. Petersson, H. Nakatsuji, M. Hada, M. Ehara, K. Toyota, R. Fukuda, J. Hasegawa, M. Ishida, T. Nakajima, Y. Honda, O. Kitao, H. Nakai, M. Klene, X. Li, J. E. Knox, H. P. Hratchian, J. B. Cross, V. Bakken, C. Adamo, J. Jaramillo, R. Gomperts, R. E. Stratmann, O. Yazyev, A. J. Austin, R. Cammi, C. Pomelli, J. W. Ochterski, P. Y. Ayala, K. Morokuma, G. A. Voth, P. Salvador, J. J. Dannenberg, V. G. Zakrzewski, S. Dapprich, A. D. Daniels, M. C. Strain, O. Farkas, D. K. Malick, A. D. Rabuck, K. Raghavachari, J. B. Foresman, J. V. Ortiz, Q. Cui, A. G. Baboul, S. Clifford, J. Cioslowski, B. B. Stefanov, G. Liu, A. Liashenko, P. Piskorz, I. Komaromi, R. L. Martin, D. J. Fox, T. Keith, M. A. Al-Laham, C. Y. Peng, A. Nanayakkara, M. Challacombe, P. M. W. Gill, B. Johnson, W. Chen, M. W. Wong, C. Gonzalez, and J. A. Pople, Gaussian, Inc., Wallingford CT, **2004**.
114. Kim, D., Klein, M. L. *J. Am. Chem. Soc.*, **1999**, *121*, 11251-11252.
115. Egan, T. J., Kaschula, C. H., Hunter, R., Basilico, N., Parapini, S., Taramelli, D., Pasini, E., Diego, M. *J. Med. Chem.*, **2002**, *45*, 3531-3539.
116. Kitano, Y., Chiba, K., Tada, M. *Tetrahedron Lett.*, **1998**, *39*, 1911.
117. Kitano, Y., Ito, T., Suzuki, T., Nogata, Y., Shinshima, K., Yoshimura, E., Chiba, K., Tada, M., Sakaguchi, I. *J. Chem. Soc., Perkin Trans. 1*, **2002**, *1*, 2251-2255.
118. March, J. *Advanced Organic Chemistry. Reactions, Mechanisms and Structure (4th Edition)*, John Wiley & Sons Ltd., New York, 1992, pp 367-368.
119. Barton, D., Ollis, W. D. *Comprehensive Organic Chemistry. The Synthesis and Reactions of Organic Compounds. Volume 2 Nitrogen Compounds, Carboxylic Acids, Phosphorous Compounds*, Sutherland, I. O., Ed.; Pergamon Press: Oxford, 1979, pp 568-569.

-
120. Barton, T. J., Tully, C. R. *J. Org. Chem.*, **1978**, *19*, 3649-3653.
 121. Van Wyk, A. W. W. PhD Thesis, Rhodes University, 2007.
 122. Socrates, G. *Infrared and Raman Characteristic Group Frequencies*, John Wiley & Sons Ltd., Chichester, 2001, pp 86.
 123. Wichmann, J., Adam, G., Röver, S., Henning, M., Scalone, M., Cesura, A. M., Dautzenberg, F. M., Jenck, F. *Eur. J. Med. Chem.*, **2000**, *35*, 839-851.
 124. Mathieson, D. W. *J. Chem. Soc.*, **1953**, 3251-3257.
 125. *Discovery Studio Visualizer, Release 2.0*, San Diego: Accelrys Software Inc., 2007.
 126. Portmann, S., Lüthi, H. P., *CHIMIA*, **2000**, *54*, 766.
 127. Pagola, S., Stephens, P. W., Bohle, D. S., Kosar, A. D., Madsen, S. K. *Nature*, **2000**, *404*, 307-310.
 128. Mast, N., White, M. A., Bjorkhem, I., Johnson, E. F., Stout, C. D., Pikuleva, I. A. *Proc.Natl.Acad.Sci.Usa*, **2008**, *105*, 9546-9551.
 129. Hay, P. J., Wadt, W. R. *J. Chem. Phys.*, **1985**, *82*, 299-311.
 130. Morris, G. M., Huey, R. S., Lindstrom, W., Sanner, M. F., Belew, R. K., Goodsell, D. S., Olson, A. J. AutoDock4 and AutoDockTools4: Automated docking with selective receptor flexibility. *Online publication in Wiley InterScience (www.interscience.wiley.com)*, **2009**.
 131. MGL Tools, Molecular Graphics Laboratory, The Scripps Research Institute, 2006-2009.
 132. Mulliken, R. S. *J. Chem. Phys.*, **1955**, *23*, 1833-1841.
 133. Humphrey, W., Dalke, A., Schulten, K. *J. Mol. Graphics.*, **1996**, *14*, 33-38.
 134. Cerius 2, Version 3.5, Molecular Simulations, San Diego, CA, 1997.
 135. Rappé, A. K., Casewit, C. J., Colwell, K. S., Goddard, W. A., Skiff, W. M. *J. Am. Chem. Soc.*, **1992**, *114*, 10046 – 10053.
 136. Goddard III, W. A., Mayo, S. L., Olafson, B. D. *J. Phys. Chem.*, **1990**, *94*, 8897-8909.
 137. Goedecker, S., Hartwigsen, C., Hutter, *J. Phys. Rev. B.*, **1998**, *58*, 3641-3662.
 138. CPMD, <http://www.cpmc.org/>, Copyright IBM Corp 1990-2008, Copyright MPI für Festkörperforschung, Stuttgart 1997-2001.
 139. Hünenberger, P. H. *Adv. Polymer. Sci.*, **2005**, *173*, 105-149.
 140. Steihaug, T. *SIAM. J. Num. Anal.* **1983**, *20*, 626-637.
 141. Perrin, D. D., Amarego, W. L. F., *Purification of Laboratory Chemicals (3rd Edition)*, Pergamon Press: Oxford, 1988.